



UNIVERSITÀ
DEGLI STUDI
FIRENZE

Ph.D. in ATOMIC AND MOLECULAR
PHOTONICS
CYCLE XXXII

COORDINATOR: PROF. FRANCESCO SAVERIO CATALIOTTI

Applying quantum Zeno effect to noise sensing
and geometrical phase detection

Academic Discipline (SSD): FIS/03

Doctoral Candidate:
Hoang-Van DO

Supervisor:
Prof. Francesco Saverio
CATALIOTTI

Coordinator:
Prof. Francesco Saverio
CATALIOTTI

Years 2016 – 2019

Thanks to

Thanks to Prof. Francesco Saverio CATALIOTTI for welcoming me into his group and for guiding me through the unfamiliar experiments with cold atoms.

Thanks to Prof. Taehyun KIM (Seoul National University) and Prof. Wonmin SON (Sogang University) for the short but exciting visit in their group.

Thanks to long-distance friends Alia ABBARA and Salam ABBARA, together with South Korean artists BTS for being my mental carers.

Special thanks to my parents Hoang-Phong DO and Ngoc-Bao PHAM for being supportive and for providing me with the best comforts.

Foreword

One of the primary keys to providing a good quantum resource is controlling the coherence of the quantum system. The protection of quantum coherence, or, complementarily, the measurement of environmental effects on a quantum system, is of great importance for the development of quantum technologies.

Dynamical decoupling methods have been introduced to protect a quantum dynamical evolution from decoherence and to infer specific features of the noise spectrum originating from the environment. By measuring the quantum system frequently enough, the system is placed into the so-called quantum Zeno regime, as described in Chapter 1 of this thesis.

The quantum Zeno effect (QZE) is demonstrated in a Bose-Einstein condensate (BEC) of rubidium-87 atoms on a chip. A BEC contains particles which all possess identical quantum states, presenting excellent tools for quantum simulations, while having the entire experiment controlled on a chip makes it conveniently compact, easy to use, stable, and robust. The experimental apparatus to produce and measure the BEC, as well as the application of projective measurements, is described in Chapter 2. Techniques for manipulating the quantum states of the atoms using microwave and radio-frequency pulses are also detailed.

The following three chapters form the core of the thesis, reporting new technologies developed through the application of projective measurements and methods of machine learning for practical quantum resource fabrication. Some of this work has been published in Refs. [1, 2].

To prove that the quantum Zeno effect not only provides a robust method for quantum control of populations but also maintains the coherence of the system, the geometric and dynamical phases acquired during evolution in the presence of measurement back-action are evaluated. Furthermore, when a state evolves through a closed loop on the Bloch sphere, it gains a geometric phase factor precisely corresponding to half the solid angle of the closed loop. Chapter 3 examines the geometric parameter in the presence of quan-

tum Zeno measurements. This chapter details work published in Ref. [1], coauthored with Manuel GESSNER, Francesco S. CATALIOTTI, and Augusto SMERZI.

Chapter 4 demonstrates how dynamical decoupling methods can be exploited in sensing technologies. Noise spectroscopy can be carried out by applying a sequence of projective measurements. This procedure induces the loss of atoms in the initial state, with a probability that presents maximal fluctuations when the measurement frequency is resonant with the noise frequency. The noise spectrum can be extracted with 80 – 90% fidelity. This chapter is based on Ref. [2], coauthored with Cosimo LOVECCHIO, Nicole FABBRI, Francesco S. CATALIOTTI, Stefano GHERARDINI, Matthias M. MÜLLER, Nicola DALLA POZZA, and Filippo CARUSO.

To pursue my interest in discovering other new quantum technologies, I visited the Department of Computer Science of Seoul National University. Here, using reinforced-learning methods, we searched for different experimental schemes to produce high-dimensional tripartite entangled states of photons and to assemble inter-level couplings to fabricate quantum logic gates in trapped ions. This work is described in Chapter 5 of the thesis.

Contents

1	Quantum Zeno effect	9
1.1	Quantum Zeno effect	9
1.2	Quantum Zeno dynamics	16
1.3	Conclusion	17
2	Experimental setup	19
2.1	Achieving Bose-Einstein condensation on a chip	19
2.1.1	^{87}Rb hyperfine structure and interaction with a magnetic field	19
2.1.2	Magneto-optical trap	21
2.1.3	Magnetic trap with Z-shaped wire	23
2.1.4	Evaporative cooling	25
2.2	Observing the atoms	26
2.2.1	Stern–Gerlach method	26
2.2.2	Absorption imaging	27
2.3	Exploiting the ^{87}Rb hyperfine structure	28
2.3.1	Transition between two hyperfine states	28
2.3.2	Transition between two magnetic sublevels of the same hyperfine manifold	29
2.4	Implementing projective measurements	29
2.5	Multi-level atomic interferometer	31
3	Geometric phases under quantum Zeno dynamics	37
3.1	Evaluation of the geometric phases	37
3.1.1	Introduction	37
3.1.2	Dynamical quantum Zeno effect and geometric phases	38
3.2	Measurements protocols	41
3.3	Results	42
4	Quantum Zeno effect assisted noise sensing	47
4.1	Generating noise with an arbitrary spectrum	48

4.1.1	Spectrum of a real noise	48
4.1.2	Sampling a real noise	49
4.2	Sensing scheme in the WQZ regime	52
4.2.1	Visualisation: Weak quantum Zeno regime as STFT	55
4.2.2	Spectrum reconstruction	56
4.3	Experimental implementation	57
5	Designing quantum computation experiments	69
5.1	Reinforcement learning	69
5.2	Producing high dimensional entangled resource	72
5.2.1	Entanglement estimation	73
5.2.2	Materials	74
5.2.3	Algorithm	75
5.2.4	Results	78
5.3	Designing ion quantum gates	83
5.3.1	Materials	83
5.4	Two qubits system made with QZE	85

Chapter 1

Quantum Zeno effect

Zeno (c. 490–430 BC) was a famous Greek philosopher who made many significant contributions to the world, among them the Zeno paradoxes, which people failed to explain at that time because of the limited understanding of infinity. The philosopher stated that motion was nothing but an illusion since at any instant, we can observe that any object would have a defined position and it would not move. However, motion is a concept defined between two instants of time. Furthermore, an object in motion at any instant has a non-zero momentum, a piece of information that was missing in Zeno’s statement.

Nonetheless, in quantum physics an interesting phenomenon occurs in which a quantum system can not change while it is being watched, just like the object described in Zeno’s story. The evolution of the system can be ‘frozen’ by measuring it frequently enough in its known initial state, or limited to a subspace by measuring its absence from the complement space. Due to the analogy between this quantum behaviour and Zeno’s arrow paradox, the name ‘quantum Zeno effect’ is given to the phenomenon. These two procedures are described in the two parts of this chapter dedicated to the quantum Zeno effect.

1.1 Quantum Zeno effect

Consider a quantum system prepared at time $t = 0$ in the state $|\Psi(0)\rangle$ which evolves under the Hamiltonian $H(t)$:

$$H(t) = H_0 + V(t), \tag{1.1}$$

with H_0 the bare Hamiltonian of the quantum system and $V(t)$ the interaction Hamiltonian that drives the evolution of the system. Performing an appropriate measurement projects the system to an initial state $|\Psi(0)\rangle$, which

undergoes free evolution into:

$$|\widetilde{\Psi(0)}\rangle = \exp\left(\frac{-iH_0t}{\hbar}\right) |\Psi(0)\rangle. \quad (1.2)$$

The problem is considered in the interaction picture, i.e., the reference frame rotates together with the free evolution of the system. In this frame, the projective measurement is fixed in time and the free evolution is included into the time-dependent state:

$$\exp\left(\frac{-iH_0t}{\hbar}\right) |\Psi\rangle \equiv |\Psi\rangle. \quad (1.3)$$

A measurement is performed after time δt . Immediately before the projection, the quantum state is

$$|\Psi(\delta t_-)\rangle = U(\delta t, 0) |\Psi(0)\rangle, \quad (1.4)$$

where the evolution operator is defined as $U(\delta t, 0)$.

The Schrödinger equation of motion is

$$i\hbar\partial_t|\Psi(t)\rangle = V(t)|\Psi(t)\rangle. \quad (1.5)$$

Equation 1.4 leads to the differential equation governing the evolution operator:

$$i\hbar\partial_t U(\delta t, 0) = V(t)U(\delta t, 0). \quad (1.6)$$

The solution of the following equation can be obtained by integrating the right-hand side:

$$U(\delta t, 0) = \mathbb{I} - \frac{i}{\hbar} \int_0^{\delta t} dt' V(t') U(t', 0). \quad (1.7)$$

For practical reasons, it is easier to work with dimensionless quantities, so the following change of variables is made:

$$z \equiv \frac{t}{\delta t} \quad (1.8)$$

$$\int_0^{\delta t} dt \rightarrow \int_0^1 dz. \quad (1.9)$$

We can see that Eq. 1.7 is self-consistent, i.e., when the solution is substituted back into the integral, it can be further expanded in an infinite series:

$$\begin{aligned}
U(z=1, 0) &= \mathbb{I} - \int_0^1 dz V(z) U(z, 0) \\
&= \mathbb{I} - \frac{i\delta t}{\hbar} \int_0^1 dz V(z) + \left(\frac{i\delta t}{\hbar}\right)^2 \int_0^1 dz_1 V(z_1) \int_0^1 dz_2 V(z_2) U(z_2, 0) \\
&= \sum_{n=0}^{\infty} \left(\frac{-i\delta t}{\hbar}\right)^n \int_0^1 dz_1 \cdots \int_0^1 dz_n V(z_1) \cdots V(z_n)
\end{aligned} \tag{1.10}$$

After the measurement, which is made by a projection to the initial state $Proj = |\Psi(0)\rangle\langle\Psi(0)|$, the state becomes

$$\begin{aligned}
|\Psi(\delta t_+)\rangle &= |\Psi(0)\rangle\langle\Psi(0)|\Psi(\delta t_-\rangle \\
&= |\Psi(0)\rangle\langle\Psi(0)|U(z=1, 0)|\Psi(0)\rangle.
\end{aligned} \tag{1.11}$$

The final outcome after a time $t = N\delta t$, with the measurement repeated each δt , is given by the state $|\Psi(t)\rangle$:

$$\begin{aligned}
|\Psi(t)\rangle &= \prod_{j=1}^N (|\Psi(0)\rangle\langle\Psi(0)|U(j, j-1)|\Psi(0)\rangle) \\
&= \prod_{j=1}^N |\Psi(0)\rangle (\langle\Psi(0)|U(j, j-1)|\Psi(0)\rangle) \\
&= |\Psi(0)\rangle \\
&\quad \prod_{j=1}^N \left(\langle\Psi(0)| \sum_{n=0}^{\infty} \left(\frac{-i\delta t}{\hbar}\right)^n \int_0^1 dz_1 \cdots \int_0^1 dz_n V(z_1) \cdots V(z_n) |\Psi(0)\rangle \right) \\
&= |\Psi(0)\rangle + |\Psi(0)\rangle \left(\langle\Psi(0)| \sum_{j=1}^N \left(\frac{-i\delta t}{\hbar}\right) \int_j^{j+1} dz V(z) |\Psi(0)\rangle \right) \\
&\quad + |\Psi(0)\rangle \left(\langle\Psi(0)| \sum_{j_1=1}^N \sum_{j_2=1}^N \left(\frac{-i\delta t}{\hbar}\right)^2 \int_{j_1}^{j_1+1} dz_1 \int_{j_2}^{j_2+1} dz_2 V(z_1) V(z_2) |\Psi(0)\rangle \right) \\
&\quad + \cdots,
\end{aligned} \tag{1.12}$$

Finally, the probability that the system remains in the initial state may be calculated:

$$\begin{aligned}
P &= |\langle \Psi(0) | \Psi(t) \rangle|^2 \\
&= \left(1 + \left(\frac{-i\delta t}{\hbar} \right) \left(\langle \Psi(0) | \sum_{j=1}^N \int_j^{j+1} dz V(z) | \Psi(0) \rangle \right) + \dots \right)^2 \\
&= \left(\sum_{k=0}^{\infty} \left(\frac{-i\delta t}{\hbar} \right)^k \overline{V}_k \right)^2,
\end{aligned} \tag{1.13}$$

where \overline{V}_k is the k -moment average of the interaction Hamiltonian, defined as

$$\overline{V}_k = \langle \Psi(0) | \sum_{j_1=1}^N \dots \sum_{j_k=1}^N \int_{j_1}^{j_1+1} dz_1 \dots \int_{j_k}^{j_k+1} dz_k V(z_1) \dots V(z_k) | \Psi(0) \rangle. \tag{1.14}$$

It is natural to assume that the quantum system and the interaction have finite energy and that the interaction Hamiltonian is bounded. The effect of the Hamiltonian on the system may be quantified by defining $Var(H)$, the variance of the Hamiltonian, as the average of its second moment by time,

$$Var(H) \equiv \langle \Psi(0) | H_{max}^2 | \Psi(0) \rangle \tag{1.15}$$

With this, the characteristic time for a significant change in evolution may be defined as

$$\tau_Z = \frac{\hbar}{\sqrt{Var(H)}}, \tag{1.16}$$

which, together with Eq.1.13, yields the probability for the system to remain frozen:

$$P = 1 + \mathcal{O} \left(N \left(\frac{\delta t}{\tau_Z} \right)^2 \right) \tag{1.17}$$

For a measurement time which is sufficiently short compared to the characteristic evolution time, $\delta t \ll \frac{\tau_Z}{\sqrt{N}}$, we can neglect the second-order term in $\frac{\delta t}{\tau_Z}$ and obtain a probability close to 1 for the system to remain in the initial state, i.e. the system is frozen and not able to evolve.

Case of a two-level system with constant coupling

Consider the specific case of a two-level system with a constant coupling V (under the rotating wave approximation), corresponding to an atomic system in the presence of a resonant electromagnetic field. Initially, the quantum

state is in one of the two levels on the z-axis of the Bloch sphere, which are eigenstates of the bare Hamiltonian of the system. The coupling is chosen as a rotation around the x-axis, which drives the system into the second level, orthogonal to the initial state. The Hamiltonian of the interaction, with a Rabi frequency of Ω , is written under the rotating wave approximation

$$V = \begin{pmatrix} 0 & \frac{\hbar\Omega}{2} \\ \frac{\hbar\Omega}{2} & 0 \end{pmatrix}. \quad (1.18)$$

It is straightforward to derive the evolution operator from the Schrödinger equation:

$$\begin{aligned} U(\delta t) &= \exp\left(-\frac{iV\delta t}{\hbar}\right) \\ &= \sum_{n=0}^{\infty} \frac{1}{n!} \left(-i \begin{pmatrix} 0 & \frac{\Omega\delta t}{2} \\ \frac{\Omega\delta t}{2} & 0 \end{pmatrix}\right)^n \\ &= \sum_{n=0}^{\infty} \frac{1}{(2n)!} (-1)^n \begin{pmatrix} \left(\frac{\Omega\delta t}{2}\right)^{2n} & 0 \\ 0 & \left(\frac{\Omega\delta t}{2}\right)^{2n} \end{pmatrix} \\ &\quad - i \sum_{n=0}^{\infty} \frac{1}{(2n+1)!} (-1)^n \begin{pmatrix} 0 & \left(\frac{\Omega\delta t}{2}\right)^{2n+1} \\ \left(\frac{\Omega\delta t}{2}\right)^{2n+1} & 0 \end{pmatrix} \\ &= \begin{pmatrix} \cos \frac{\Omega\delta t}{2} & -i \sin \frac{\Omega\delta t}{2} \\ -i \sin \frac{\Omega\delta t}{2} & \cos \frac{\Omega\delta t}{2} \end{pmatrix} \end{aligned} \quad (1.19)$$

Note that the atom oscillates between the two levels with a frequency Ω . The probability of being measured in the initial state hence varies sinusoidally in time due to the rotation induced by the driving field, as seen in Fig. 1.1.

$$P = |\langle \Psi(0) | \Psi(t) \rangle|^2 = \cos^2 \left(\frac{\Omega\delta t}{2} \right). \quad (1.20)$$

After a short interval of evolution δt , a measurement is made by projecting onto the initial state, therefore, after N projections, the evolved state is:

$$\begin{aligned} |\Psi(t = N\delta t)\rangle &= (|\Psi(0)\rangle \langle \Psi(0)| U(\delta t))^N |\Psi(0)\rangle \\ &= |\Psi(0)\rangle (\langle \Psi(0)| U(\delta t) |\Psi(0)\rangle)^N \\ &= |\Psi(0)\rangle \left(\cos \frac{\Omega\delta t}{2} \right)^N, \end{aligned} \quad (1.21)$$

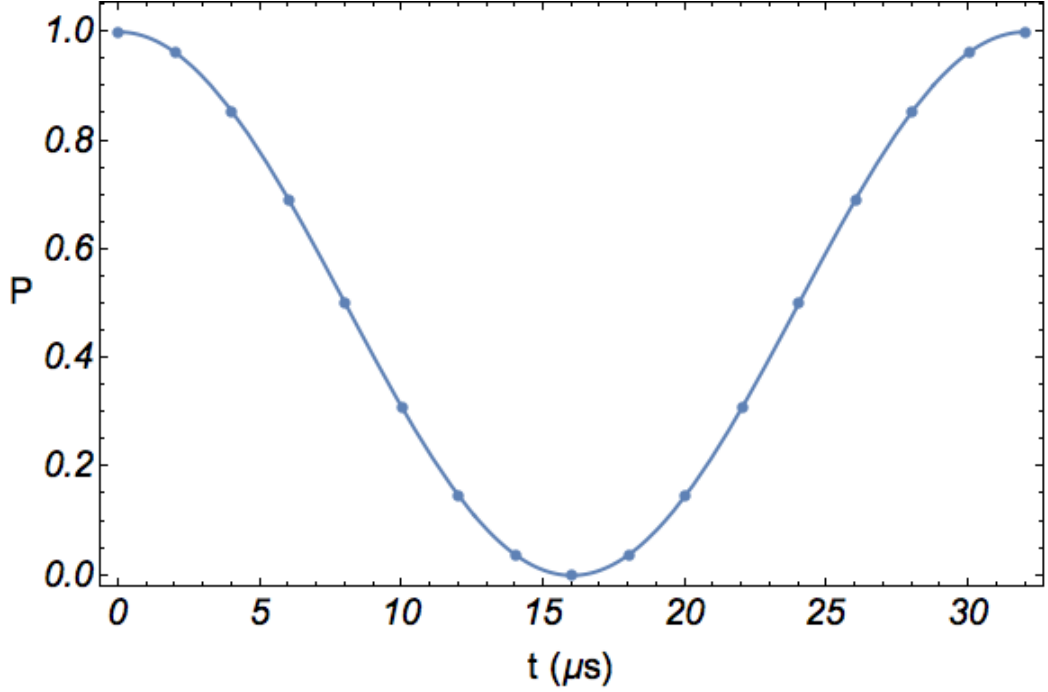


Figure 1.1: Probability for the final quantum state to be found in $|\Psi_0\rangle$ state for a Rabi frequency $\Omega = 2\pi \times 31.25$ kHz

and the final probability of remaining in the initial state is

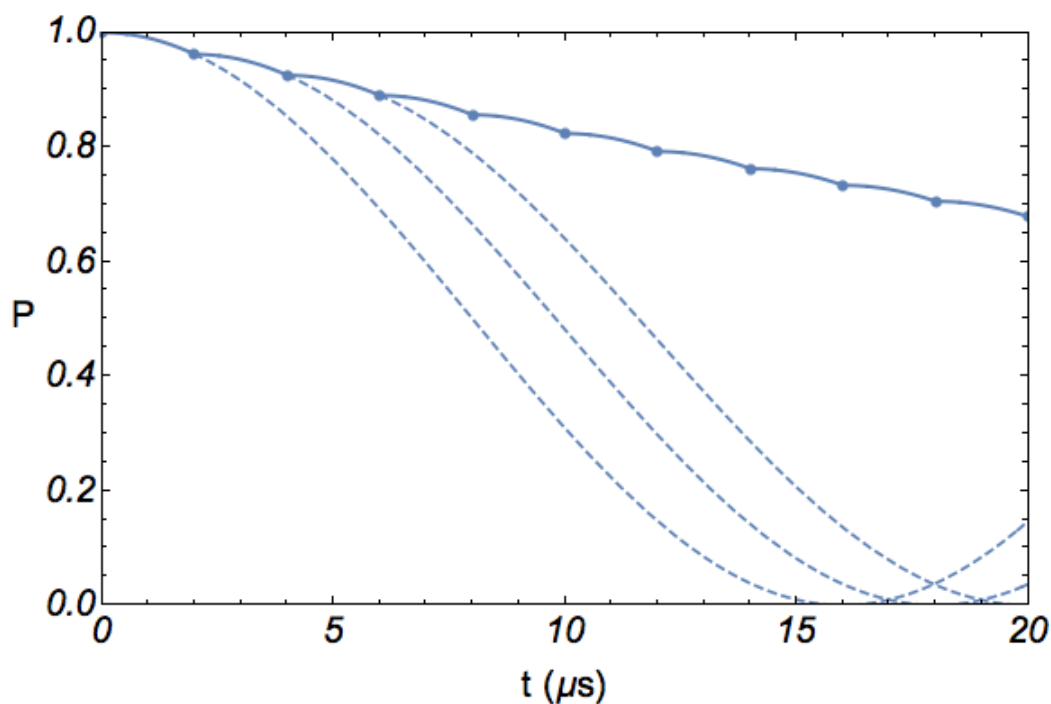
$$\begin{aligned}
 P &= |\langle \Psi(0) | \Psi(t) \rangle|^2 \\
 &= \left(\cos \frac{\Omega \delta t}{2} \right)^{2N} \\
 &= \left(\sum_{n=0}^{\infty} \frac{1}{(2n)!} (-1)^n \left(\frac{\Omega \delta t}{2} \right)^{2n} \right)^{2N} \\
 &= 1 - N \left(\frac{\Omega \delta t}{2} \right)^2 + \dots
 \end{aligned} \tag{1.22}$$

It is natural in this case to choose the Zeno characteristic time to be on the order of the period of the Rabi oscillation:

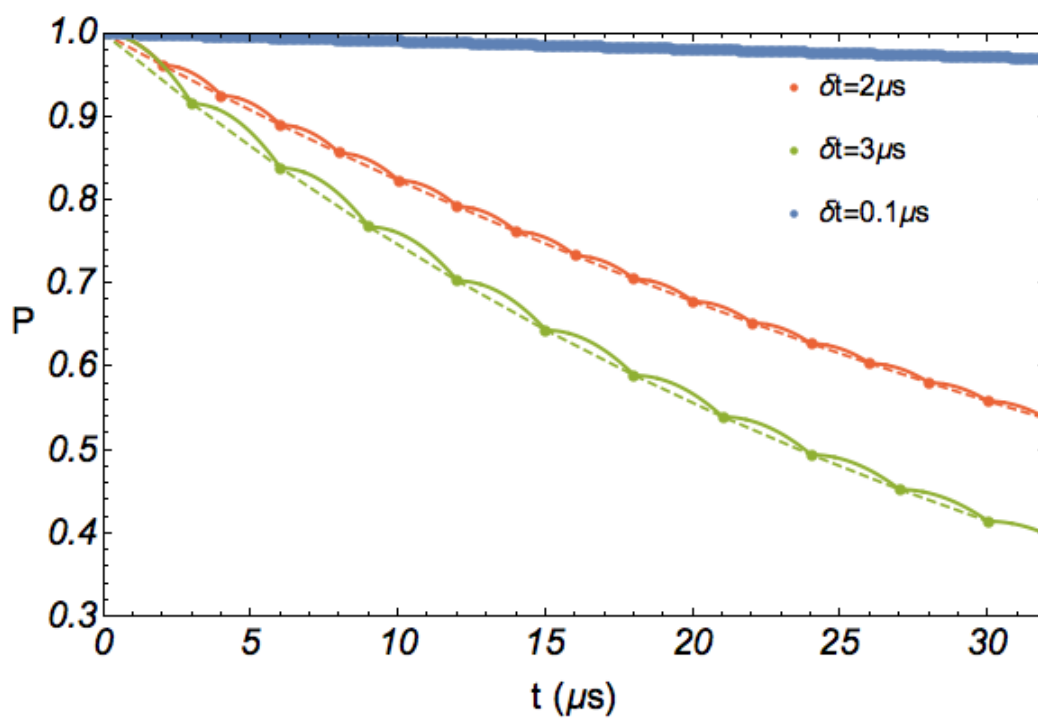
$$\tau_Z = \mathcal{O} \left(T = \frac{1}{2\pi\Omega} \right), \tag{1.23}$$

and hence Eq.1.17 is again obtained.

Figure 1.2a visualises the quantum Zeno effect for a Zeno repetition time $\delta t = 2 \mu\text{s}$, which is small compared to the Rabi oscillation period $T = 32 \mu\text{s}$.



(a) Probability for the final quantum state to be found in $|\Psi_0\rangle$ for a Rabi frequency $\Omega = 2\pi \times 31.25$ kHz, under a series of Zeno measurements with repetition time $\delta t = 2 \mu s$



(b) Probability for the final quantum state to be found in $|\Psi_0\rangle$ for a Rabi frequency $\Omega = 2\pi \times 31.25$ kHz, under a series of Zeno measurements with different repetition times

A short evolution close to the initial state takes place, a measurement is performed and resets the evolution: the probability to remain in the initial state decreases again as it was initially doing. The procedure continues and the progress is made with successive identical initial evolution.

Looking at Fig. 1.2b, it is clear that the probability of remaining in the initial state increases as the measurement interval is reduced. The limit $\delta t \rightarrow 0$, $P \rightarrow 1$, originally called the limit of ‘continuous observation’ by Misra and Sudarshan [5], describes the case where the system remains frozen under constant observation.

1.2 Quantum Zeno dynamics

In this section, we examine the case of a multi-dimensional quantum system. Given an n -dimensional quantum system, consider the effect of a projection onto a k -dimensional subspace \mathcal{H}_k containing the initial state, with $k < n$. The total space containing the quantum system is written as a sum of the projection subspace and its complement, $\mathcal{H}_n = \mathcal{H}_k \oplus \mathcal{H}_{n-k}$.

To start with, Eq.1.11 may be rewritten with the new projection operator:

$$Proj = Id_k \otimes 0_{n-k} \quad (1.24)$$

$$|\Psi(t)\rangle = [Proj \cdot U(\delta t)]^N |\Psi(0)\rangle. \quad (1.25)$$

Observe that the quantum projection does not prevent the quantum state from evolving within \mathcal{H}_k .

The next step is to evaluate the survival probability P , which is the probability of remaining in \mathcal{H}_k . Note that since the system is projected onto a subspace, not the initial state, the survival probability is no longer defined as the probability of remaining in the initial state $|\Psi(0)\rangle$. The system can still evolve to a different state within the projection subspace (that is, $|\Psi(t)\rangle \neq |\Psi(0)\rangle$, $|\Psi(t)\rangle \in \mathcal{H}_k$). Hence the survival probability is

$$\begin{aligned} P &= ||Proj \cdot |\Psi(t)\rangle||^2 \\ &= \text{Tr} \left[[Proj \cdot U(\delta t)]^N \rho_0 [Proj \cdot U(\delta t)]^{\dagger N} \right], \end{aligned} \quad (1.26)$$

where Tr denotes the trace, calculated by summing the average of the quantum operator in each basis state represented by the diagonal terms of the matrix, and $\rho_0 = |\Psi(0)\rangle\langle\Psi(0)|$ is the density matrix of the initial state. Note that as the projection subspace contains the initial state, the initial density matrix remains unaffected by the projection: $\rho_0 = Proj \cdot \rho_0 \cdot Proj$.

Equations 1.10 and 1.13 may now be rewritten as

$$\begin{aligned}
P &= \\
\text{Tr} &\left[\left[Proj \cdot \left(1 + \mathcal{O} \left(\left(\frac{\delta t}{\tau_Z} \right)^2 \right) \right) \right]^N \rho_0 \left[Proj \cdot \left(1 + \mathcal{O} \left(\left(\frac{\delta t}{\tau_Z} \right)^2 \right) \right) \right]^{\dagger N} \right] \\
&= \text{Tr} [Proj^N \cdot \rho_0] \left(1 + \mathcal{O} \left(\left(\frac{N\delta t}{\tau_Z} \right)^2 \right) \right) \\
&\approx_{\delta t \ll \tau_Z} \text{Tr} [Proj \cdot \rho_0] = 1.
\end{aligned} \tag{1.27}$$

The probability of remaining in the projection subspace tends to 1 as the projection repetition time tends to 0. This result is consistent with the previous result on the quantum Zeno effect.

1.3 Conclusion

The procedures described in this chapter rely on projective measurements, introduced with the aim of protecting a quantum dynamical evolution from decoherence [3, 4]. Quantum state protection has also been achieved experimentally by applying a sequence of quantum projective measurements, often called Zeno measurements, whose action freezes the dynamical evolution of the system under observation [5, 6, 7, 8, 9]. More generally, a quantum system can also be confined in an arbitrary subspace of a larger Hilbert space, according to the so-called quantum Zeno dynamics, as predicted in [10, 11, 12] and experimentally observed in [13, 14]. The existence of a relationship between dynamical decoupling methods and the application of a sequence of projective measurements for noise spectroscopy is also formally discussed in [15].

At the end of the next chapter, the quantum Zeno effect in a multi-dimensional system is demonstrated experimentally (see 2.4,2.5), making use of 5 magnetic sublevels in the hyperfine ground state $|F = 2\rangle$ and 3 magnetic sublevels in the hyperfine ground state $|F = 1\rangle$ of ^{87}Rb atoms.

Chapter 2

Experimental setup

All experiments in this thesis have been performed on a Bose condensed cloud of ^{87}Rb atoms released from a magnetic microtrap. The experiment consists of five basic steps:

1. Atoms are cooled in a magneto-optical trap.
2. The atoms are then loaded into a magnetic trap.
3. Evaporative cooling is used to achieve Bose-Einstein condensation.
4. The condensate is used as quantum resource for interferometry, sensor or other technologies.
5. The atoms are measured using absorption imaging techniques.

Each step is described in this chapter.

2.1 Achieving Bose-Einstein condensation on a chip

2.1.1 ^{87}Rb hyperfine structure and interaction with a magnetic field

This section describes the procedure of trapping and cooling ^{87}Rb atoms to a temperature near absolute zero. The ^{87}Rb atom possesses two absorption lines from a fine-structure doublet, D_1 ($S_{1/2}^2 \rightarrow P_{1/2}^2$) and D_2 ($S_{1/2}^2 \rightarrow P_{3/2}^2$). The D_2 transition has a natural linewidth $\Gamma \sim 2\pi \times 6$ MHz. The D_2 line also has a hyperfine structure induced by the coupling between the nuclear

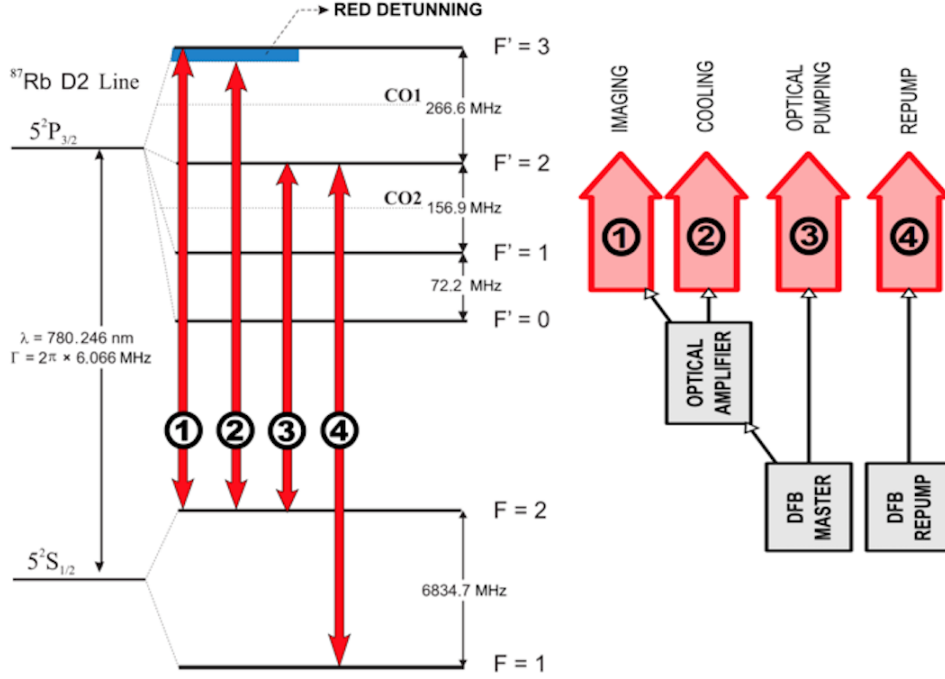


Figure 2.1: The hyperfine structure of the $5^2S_{1/2}$ and $5^2P_{3/2}$ states of the ^{87}Rb D2 line

angular momentum \vec{I} and the total electron angular momentum $\vec{J} = \vec{L} + \vec{S}$, with the Hamiltonian

$$H_{hfs} = A_{hfs} \vec{J} \cdot \vec{I}. \quad (2.1)$$

The eigenstates of this Hamiltonian, denoted $|F, m_F\rangle$, represent the total momentum $\vec{F} = \vec{I} + \vec{J}$. The ground state, with $L = 0$, contains two hyperfine manifolds: $F = 1$ with $2F + 1 = 3$ magnetic sublevels and $F = 2$ with five magnetic sublevels. The complete hyperfine structure of ^{87}Rb is shown in Fig.2.1.

Throughout the experiment, the interaction of the atoms with an electromagnetic field is exploited to trap, cool, and manipulate the atoms. Consider a magnetic field which the direction is defined as the z direction. The interaction of an atom and a magnetic field \vec{B} is described by the Hamiltonian H_B :

$$\begin{aligned}
H_B &= -\vec{\mu} \cdot \vec{B} \\
&= \mu_B \frac{(g_S \vec{S} + g_I \vec{I})}{\hbar} \cdot \vec{B} \\
&= \mu_B B \frac{(g_S S_z + g_I I_z)}{\hbar}
\end{aligned} \tag{2.2}$$

where $\mu_B = \frac{e\hbar}{2m_e} \approx 9.274 \cdot 10^{-24} \text{ J} \cdot \text{T}^{-1}$ is the Bohr magneton.

Under the assumption that the magnetic field used in the experiment is weak, i.e., $H_B \ll H_{hfs}$, the small energy shift of the levels $\Delta E_{F,m_F}(B)$ induced by the magnetic field is

$$\Delta E_{F,m_F}(B) = \mu_B g_F m_F B \tag{2.3}$$

where g_F is the Landé g-factor.

Furthermore, since the atomic magnetic moment follows adiabatically the direction set by the field, the atoms end up feeling a potential that is dependent on the magnitude of the magnetic field. Hence it is possible to trap atoms with a conveniently shaped inhomogeneous magnetic field.

2.1.2 Magneto-optical trap

Laser cooling and trapping are achieved under high vacuum conditions, therefore our experiment is performed inside a Vycor glass vacuum cell where an ion-pump maintains a pressure of 10^{-10} mbar.

A conventional magneto-optical trap (MOT) [16, 17, 18] for alkali atoms consists of the combination of a quadrupole magnetic field and six pairs of laser beams. The beams, coming from two lasers, each quasi-resonant with a D_2 transition starting from the two hyperfine ground states of the alkali, are overlapped in pairs coming from orthogonal directions and crossing in the zero of the magnetic quadrupole. In the case of ^{87}Rb , the six beams from one laser (cooling laser), red-detuned from the $F = 2 \rightarrow F'_0 = 3$ transition provides a cooling force and, in combination with the quadrupole field, a restoring force while the beams coming from the second laser (repumper laser), resonant with the $F = 1 \rightarrow F'_0 = 2$ transition repump the atoms in the $F = 2$ ground state.

Laser cooling

When the red-detuned cooling laser meets an atom, the following cases happened. The first case is when either the atom is not moving or is moving

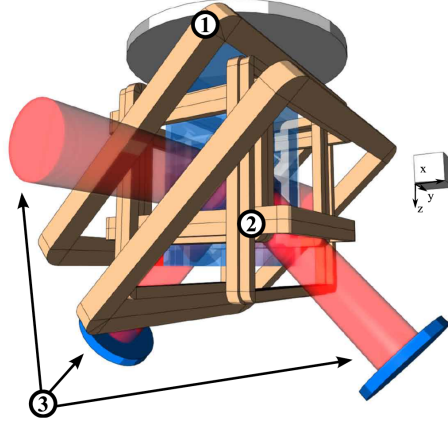


Figure 2.2: Design of the magneto-optical trap

toward the same direction of the arriving photon and sees an even more red-detuned frequency, there will not be any absorption of the photon which has a smaller frequency than the electronic transition $5S_{1/2}^2|F = 2\rangle \leftrightarrow 5P_{3/2}^2|F' = 3\rangle$. The second case is when the atom is moving toward the opposite direction of the arriving photon and sees a blue-detuned frequency, which is closer to the resonance frequency, absorption of the photon can now happen. Once the photon is absorbed, the atom received momentum in the reverse direction of its movements, and later emit the photon again in a random direction. This method allowed the atom to be slowed down by the transfer of momentum.

The atoms in the excited state $5^2P_{3/2}$ can sometimes into $5S_{1/2}^2|F = 1\rangle$ level. The repump laser puts the concerned atoms back in $5P_{3/2}^2|F' = 2\rangle$ and allows the atoms to fall back to the cooling loop $5S_{1/2}^2|F = 2\rangle \leftrightarrow 5P_{3/2}^2|F' = 3\rangle$.

In our experiment, since we are employing an Atom chip, i.e. a chip with microstructured conductors, we are forced to modify this configuration reflecting two pairs of beams off the surface of the chip creating a “mirror MOT” [19] as shown in Fig. 2.2

The mirror MOT is used to cool $\sim 70 \times 10^7$ atoms of ^{87}Rb to $\sim 100 \mu\text{K}$, making use of Doppler [20] and sub-Doppler [21] cooling techniques. The cooling laser is detuned by -3Γ from the $F = 2 \rightarrow F' = 3$ transition and has a power density of $10 \text{ mW}/\text{cm}^2$, and the repumper laser has a total power of 7 mW .

Quadrupole trapping

The quadrupole magnetic field is null in the center of the magnetic trapping point and increases linearly in magnitude with the distance of the atom to the center of the trap. As we have seen in equation (2.3), the presence of the magnetic field lifts the degeneracy of the magnetic sublevels depending on the m_F values and the radial distance of the atom to the trap. This energy shift is called the anomalous Zeeman effect and it makes the transition frequencies go closer to the arriving photons, increases the probability for an atom away from the center to absorb a photon and to be brought back to the center of the trap. We chose the light polarization in a way that it always interact with the right m_F sublevels.

The mirror MOT is completed by two 45° tilted anti-Helmholtz coils (Configuration 1 in Fig.2.2) that creates a field around the trap point (chosen to be the origin), given by

$$\vec{B}(x, y, z) = B_x x \vec{u}_x + B_y y \vec{u}_y + B_z z \vec{u}_z \quad (2.4)$$

The coils and beams are superimposed in such a way that the MOT center is 8 mm down from the chip surface.

Around the cell are also 6 pairs of coils in a Helmholtz configuration which generate opposite bias fields in each direction (see configuration 2 of Fig.2.2). Their purpose is twofold. On the one hand, they are used to compensate for the earth's magnetic field and any constant magnetic fields that could be coming from nearby equipment, especially the ion pump magnetic shield. On the other hand, they serve in connection with the chip wires to create the trapping potential.

2.1.3 Magnetic trap with Z-shaped wire

As mentioned above, the atomic magnetic moment adiabatically follows the magnetic fields hence magnetic trapping requires the creation of a local minimum of the field (Maxwell equations preventing the existence of a maximum) and low field seeking magnetic states (i.e. states who feel a potential that increases with the field modulus). However, it is impossible to be aligned with a null magnetic field (Majorana non-adiabatic transitions [22]), the presence of a zero in the magnetic field introduces losses in the trapping potential, therefore, a magnetic trap must have a non-zero minimum.

The chip was produced with the help of the Quantum Optics group at the University of Vienna. It is coated with a gold layer $2 \mu\text{m}$ thick, above which various wires are laid out. One of the wires, with a width of $125 \mu\text{m}$, resistance of 1.63Ω , and carrying a current I (the pink wire in Fig.2.3),

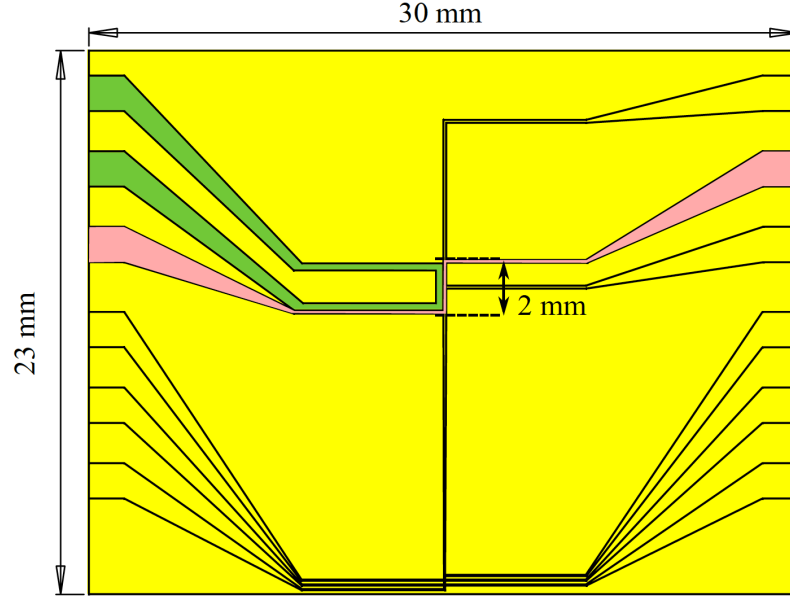
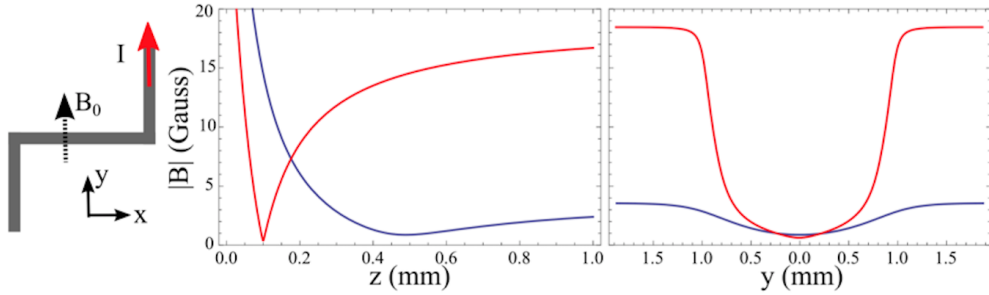


Figure 2.3: Layout of the wires on the chip surface

creates a magnetic field that traps the atoms. A plot of the magnetic field is shown below in Fig.2.4

Figure 2.4: Magnetic field calculated for a Z-shaped wire with a current $I = 1A$ at a distance $r = 0.5$ mm (red line) and $r = 0.1$ mm (blue line)

The trap frequencies produced by a current of ~ 1.5 A in the z-direction and ~ 900 mA in the y-direction, an external field of 15 Gauss were measured, yielding an axial trap frequency of $f_{axial} = 76$ Hz and a radial trap frequency of $f_{radial} = 975$ Hz.

A large Z-shaped Kapton wire was placed on the back side of the chip to create a larger trap to assist with transferring atoms from the MOT stage to the magnetic trap stage (see Fig.2.5).

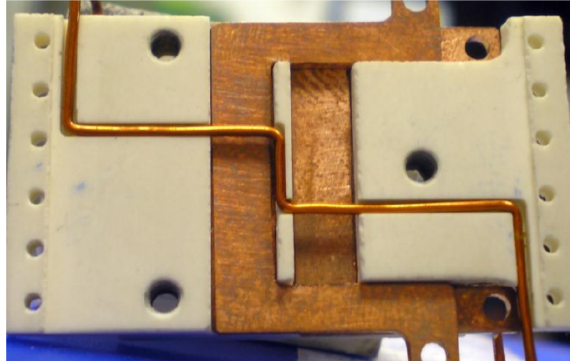


Figure 2.5: Photo of the back side of the chip

Figure 2.3 also shows, in green, a U-shaped wire that is used as a radio-frequency (RF) antenna to efficiently couple an external field to the atoms.

2.1.4 Evaporative cooling

The atoms are initially confined in a potential well with finite depth. When the energy of an atom is higher than the depth of the well, the atom escapes the confinement. The evaporative cooling is achieved by progressively lowering the depth of this potential well. In our experiment, the depth of the potential is regulated by inducing RF transitions between m_F sub-levels effectively turning the potential from trapping to anti-trapping. The potential depth is then lowered by decreasing the RF frequency. Through this procedure, even if the majority of the atoms were lost, we still get in the end 10^5 atoms out of 2×10^8 initially loaded from the magnetic trap. The main interest is that the atomic gas is cold down and reaches the quantum degenerescence and all the remained atoms are finally on a unique same quantum level.

After magnetic trapping, we apply a radio-frequency field, whose frequency decreases exponentially from 22 MHz to a final value of 0.7 MHz over 3 s, to a U-shaped conductor implanted on the back side of the chip (see Fig.2.5). We obtain 90×10^3 atoms condensed in $|F = 2; m_F = +2\rangle$ at a temperature $T = 480$ nK, distributed following a Thomas-Fermi profile in the anisotropic magnetic trap with a size $d_{axial} = 15.5 \mu\text{m}$ along the axial direction and $d_{radial} = 1.26 \mu\text{m}$ in the radial direction.

2.2 Observing the atoms

To record the number of atoms in each of the internal states, a Stern–Gerlach method [23] is used. Atoms are released from the magnetic trapping potential, after 1 ms of free expansion, a magnetic field gradient is applied along the quantisation axis (in addition to the homogeneous bias field) to separate the different m_F states. After a further 13 ms of expansion, a standard absorption imaging sequence [24] is executed. To ensure a strong absorption process, and thus a large signal-to-noise ratio, the probe beam is resonant with the transition $|F = 2\rangle \rightarrow |F = 3\rangle$. We take an image of the atoms in $|F = 2\rangle$, then repump atoms from $|F = 1\rangle$ to $|F = 2\rangle$ to take a second image $25 \mu\text{s}$ later.

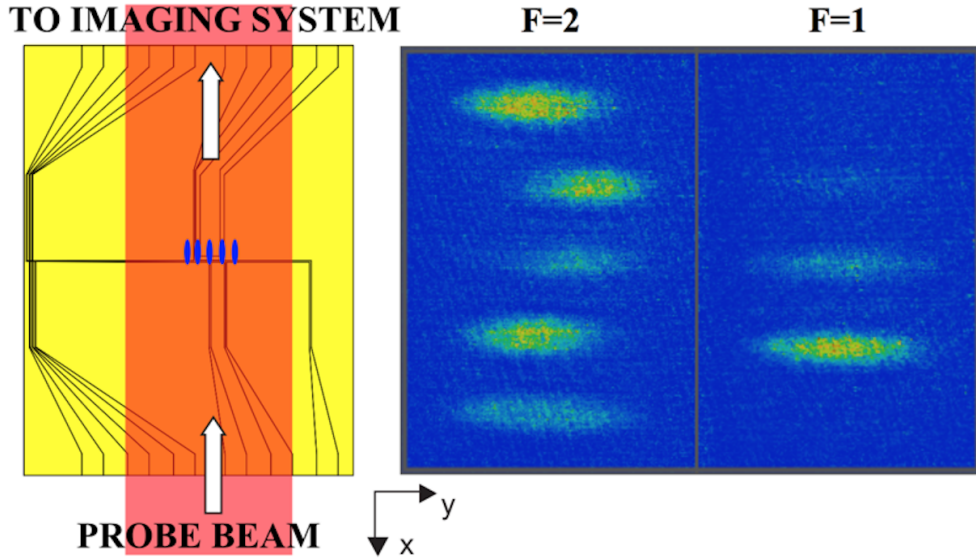


Figure 2.6: Image recorded with the absorption imaging method. The levels are spatially separated by the Stern–Gerlach procedure.

2.2.1 Stern–Gerlach method

To begin the measurement, with the trapping system turned off, the atoms are allowed to fall in the presence of an inhomogeneous magnetic field of 4 G/cm, generated by a pair of anti-Helmholtz coils placed in proximity to the cell, which is applied along the quantisation axis for 10 ms. Recall that the atoms evolve under the interaction Hamiltonian $H_B = -\vec{\mu} \cdot \vec{B}(\vec{r})$.

The different m_F states become spatially separated under the effect of a force:

$$\langle F, m_F | \vec{\nabla} \left(-\vec{\mu} \cdot \vec{B}(\vec{r}) \right) | F, m_F \rangle = -\mu_B g_F m_F \vec{\nabla} \vec{B}(\vec{r}). \quad (2.5)$$

The magnetic sublevels $|m_F = \pm 1, 2\rangle$ are deviated in opposite directions, while the magnetic sublevel $|m_F = 0\rangle$ does not sense any force and hence is not affected. (See Fig. 2.6.)

2.2.2 Absorption imaging

After further 13 ms of free-fall following application of the Stern-Gerlach method, we perform the following sequence using a sheet of probe beam on the Oyz plane and resonant with the transition $|F = 2\rangle \rightarrow |F = 3\rangle$.

1. The probe beam is applied for $25 \mu\text{s}$ and an image of the shadow cast by atoms in the $|F = 2\rangle$ manifold is taken with the CCD camera.
2. 1 ms after the first imaging, the imaging beam and repumping beam are switched on simultaneously, also for $25 \mu\text{s}$, to take an image of the atoms that were initially in the $|F = 1\rangle$ manifold.
3. After the probe beam has removed all the atoms from the trap, after 600 ms, the previous two steps are repeated to produce two images of the two frames with the corresponding light but without any atoms.
4. After 1200 ms, a final image of the dark background is taken, this time without any light.

In the first two steps, in the region of the beam where the atoms are present with a density $n(\vec{r})$, the resonant light excites the atoms and is absorbed. This results in a lower intensity $I_t(y, z)$ in this region relative to the initial intensity $I_0(y, z)$:

$$I_t(y, z) = I_0(y, z) \exp \left(-\sigma \int \vec{n}(r) dx \right) \quad (2.6)$$

with $\sigma = \frac{2\lambda^2}{2\pi}$ being the resonant absorption cross section.

By subtracting the images taken in step 3 from these pictures, the column atom density $\vec{n}(r)$ is extracted.

Since the atoms are identical and do not interact during the expansion, the relative atomic population of the sublevels is equivalent to the probability for each atom to be found in each of the sublevels.

2.3 Exploiting the ^{87}Rb hyperfine structure

2.3.1 Transition between two hyperfine states

A microwave field at 6.834 GHz is used to drive the transition between levels $|F = 1, m_F = 0\rangle$ and $|F = 2, m_F = 0\rangle$. Within the rotating wave approximation, the interaction Hamiltonian and its evolution operator of Eq.2.2 can be written, for two levels,

$$H = \begin{pmatrix} 0 & \frac{\hbar\Omega}{2} \\ \frac{\hbar\Omega}{2} & 0 \end{pmatrix} \quad (2.7)$$

$$U = \exp\left(-\frac{iHt}{\hbar}\right) = \begin{pmatrix} \cos \Omega/2 & -i \sin \Omega/2 \\ \cos \Omega/2 & -i \sin \Omega/2 \end{pmatrix} \quad (2.8)$$

The atoms oscillate between the two levels with a Rabi frequency $\Omega \propto \mu_B B$.

To generate this microwave field in the experiment, a 12 dBm signal at 6.834 GHz is produced by a synthesizer or a phase-locked coaxial resonator oscillator at a factor of 6834 with an external reference frequency of 10 MHz. This signal is amplified by a series of three mixers. In the final mixer, the field is mixed with an arbitrarily shaped signal from a wave generator with a resolution of 4 ns, which allows us to modulate and control the output field. The output is sent to a flat antenna placed under the atom chip. The oscillations and the Rabi frequency depend on the voltage set for the wave generator signal (see Fig.2.7).

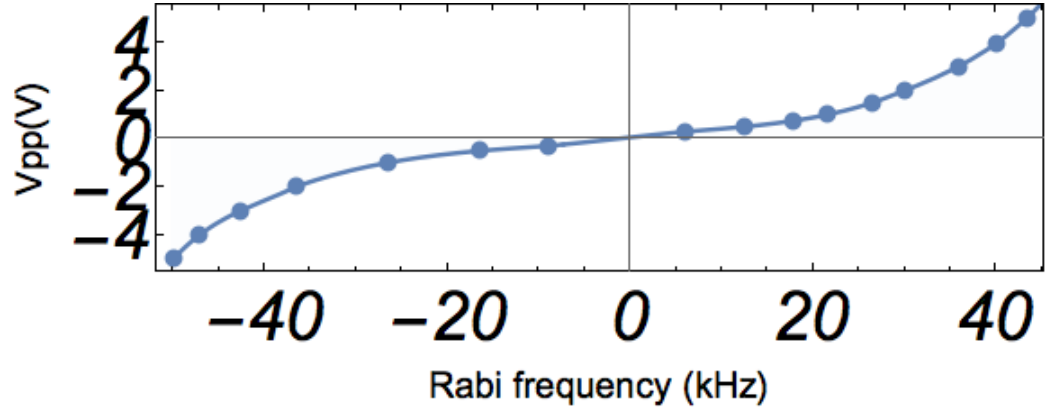


Figure 2.7: The microwave Rabi frequency as a function of the voltage of the control signal sent by the wave generator.

The transition created by the synthesizer or the resonator oscillator remains stable for fifty oscillations and is only limited by the atoms' survival

time. A future project could be to improve the design of the antenna to enhance the coupling.

2.3.2 Transition between two magnetic sublevels of the same hyperfine manifold

A resonant RF field with a frequency around 4.323 MHz is used to couple the sublevels $m_F = \{+2, +1, 0, -1, -2\}$ of $|F = 2\rangle$ and $m_F = \{+1, 0, -1\}$ of $|F = 1\rangle$ [25]. The signal is also mixed with the arbitrary wave generator to control the pulse. Figure 2.8 shows the Rabi frequency as a function of the voltage of the wave generator signal. The oscillation between sublevels is pictured later in the third chapter.

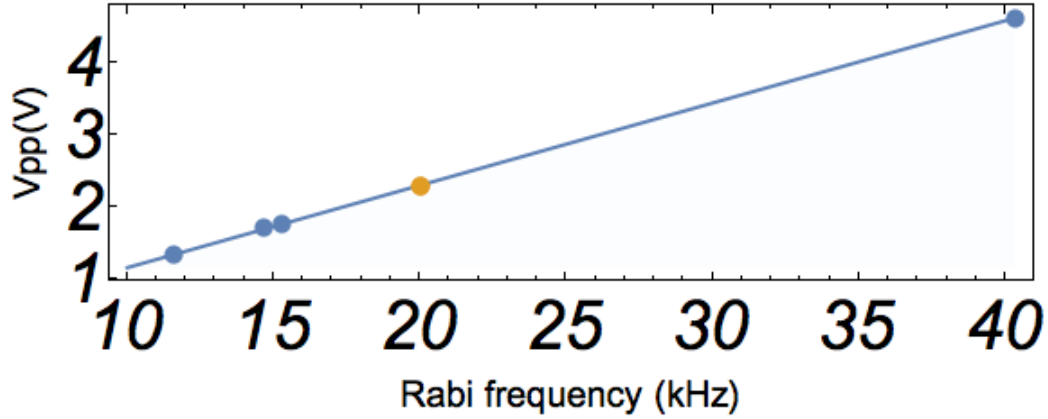


Figure 2.8: Rabi frequency induced by the RF field as a function of the voltage sent from the wave generator

2.4 Implementing projective measurements

The projective measurement $P = |F = 1\rangle\langle F = 1|$ is performed by illuminating the atoms with a light pulse of $1.5 \mu\text{s}$ duration, resonant with the $|F = 2\rangle \rightarrow |F = 3\rangle$ component of the rubidium $D2$ line. This pulse is fabricated by separating 1% from the same probe beam used for absorption imaging (beam 1 on Fig.2.1) using a beam splitter, then focussing it onto the atom cloud. Even though only a small fraction is used, the light is focused over a tiny area and so its power is increased.

Consider an atom in the measured in the hyperfine ground state $5S_{1/2}^2|F = 2\rangle \equiv |g\rangle$ under the projection pulse coupled to the excited state $5P_{3/2}^2|F' =$

$3\rangle \equiv |e\rangle$, has its quantum state written $|\Psi\rangle = c_g|g\rangle + c_e|e\rangle$. The Rabi frequency between induced by the projection pulse being Ω_0 and the decay rate of the excited being Γ , the evolution of the quantum state is written

$$i\partial_t c_g = \frac{\Omega_0}{2} c_e \quad (2.9)$$

$$i\partial_t c_e = \frac{\Omega_0}{2} c_g - i\Gamma c_e \quad (2.10)$$

$$(2.11)$$

The evolution of atoms in the excited state follows a damped harmonic oscillation equation:

$$\partial_t^2 c_e = -\frac{\Omega_0^2}{4} c_e - \partial_t \Gamma c_e \quad (2.12)$$

We put the system in the condition $\frac{\Omega_0}{2} < \Gamma$, i.e., the decay procedure is much faster than the coupling, and the oscillation is in the over damping stage where its amplitude decreased exponentially with Γ .

The atoms in $|F = 1\rangle$ are not affected. Now, the evolution matrix written between the two hyperfine ground state $|F = 1\rangle$ and $|F = 2\rangle$ is written

$$U(0, t) = \begin{pmatrix} e^{-2\Gamma} & e^{-\Gamma} \\ e^{-\Gamma} & 1 \end{pmatrix} \xrightarrow{\Gamma \rightarrow +\infty} \begin{pmatrix} 0 & 0 \\ 0 & 1 \end{pmatrix} \quad (2.13)$$

Observe that the stronger the damping is, the closer the evolution matrix is to an ideal projection.

The power of the projection pulse was not measured exactly, but the remaining number of atoms after an exposure time of t is shown in Fig. 2.9.

This light pulse causes the atoms that in the $|F = 2\rangle$ state to be lost, effectively implementing a projection onto the subspace orthogonal to $|\Psi_0\rangle$. Frequent repetition (every $\tau = 2\ \mu\text{s} \ll 1/\omega$) of such pulses effectively prevents atoms from entering this subspace, hence realising quantum Zeno dynamics.

Since the strongest Rabi pulse used creates a rotation with a period of $T = 25\ \mu\text{s}$, Zeno measurements with a $2\ \mu\text{s}$ rate and $1.5\ \mu\text{s}$ pulse duration are sufficient.

We first confirm the effectiveness of the Zeno pulses ($1.5\ \mu\text{s}$ of light resonant with the $F = 2 \rightarrow F' = 3$ transition). The atoms are divided into the three levels of $|F = 1\rangle$ with a $\pi/2$ RF pulse (note that the calibration of the RF pulses was not yet perfected in this preliminary test, causing the initial population ratios among $m_F = \{-1, 0, 1\}$ to deviate slightly from

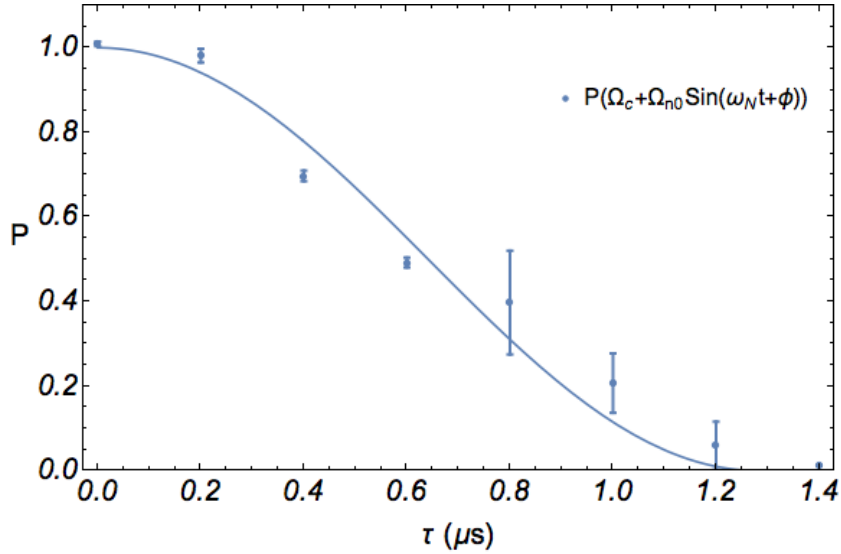


Figure 2.9: All the atoms in $|F = 2\rangle$ got blown away after $1.4 \mu\text{s}$

{25%, 50%, 25%}). The population distribution in the presence of the coupling between $|F = 1, m_F = 0\rangle$ and $|F = 2, m_F = 0\rangle$ is then measured. The population in each level is measured while driving the microwave transition for one full Rabi cycle. Afterwards, the same experiment is repeated with Zeno pulses applied every $2 \mu\text{s}$. Figure 2.10 shows that the Zeno pulses do indeed inhibit the atoms in $|F = 1, m_f = 0\rangle$ from making a transition to $|F = 2, m_F = 0\rangle$.

After this preliminary test, the projection light was focused to an even smaller area, with a diameter of $\sim \text{mm}$, in order to obtain a faster measurement. A pulse with a duration of less than $0.6 \mu\text{s}$ was able to remove all the atoms without scattering atoms in $|F = 1\rangle$ manifold. It is important to make sure that these measurements do not affect the projected subspace. However, a new limitation was encountered: the acousto-optic modulator that monitors the light pulse struggles to switch on and off with a time separation of less than $0.5 \mu\text{s}$. For this reason, the measurement requires at least $0.6 \mu\text{s}$ and so is not instantaneous.

2.5 Multi-level atomic interferometer

While the previous experimental proofs of the quantum Zeno effect provide control over the populations, they cannot provide direct access to the quantum phase, which is suppressed by the projections. However, the properties of the trajectory outlined by the projections can still yield a geometric

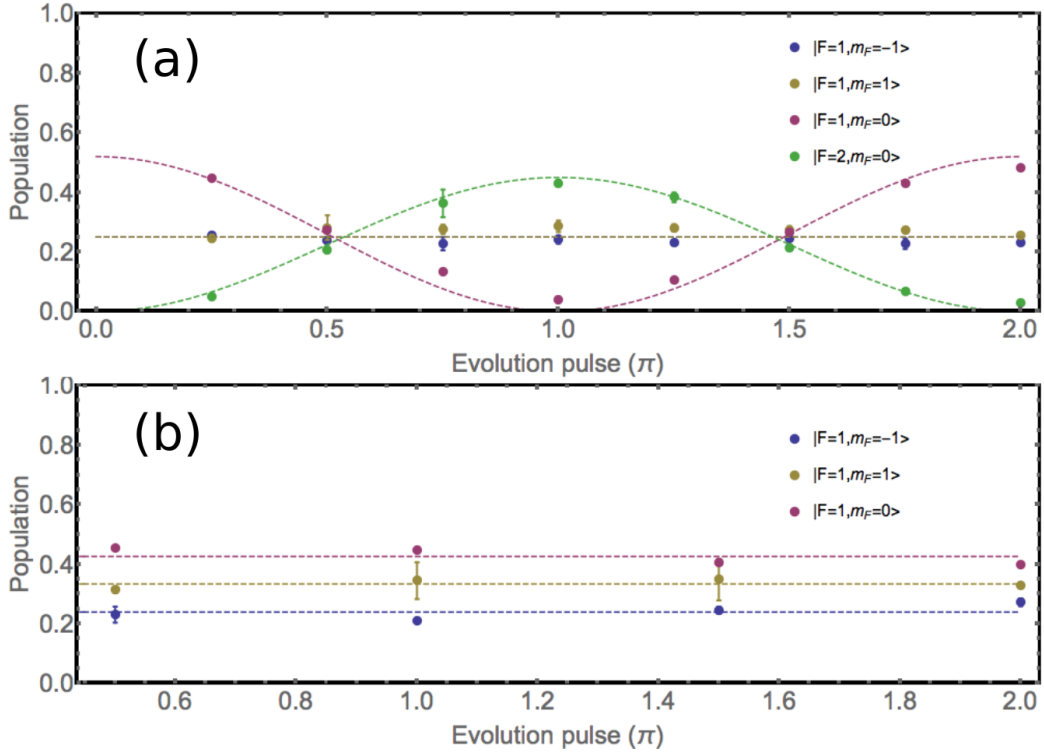


Figure 2.10: (a) Evolution of the atomic population in the presence of Zeno projective measurements. (b) Reference evolution without Zeno measurements.

phase factor that can be controlled and measured using a multi-level interferometer.

This section gives further details of the method for phase evaluation through the use of a three-level atomic interferometer.

Recall from Section that the presence of a homogeneous magnetic field of absolute value B lifts the degeneracy of the three magnetic sublevels $m_F = -1, 0, 1$ of the hyperfine ground state $|F = 1\rangle$ of ^{87}Rb atoms. The frequency difference $\Delta_{\pm} = \nu_{\pm 1} - \nu_0$ between the $m_F = \pm 1$ and the $m_F = 0$ sublevels depends on B as

$$\Delta_{\pm} = \mp g_I \mu_B B - \frac{\nu_{\downarrow\uparrow}}{2} \sqrt{1 \pm \frac{(g_J - g_I) \mu_B B}{\nu_{\downarrow\uparrow}} + \left(\frac{(g_J - g_I) \mu_B B}{\nu_{\downarrow\uparrow}} \right)^2},$$

where g_I and g_J are Landé factors, μ_B is the Bohr magneton and $\nu_{\downarrow\uparrow}$ is the frequency of the transition between the $|1, 0\rangle = |\downarrow\rangle$ and $|2, 0\rangle = |\uparrow\rangle$ states.

In the experiment, the initial state is the central state, $|F = 1, m_F = 0\rangle = |0, 1\rangle$. A near-resonant RF pulse with frequency $|\Delta_{\pm}| \approx 4.323$ MHz is applied

to drive the coherent transfer of excitations between magnetic sublevels of the same hyperfine state. Inspired by the Ramsey method of interferometry [42], the atoms are split into an interaction zone and a reference zone by applying two RF pulses, separated by a controllable time delay T (see Fig. 2.12). The second pulse maps the relative phases accumulated between different states during the delay into a population distribution at the output of the interferometer. At the end of the sequence, the populations of the three magnetic levels are measured.

We numerically calculate the interferometry figures for splitting and closing RF pulses with a duration corresponding to various rotations. Figure 2.11 shows the results of successive rotations of $\pi/4$, $\pi/2$, and $3\pi/4$. An equal splitting of the amplitude between states $|1, 0\rangle$ and $\frac{1}{\sqrt{2}}(|1, 1\rangle + e^{i\phi}|1, -1\rangle)$, i.e., a Ramsey-Bordé $\pi/2$ pulse, gives maximal visibility, as expected from the theory of a Ramsey interferometer.

From Fig. 2.11 we can see that the $\pi/2$ pulse, which puts half of the atoms in the reference zone and the other half in the interaction zone, is indeed the configuration that maximises the visibility of the interaction-induced phase change of the atoms. There is a more significant contrast between the $|m_F = 0\rangle$ state and its side levels $m_F = \pm 1$, as well as a wider gap between the case without additional phase and with additional phase using $\pi/2$ pulses comparing to using other pulses.

Accordingly, the starting and ending RF pulses are chosen to be $\pi/2$ for the interferometry scheme.

The first RF $\pi/2$ -pulse produces the superposition $|\Psi\rangle = (|\downarrow\rangle + |\Psi_r\rangle)/\sqrt{2}$, where $|\Psi_r\rangle = (|1; -1\rangle + |1; 1\rangle)/\sqrt{2}$. The reference state $|\Psi_r\rangle$ is unaffected by both the microwave coupling and the projective measurements and therefore provides a phase reference.

Figure 2.13 displays the relative populations of the three levels as a function of the evolution time T . In Fig. 2.13 a) this is shown for one instance of the reference evolution. We compute the system dynamics and fit the measured fringes using the magnetic field B as a free parameter. By measuring the magnetic field directly with the atomic interferometer, all systematic effects coming from day-to-day variations of the system environment may be eliminated. Indeed, the absolute value of the magnetic field is found to fluctuate in the range 6.180 – 6.184 G, demonstrating good stability within the experiment.

Figure 2.13 b) shows an example of the measurement-free evolution in the case of a full rotation in the yz plane. As expected, the fringes are shifted by half a period, indicating a phase difference of π relative to the reference evolution.

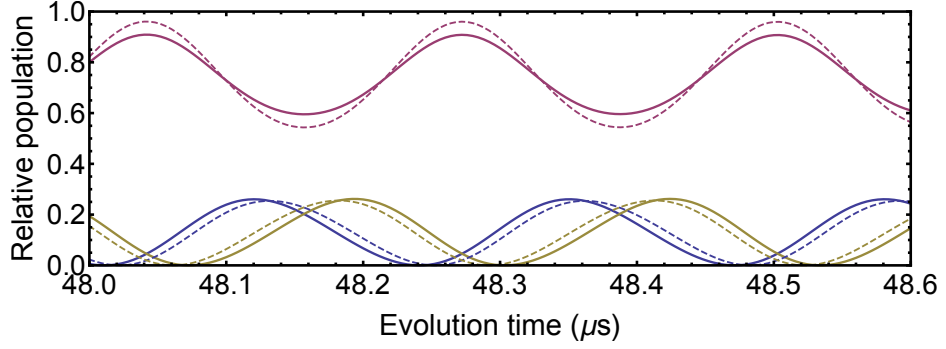
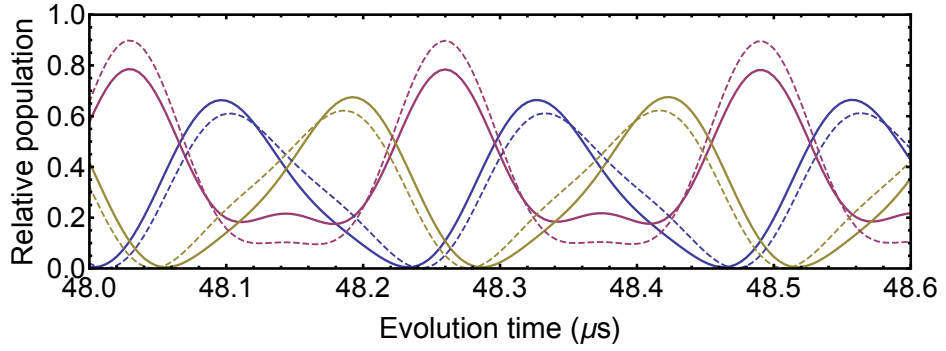
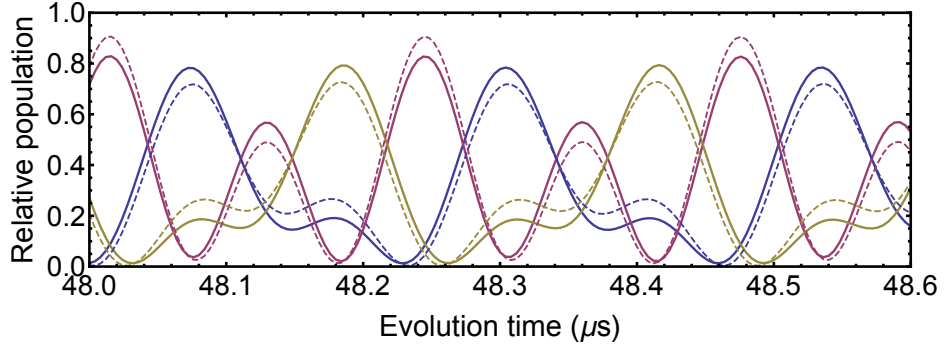
(a) $\pi/4$ split pulse(b) $\pi/2$ split pulse(c) $3\pi/4$ split pulse

Figure 2.11: Relative populations of the three magnetic sublevels of $|F = 1\rangle$ as a function of the evolution time T numerically simulated for $B = 6.18$ for different split pulses. The continuous line shows the system dynamics of a free evolution, while the dashed line shows the interferometer figures for a final state with an additional phase of $\pi/10$ added to $|F = 1, m_F = 0\rangle$.

Cases 1 and 2 are theoretically and experimentally identical, thus proving that there is indeed no disturbance of the local oscillator coming from

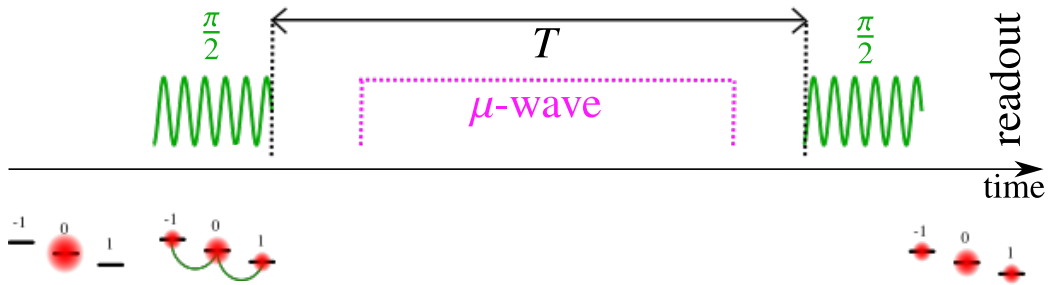


Figure 2.12: Scheme of the three-level atomic interferometer. A first $\pi/2$ RF pulse transfers half of the atomic population from the $|1,0\rangle$ state to the $|1,\pm 1\rangle$ states. These levels are not affected by either the microwave coupling or the projective measurements. Next, the system evolves for a time T according to one of the 4 cases discussed in the main text, which may involve driving with a microwave field. Finally, a second $\pi/2$ RF pulse closes the interferometer and the populations are read out.

the projective measurements. All the experimentally measured phases in the following are extracted by comparing to one of these references. In the theoretical description the phase reference is taken into account via the arbitrary energy offset ϵ .

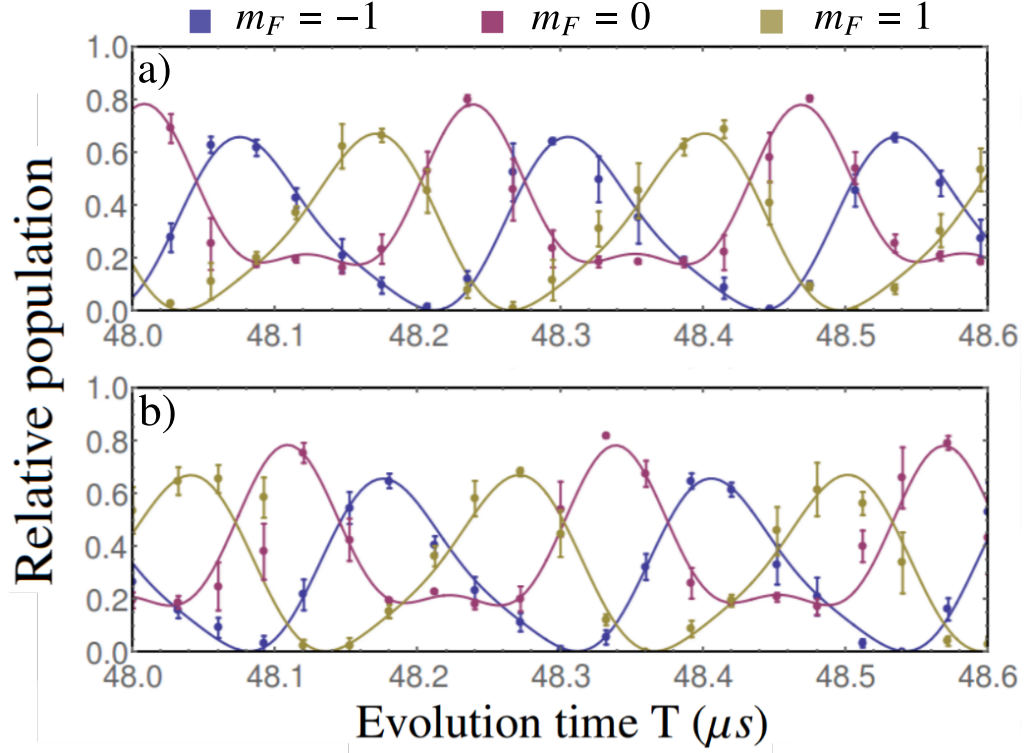


Figure 2.13: Relative populations of the three magnetic sublevels of $|F = 1\rangle$ as a function of the evolution time T . The experimental dots are the average of 5 repetitions with error bars representing the standard deviation. The continuous line is a fit to the data obtained by computing the system dynamics with B as a free parameter in a). In panel b) the magnetic field is fixed to the value found in a) while the free parameter is the phase ϕ of level $|1, 0\rangle = |\downarrow\rangle$.

Chapter 3

Geometric phases under quantum Zeno dynamics

A closed-trajectory evolution of a quantum state generally imprints a phase that contains both dynamical and geometrical contributions. While dynamical phases depend on the reference system, we uniquely define geometric phase factors by the properties of the outlined trajectory. Here, we generate and measure geometric phases in a Bose-Einstein condensate of ^{87}Rb using a combination of dynamical quantum Zeno effect and measurement-free evolution. We show that the dynamical quantum Zeno effect can inhibit the formation of a geometric phase without altering the dynamical phase, which can be used to extract the geometric Aharonov-Anandan phase from any closed-trajectory evolution without requiring knowledge or control of the Hamiltonian.

3.1 Evaluation of the geometric phases

3.1.1 Introduction

The dynamical quantum Zeno effect describes an evolution induced by measurement back-action, forcing the system to follow a sequence of projections [9, 5, 11, 12]. This technique provides a robust method for quantum control of populations, as has been demonstrated experimentally, e.g., for the static quantum Zeno effect with a trapped ion [6] and for dynamical evolution with atoms [13, 14]. Interestingly, an evolution driven by quantum back-action may also induce a nontrivial transformation of the quantum mechanical phase, despite the phase-insensitive nature of projective measurements. Indeed, the evolution along a closed trajectory gives rise to a

geometric phase factor, on top of a possible dynamical phase that depends on the realisation of the trajectory.

Geometric phases in quantum physics were first systematically studied for adiabatic evolution by Berry [26] and later generalised to arbitrary periodic evolution by Aharonov and Anandan [27]. They now play an integral part in all fields of quantum physics [28] and have been observed in several experiments, including nuclear magnetic resonance [29], molecular systems [30], graphene [31], solid-state qubits [32], and cold atoms in an optical lattice [33]. Controlling and manipulating geometric phase factors provides a robust alternative to engineering quantum states by purely dynamical evolution. As such, these techniques have potential applications in the field of quantum information, in particular quantum simulations [34] and quantum computations [35]. Geometric phases that arise from a sequence of projections were first discussed in the pioneering work of Pancharatnam [36] and were the subject of several subsequent studies [37, 38, 39, 40, 41].

In the work described in this chapter, we experimentally generate and measure geometric phase factors in a Bose-Einstein condensate using a combination of free evolution and the dynamical quantum Zeno effect. The theoretical framework for their interpretation is provided, showing that the purely geometric phase generated by a sequence of closely spaced projections on a closed trajectory can be understood by an equivalent two-step representation. In the first step, the system evolution along the trajectory is interrupted by frequent projections onto the initial state, which effectively freezes the dynamics. In the second step, the trajectory is retraced in the opposite direction, undisturbed by measurements. The geometric phase is entirely acquired as an Aharonov-Anandan phase in the second step. Since both steps require the same amount of time, their dynamical phases cancel, which leads to a robust method for isolating geometric phase factors from dynamical contributions, even without complete control of the Hamiltonian of the system.

3.1.2 Dynamical quantum Zeno effect and geometric phases

Consider a family of states $\{|\Psi_k\rangle\}$, each obtained from a small rotation $U(\delta t)$ of the preceding one, i.e., $|\Psi_k\rangle = U(\delta t)|\Psi_{k-1}\rangle$. If the first state $|\Psi_0\rangle$ and the last state $|\Psi_N\rangle = U(\delta t)^N|\Psi_0\rangle = e^{i\phi_0}|\Psi_0\rangle$ are identical except for the phase factor ϕ_0 then the states $\{|\Psi_k\rangle\}$ form a closed trajectory. Let us now consider the dynamics induced by a series of successive projections onto the states $\{|\Psi_k\rangle\}$, starting from the initial state $|\Psi_0\rangle$. The final state $|\Psi_f\rangle$ at the

end of the sequence of projections is given by

$$|\Psi_f\rangle = |\Psi_N\rangle\langle\Psi_N|\Psi_{N-1}\rangle\cdots\langle\Psi_2|\Psi_1\rangle\langle\Psi_1|\Psi_0\rangle. \quad (3.1)$$

Notice that since the evolution ends in a closed loop such that $|\Psi_N\rangle \equiv e^{i\phi_0}|\Psi_0\rangle$, the above expression can be written as

$$\begin{aligned} |\Psi_f\rangle &= e^{i\phi_0}|\Psi_0\rangle\langle\Psi_N|\Psi_{N-1}\rangle\cdots\langle\Psi_2|\Psi_1\rangle\langle\Psi_1|\Psi_0\rangle \\ &= e^{i\phi_0}|\Psi_0\rangle\langle\Psi_0|\left((U(\delta t))^N\right)^\dagger(U(\delta t))^{N-1}|\Psi_0\rangle\cdots\langle\Psi_0|U^\dagger(\delta t)|\Psi_0\rangle \\ &= e^{i\phi_0}|\Psi_0\rangle\left(\langle\Psi_0|U^\dagger(\delta t)|\Psi_0\rangle\right)^N \\ &\equiv e^{i\phi}|\Psi_0\rangle, \end{aligned} \quad (3.2)$$

where the total phase $\phi = \phi_0 + \phi_p$ contains both the phase ϕ_0 of the free evolution from $|\Psi_0\rangle$ to $|\Psi_N\rangle$ and an additional phase factor from the projections $e^{i\phi_p} = \prod_{k=1}^N\langle\Psi_k|\Psi_{k-1}\rangle = \left(\langle\Psi_0|U^\dagger(\delta t)|\Psi_0\rangle\right)^N$. This shows that the evolution (3.1) can be equivalently decomposed into (i) the *Zeno evolution*: N evolution steps backward in time of duration δt , each followed by a projection onto the initial state, and finally (ii) the *measurement-free evolution*: one long forward evolution of duration $T = N\delta t$.

Let us analyse the two steps of the process (3.1) separately, focusing first on the *measurement-free evolution* [step (ii)]. The eigenstates of the Pauli matrix σ_z are denoted by $|\downarrow\rangle$ and $|\uparrow\rangle$. The system evolution is generated by the Hamiltonian $H_{\mathbf{n}} = \omega\frac{\mathbf{n}\cdot\boldsymbol{\sigma}}{2} + \epsilon\frac{\mathbb{I}}{2}$, where $\mathbf{n} = (\sin\theta, 0, \cos\theta)$ is a unit vector and ϵ is an arbitrary energy offset whose significance will be specified below. After a period of $T = 2\pi/\omega$, the state $|\Psi_0\rangle = |\downarrow\rangle$ evolves with $U(t) = e^{-iH_{\mathbf{n}}t}$ to the state $|\Psi(T)\rangle = U(T)|\downarrow\rangle = e^{i\phi_0}|\downarrow\rangle$ and acquires a total phase of $\phi_0 = -\pi(1 + \frac{\epsilon}{\omega})$, which follows from $U(T) = e^{-i\pi(1 + \frac{\epsilon}{\omega})\mathbb{I}}$. Following Aharonov and Anandan [27], the dynamical phase associated with this evolution is determined:

$$\phi_d = -\int_0^T dt\langle\Psi(t)|H_{\mathbf{n}}|\Psi(t)\rangle = \pi\left(\cos\theta - \frac{\epsilon}{\omega}\right). \quad (3.3)$$

The total phase is now decomposed as $\phi_0 = \phi_d + \beta$, with the fully geometric Aharonov-Anandan phase

$$\beta = \Omega/2, \quad (3.4)$$

where $\Omega = 2\pi(1 - \cos\theta)$ is the solid angle of the trajectory subtended at the origin of the Bloch sphere. The phase β is therefore independent of the energy offset ϵ , while the dynamical and total phases are not.

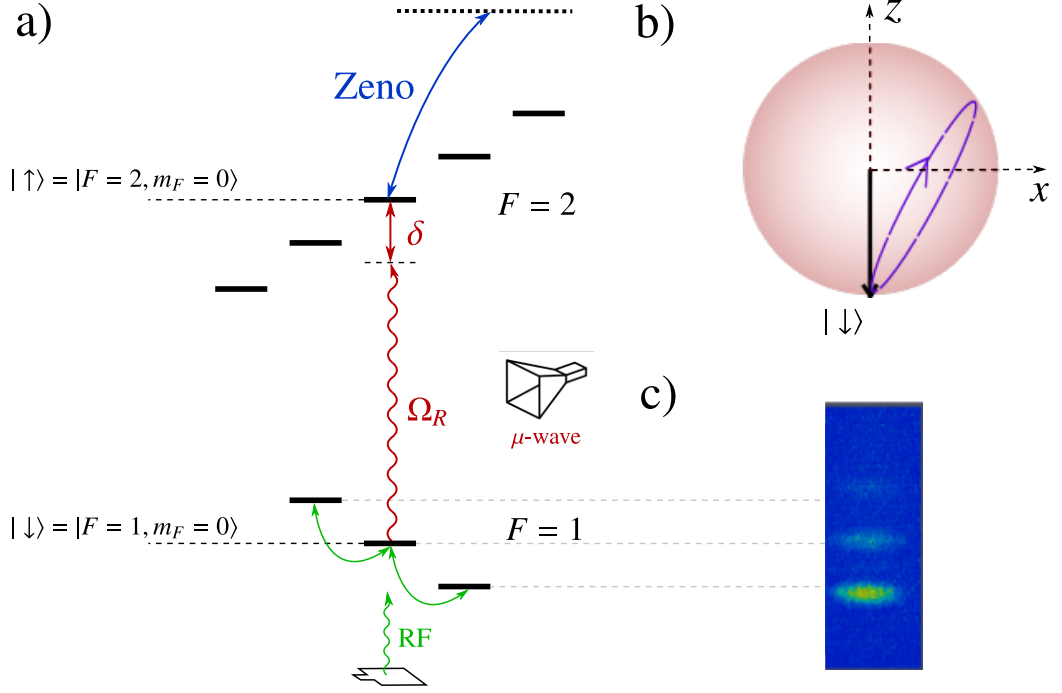


Figure 3.1: a) Schematic representation of the level structure of ^{87}Rb in the presence of a weak homogeneous magnetic field and the fields used to control the quantum state. A resonant radiofrequency (RF) field couples magnetic sublevels within the same hyperfine state (green lines), a quasi-resonant microwave field couples different hyperfine levels (red line), and an optical field implements the quantum Zeno dynamics by coupling to an excited state (blue line). b) Pictorial representation of the trajectory on the Bloch sphere achieved by evolution with the Hamiltonian $H_{\mathbf{n}}$. c) Absorption image of the $F = 1$ manifold after expansion in a magnetic field gradient.

Next, we analyse the phase ϕ_p that arises from the sequence of projections: the *Zeno evolution* [step (i)]. We obtain $e^{i\phi_p} = \langle \downarrow | U^\dagger(\delta t) | \downarrow \rangle^N = (\cos(\pi/N) - i \cos\theta \sin(\pi/N))^N e^{i\frac{\epsilon}{\omega}\pi}$, which in the limit of $N \rightarrow \infty$ tends to (see, e.g., [37])

$$\lim_{N \rightarrow \infty} \phi_p = -\pi \left(\cos\theta - \frac{\epsilon}{\omega} \right) = -\phi_d. \quad (3.5)$$

This corresponds to the negative dynamical phase of the measurement-free evolution (3.3). The negative sign is due to the appearance of adjoint evolution operators $U^\dagger(\delta t)$ that propagate backwards in time.

Combining the two results, it can be seen that the purely projective evolution (3.1) indeed imprints only the geometric phase $\phi = \beta$, as pointed out

in Refs. [37, 41]. The analysis here reveals that the origin of the geometric phase can be traced back to the Aharonov–Anandan phase that is generated in the final evolution [step (ii)]. Any dynamical phase that is created in this step is cancelled by the phase accumulated during the projections [step (i)], as both steps require the same time T .

3.2 Measurements protocols

Using a frequency-modulated radiofrequency (RF) pulse designed with an optimal control strategy (as described in), all the atoms are transferred into the $|\uparrow\rangle = |F = 2; m_F = 0\rangle$ state. Subsequently a microwave π -pulse at $\omega_0 = 6.834\,703$ GHz is used to transfer all the atoms into $|\downarrow\rangle = |F = 1; m_F = 0\rangle$. This is the initial state $|\Psi_0\rangle$ for the experiment.

By applying an RF $\pi/2$ -pulse which resonantly couples neighbouring m_F states, we produce a superposition $|\Psi\rangle = (|\downarrow\rangle + |\Psi_r\rangle)/\sqrt{2}$, where $|\Psi_r\rangle = (|1; -1\rangle + |1; 1\rangle)/\sqrt{2}$ is used as a local oscillator to provide a phase reference. (See 2.5 below for further explanation of three-level interferometry.)

The hyperfine transition $|1; 0\rangle \rightarrow |2; 0\rangle$ is then driven with a microwave field of frequency ω_L (see experimental details in 2.3.1). Defining the resonant Rabi frequency produced by the microwave as Ω_R and the detuning as $\delta = \omega_0 - \omega_L$, the atomic evolution is described in the rotating wave approximation by the Hamiltonian $H_{\mathbf{n}}$, where $\omega = \sqrt{\Omega_R^2 + \delta^2}$, $\cos\theta = \delta/\omega$, and $\sin\theta = \Omega_R/\omega$. Projective measurements $P = |\Psi_0\rangle\langle\Psi_0|$ are produced by illuminating the atoms with a light pulse of $1.5\,\mu\text{s}$ duration, resonant with the $|F = 2\rangle \rightarrow |F = 3\rangle$ component of the rubidium $D2$ line. Note that atoms in the excited state $|F = 3\rangle$ immediately decay outside the condensate and are therefore lost. Quantum Zeno dynamics is realised by applying projective measurement pulses every $\tau = 2\,\mu\text{s}$, which means that $\tau \ll 1/\omega$.

At the end of the evolution period T the phase is measured by overlapping with the local oscillator, employing a second RF $\pi/2$ -pulse. In essence, this closes a 3-level Ramsey-like atomic interferometer. In the absence of driving, the interferometer output exhibits fringes in the atomic population of the three levels with a periodicity dictated by the homogeneous magnetic field.

With the atoms always initialised in the state $|\downarrow\rangle$, the experimental protocol consists of recording the interferometric fringes for the following four cases:

1. *Reference evolution 1*: Evolution of the system in the absence of coupling between $|\downarrow\rangle$ and $|\uparrow\rangle$, introducing a phase shift ϕ_1 .
2. *Reference evolution 2*: Evolution of the system in the absence of cou-

pling between $|\downarrow\rangle$ and $|\uparrow\rangle$ while performing projective measurements onto $|\downarrow\rangle$, introducing a phase shift ϕ_2 .

3. *Measurement-free evolution*: Evolution of the system in the presence of coupling $|\downarrow\rangle$ and $|\uparrow\rangle$ with $H_{\mathbf{n}}$, introducing a phase shift ϕ_3 .
4. *Zeno evolution*: Evolution of the system in the presence of coupling $|\downarrow\rangle$ and $|\uparrow\rangle$ with $H_{\mathbf{n}}$ while performing projective measurements onto $|\downarrow\rangle$, introducing a phase shift ϕ_4 .

All experiments are repeated 5 times for statistical significance.

3.3 Results

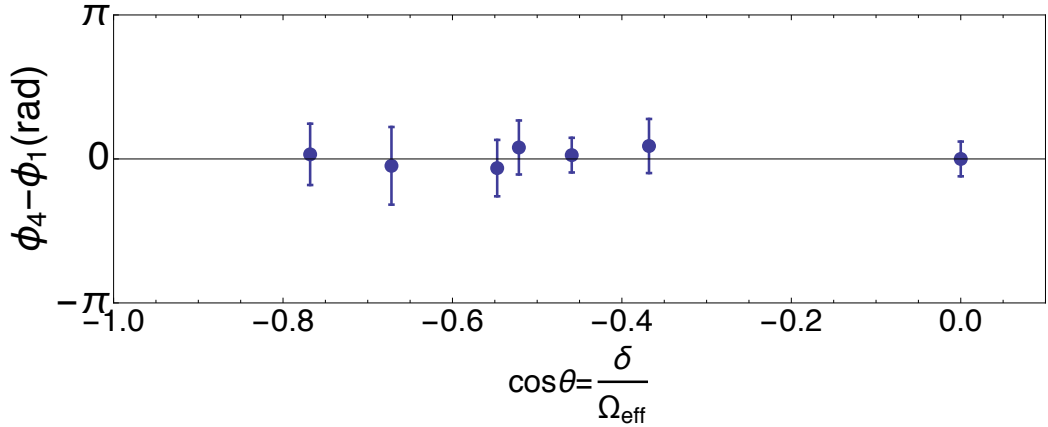


Figure 3.2: Difference between phase shifts recorded for the *Zeno evolution* (case 4) and the purely dynamical phase that is obtained by the reference evolution without driving and measurements (case 1).

Figure 3.2 shows the experimentally recorded phases for the Zeno evolution for different detunings δ , which rotate \mathbf{n} . This corresponds to the forward evolution, driven by $H_{\mathbf{n}}$, that generates the phase $-\phi_p = \phi_d$. The projective part in Eq. (3.1) describes an evolution along the same trajectory but in the opposite direction, which corresponds to the dynamics generated by $H_{-\mathbf{n}}$. The measured phases $-\phi_p$ are compared to the phases obtained by waiting for the same time T without any external driving or measurements (reference evolution 1), which imprints the dynamical phase $-(\epsilon - \delta)T/2 = \pi(\delta - \epsilon)/\omega = \phi_d$ as defined in Eq. (3.3), with ϵ given by the RF frequency. The coinciding phase shifts for these two evolutions confirm

that the projections freeze the system in the initial state, which inhibits the accumulation of geometric phase factors, while a dynamical phase is still acquired due to the passing of time.

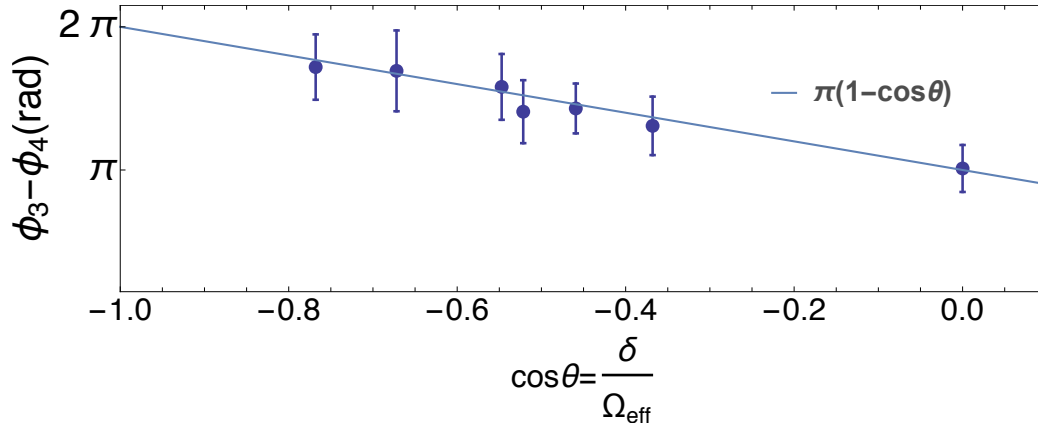


Figure 3.3: Difference between phase shifts of the measurement-free evolution in the presence of coupling without Zeno measurements (case 3) and the phase shift coming from the Zeno evolution in the presence of coupling with Zeno measurements (case 4). The phase difference $\phi_0 - \phi_d = \beta$ is the purely geometric Aharonov-Anandan phase, as predicted in Eq. (3.4), which depends only on the trajectory and is independent of the dynamical process.

Figure 3.3 shows the phase shifts generated by the closed trajectory of projections, described in Eq. (3.1). This corresponds to the combination of steps (i) and (ii). We show the result of the subtraction of the phase shift acquired during the Zeno evolution (ϕ_4) from the phase shift acquired during the measurement-free evolution (ϕ_3) for various detunings δ of the microwave coupling. The result, as predicted in Eq. (3.4), is the purely geometric Aharonov-Anandan phase $\beta = \pi(1 - \cos\theta)$, shown as a continuous line in the figure.

To demonstrate that the measured phase β is indeed geometric and only depends on the properties of the trajectory via Eq. (3.4), a series of additional measurements with different trajectories are performed. Figure 3.4 shows three sets of experiments:

- a) Retracing a circular trajectory twice.
- b) Evolving along a larger intersection of two spherical caps by abruptly changing \mathbf{n} during the evolution.
- c) Evolving along a smaller intersection of two spherical caps by abruptly changing \mathbf{n} during the evolution.

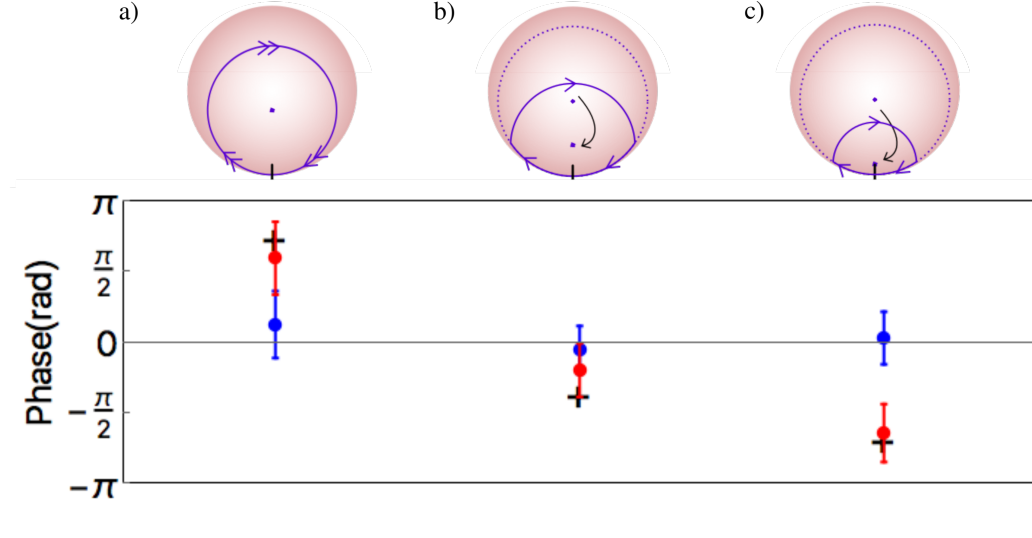


Figure 3.4: Phase shifts for the different trajectories represented on the Bloch sphere at the top of the figure. The three cases a), b), and c) are explained in the text. The blue dots show the differences $(\phi_4 - \phi_1)$ between phase shifts recorded for the *Zeno evolution* (case 4) and the purely dynamical phase that is obtained by the *reference evolution 1* without driving and measurements (case 1). The difference is expected to be compatible with zero (dotted line). The red dots show the differences $(\phi_3 - \phi_4)$ between phase shifts for the *measurement-free evolution* in the presence of coupling without Zeno measurements (case 3) and the phase shift coming from the *Zeno evolution* in the presence of coupling with Zeno measurements (case 4). This difference realizes the purely projective evolution (3.1). The expected geometrical phase factor is predicted by Eq. (3.4) which is shown as black dots.

For case a), we expect to find twice the solid angle of the single trajectory. The detuning was chosen as $\delta = 16$ kHz, with a resonant Rabi frequency $\Omega_R = 40.4$ kHz leading to an angle of $\theta = 1.19$ rad.

The solid angles of intersecting spherical caps (b and c) can be determined from elementary geometric considerations by changing the rotation axis abruptly $\mathbf{n}_i \rightarrow \mathbf{n}_j$. For simplicity, symmetrical evolutions are chosen:

$$|\Psi(t)\rangle = \exp \frac{-iH_i t_i}{\hbar} \cdot \exp \frac{-iH_j t_j}{\hbar} \cdot \exp \frac{-iH_i t_i}{\hbar} \cdot |\Psi(0)\rangle \quad (3.6)$$

where t_i is chosen so that the rotation is smaller than π and the only variable t_j is calculated so that the loop is closed, i.e., $|\Psi(t)\rangle \equiv \exp i\phi|\Psi(0)\rangle$.

The detuning of the microwave source cannot be changed during the

very short experiment. In the experiment, case b) was realised with a fixed detuning of $\delta = 24$ kHz by suddenly changing the resonant Rabi frequency from $\Omega_R = 36.7$ kHz to $\Omega_R = 26.4$ kHz and back so that the system still evolves on a closed loop. Case c) utilises a fixed detuning of $\delta = 16$ kHz and a sudden transition of the Rabi frequency from $\Omega_R = 36.7$ kHz to $\Omega_R = 19.9$ kHz and back, again ensuring that the system evolves on a closed loop.

The corresponding trajectories on the Bloch sphere are pictorially represented in Fig. 3.4. For all three cases we performed reference evolution 1, obtaining the phase ϕ_1 ; measurement-free evolution, obtaining the phase ϕ_3 ; and Zeno evolution, obtaining the phase ϕ_4 . The differences of the measured phases are in satisfactory agreement with the theoretical prediction of Eq. (3.4), which confirms their geometric nature.

Chapter 4

Quantum Zeno effect assisted noise sensing

In the ideal quantum Zeno effect, repeated projective measurements are able to protect the coherent dynamics of a quantum system. In contrast, here we consider projective measurements carried out at a variable low rate on the microwave transition between two hyperfine states (the so-called weak quantum Zeno regime), which allows us to perform a short-time Fourier transform of the Rabi frequency of the two-level coupling. Consequently, it is possible to extract pieces of information relating to the signal spectrum, such as its central frequency or bandwidth, and hence build a sensor for semiclassical field fluctuations. In this chapter, a theoretical framework is developed which shows how to combine the controlled manipulation of a quantum two-level system used as a probe and a sequence of projective measurements in order to have direct access to the noise correlation function. The effectiveness of the proposed noise sensing method is experimentally tested with a properly engineered Bose-Einstein condensate of ^{87}Rb atoms realised on an atom chip. We believe that this quantum-Zeno-based approach can open a new path towards novel quantum-based sensing devices. However, more precise methods to distinguish different shapes of the spectra, such as a normal distribution or a Cauchy distribution, still need to be designed. A preprint paper on arXiv [2] of manuscript accepted by the New Journal of Physics summarises this work.

All quantum information theories require coherence within a system to be maintained in order for a quantum computer to function. However, it is impossible to manipulate or investigate a quantum system without perturbing the system. Coupling the quantum system to an environment during a procedure causes it to lose its coherence, and decoherence eventually leads to information losses in the system. The preservation of quantum coherence [48, 49],

or, conversely, the measurement of environmental effects on a quantum system [50] is crucial for improving quantum technologies. ‘Quantum sensing’ denotes all techniques that allow a quantum system to be considered as a *sensor* by exploiting genuine quantum features (e.g. entanglement) to enhance measurement performance [51, 52]. Accordingly, the sensing of field fluctuations induced by an external environment – known as ‘noise sensing’ [53, 54, 55, 56] – also falls within such a framework.

4.1 Generating noise with an arbitrary spectrum

4.1.1 Spectrum of a real noise

Using the Wiener-Khinchin theorem for a stationary random process, the spectrum of real noise can be written as

$$S_n(\nu) = \int_{-\infty}^{\infty} \langle \Omega_n(t)\Omega_n(t-\tau) \rangle e^{-2\pi i\nu\tau} d\tau \quad (4.1)$$

Defining $\Gamma_n(t) = \Omega_n(-t)$, Eq. (4.1) becomes

$$\begin{aligned} S_n(\nu) &= \int_{-\infty}^{\infty} \langle \Omega_n(t)\Gamma_n(\tau-t) \rangle e^{-2\pi i\nu\tau} d\tau \\ &= \int_{-\infty}^{\infty} \left(\int_{-\infty}^{\infty} \Omega_n(t)\Gamma_n(\tau-t) dt \right) e^{-2\pi i\nu\tau} d\tau \\ &= \int_{-\infty}^{\infty} (\Omega_n * \Gamma_n)(\tau) e^{-2\pi i\nu\tau} d\tau \\ &= \mathcal{FT}(\Omega_n * \Gamma_n)(\nu) \\ &= \mathcal{FT}(\Omega_n)(\nu) \cdot \mathcal{FT}(\Gamma_n)(\nu) \end{aligned} \quad (4.2)$$

Meanwhile, the Fourier transform of the noise signal can be expressed as

$$\begin{aligned} \mathcal{FT}(\Gamma_n)(\nu) &= \int_{-\infty}^{\infty} \Gamma_n(t) e^{2\pi i\nu t} dt \\ &=_{t \rightarrow -t} \int_{-\infty}^{\infty} \Gamma_n(-t) e^{2\pi i\nu(-t)} (-dt) \\ &= - \int_{-\infty}^{\infty} \Omega(t) e^{2\pi i(-\nu)t} dt \\ &= \mathcal{FT}(\Omega_n)(-\nu) \end{aligned} \quad (4.3)$$

Since $\Omega_n(t)$ is real, its Fourier transform satisfies the reality condition $\mathcal{FT}(\Omega_n)(-\nu) = \mathcal{FT}^*(\Omega_n)(\nu)$. Substituting this into Eq. (4.2), a relation between the spectrum of the noise and its Fourier transform is obtained:

$$S_n(\nu) \propto |\mathcal{FT}(\Omega_n)(\nu)|^2 \quad (4.4)$$

4.1.2 Sampling a real noise

It is straightforward to see that the noise signal corresponding to a spectrum with a single frequency component ν_0 (i.e., a noise with frequency spectrum is a Dirac centered at ν_0) takes a sinusoidal form with a random phase in the temporal domain:

$$\Omega_n(t) \propto \sin(2\pi\nu_0 t + \phi) \quad (4.5)$$

with ϕ randomly distributed between $[0, 2\pi]$, described by a stochastic process.

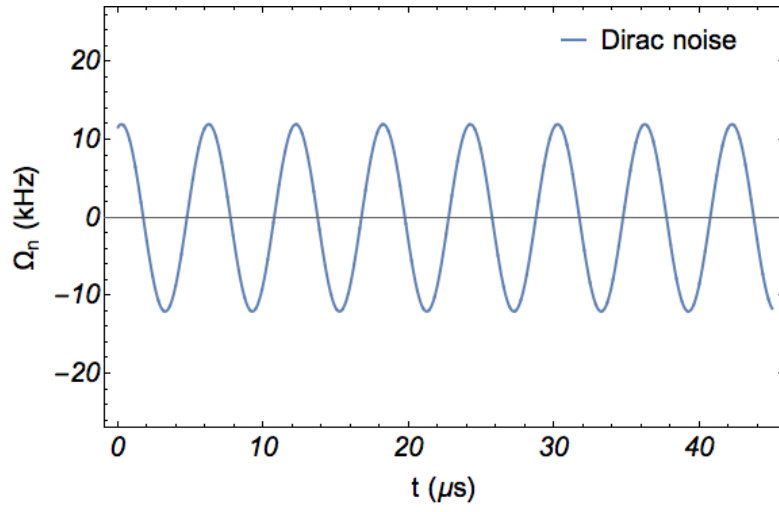
However, in the case of a more general noise spectrum, the analytical formula for the temporal signal is not directly obtained from the desired spectrum profile. Instead, we start by inspecting the positive frequency components of white noise, i.e., a random signal having equal intensity at different frequencies. As the normalisation of the temporal signal appears in the last step, the normalisation factor may be neglected at this stage. All the frequency components in the spectrum are set to 1, which means that

$$\mathcal{FT}(x_{white})(\nu) = e^{i\phi(\nu)}, \nu > 0 \quad (4.6)$$

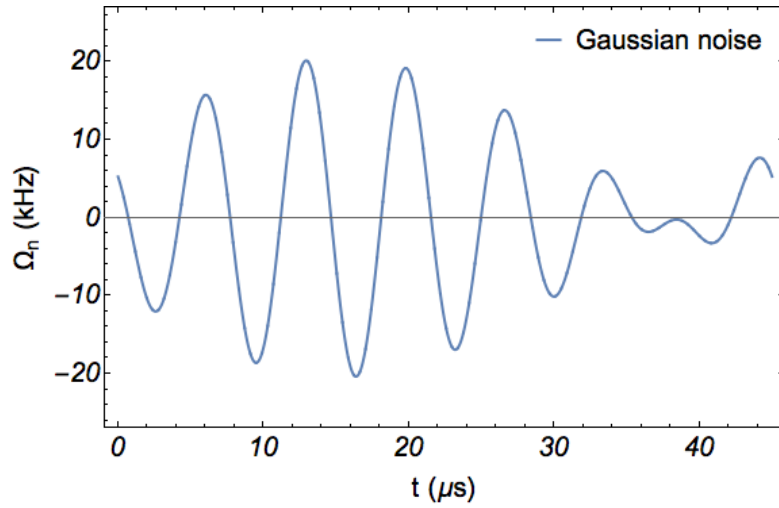
with $\phi(\nu)$ randomly distributed between $[0, 2\pi]$. The spectrum may then be shaped as desired, with more intensity in certain frequencies than in others. For this purpose, we write the frequency distribution in terms of a real function g_d , following equation 4.4, as

$$\mathcal{FT}(x_d)(\nu) = \sqrt{g_d(\nu)} e^{i\phi(\nu)}, \nu > 0 \quad (4.7)$$

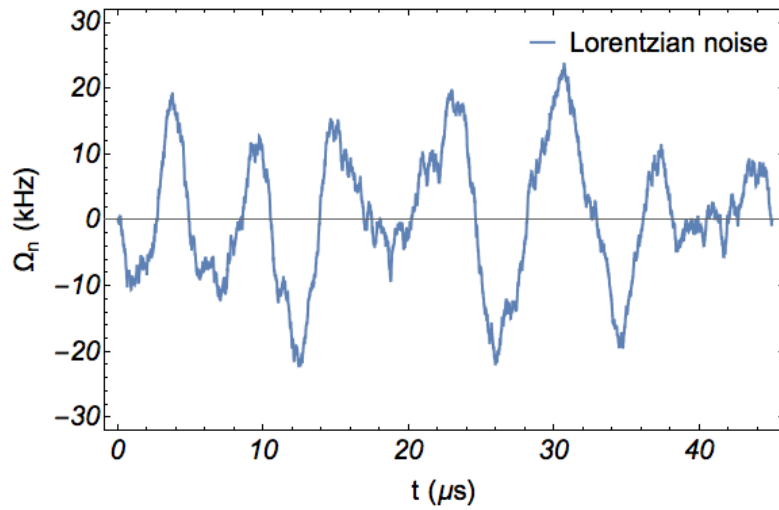
We choose to work with noise whose spectrum profiles follow a normal distribution (described by a Gaussian function) and a Cauchy distribution (described by a Lorentzian function). The normal distribution shows limited fluctuations of the noise frequency around the central frequency ν_0 , while the Cauchy distribution allows noise with frequency components even many standard deviations away from the central frequency with a non-negligible probability.



(a) Dirac spectrum



(b) Gaussian spectrum



(c) Lorentz spectrum

$$g_{\text{Gaussian}}(\nu) = \exp\left(-\left(\frac{\nu-\nu_0}{\sigma_\nu}\right)^2\right) \quad (4.8)$$

$$g_{\text{Lorentzian}}(\nu) = \frac{1}{1+\left(\frac{\nu-\nu_0}{\gamma\nu}\right)^2} \quad (4.9)$$

In order to obtain real noise, the reality condition must be respected when constructing the non-positive part of the spectrum. Negative frequency components can be deduced by conjugating the positive spectrum. Note that for this condition to be satisfied the component at $\nu = 0$ must have a real value.

$$\mathcal{FT}(x_d)(\nu) = \overline{\mathcal{FT}(x_d)(-\nu)} \quad (4.10)$$

$$\mathcal{FT}(x_d)(0) = \overline{\mathcal{FT}(x_d)(0)} = \sqrt{g_d(0)} \quad (4.11)$$

The inverse Fourier transform of the expression above gives the temporal noise signal $x(d)$ with the desired spectral distribution g_d . Finally, the signal should be normalised; in this case, the normalisation is determined by setting the amplitude of the Rabi frequency.

The noise field should have the same power for a better comparison and should be $\approx 25\%$ the maximum power that can be produced by the microwave field driving the hyperfine transition.

The energy given to the system by a microwave field \vec{E} is:

$$W = \frac{1}{\epsilon_0} \left| \vec{E} \right|^2 \quad (4.12)$$

The power is its time average:

$$Pw = \langle W \rangle_T = \left\langle \frac{1}{\epsilon_0} E^2 \right\rangle_T \quad (4.13)$$

The relation between the field amplitude and the induced Rabi frequency is:

$$\Omega \propto \vec{d} \cdot \vec{E} \propto \left| \vec{E} \right| \quad (4.14)$$

It is sufficient to normalise the time average of the Rabi frequency amplitude:

$$\begin{aligned} Pw &\equiv \langle |\Omega(t)|^2 \rangle_T \\ &= \lim_{T \rightarrow \infty} \frac{1}{T} \int_0^T |\Omega(t)|^2 dt \end{aligned} \quad (4.15)$$

To set the correct Rabi frequency amplitude, we fix the ratio between the power of the noise Pw_n and the maximum power of the microwave field $Pw_{max} = \langle |\Omega_{max}(t)|^2 \rangle_T$.

The microwave field is mixed with a discrete control temporal signal at the sampling rate of the noise $S_{rate} = 4\text{ ns}$. An array A of $N/2$ points, with $N = \frac{T}{S_{rate}}$, randomly uniformly distributed on the unit circle $\exp(i\phi)$, represents the positive part of the white noise component. After incorporating the sampling rate, the distribution functions become

$$g_{Gaussian}(i) = \exp\left(-4\left(\frac{i-\nu_0 T/2}{\sigma T/2}\right)^2\right) \quad (4.16)$$

$$g_{Lorentzian}(i) = \frac{(\sigma T/2)^2}{(i-\nu_0 T/2)^2 + (\sigma T/2)^2} \quad (4.17)$$

with $i \in [1, N/2]$ the index of the array. Note that the central frequency is located at element number $\nu_0 T/2$ and its standard deviation is $\sigma T/2$ points. The initial array is now replaced by

$$A(i) := \sqrt{g_d(i)} * A(i) \quad (4.18)$$

To satisfy the reality condition, the reverse conjugate of the array is added to the end of the list and the real value for the zero-frequency component is added in the middle, giving a total of $N + 1$ elements. Finally, applying an inverse Fourier transform and normalising the amplitude produces the discrete temporal signal sampled for the experiment.

4.2 Sensing scheme in the WQZ regime

Under the effect of a time-dependent Hamiltonian $H(t)$, a state evolves from $|\psi(t_0)\rangle$ into $|\psi(t)\rangle = e^{-iA(t,t_0)}|\psi(t_0)\rangle$, with $A(t, t_0) = 1/\hbar \int_{t_0}^t H(t')dt'$. If the system is repeatedly projected into a given state, its dynamics can be effectively frozen in the QZ regime. This is obtained when the time interval τ between consecutive projections is small compared to $\tau_Z = \hbar/\sqrt{\text{Var}(H)}$, where $\text{Var}(H)$ is the variance of the Hamiltonian $H(t)$ with respect to the initial state $|\psi(t_0)\rangle$ (see the first chapter and Ref. [11]). If, on the contrary, τ approaches τ_Z , i.e., $\tau = \mathcal{O}(\tau_Z)$, the system is in the WQZ regime [57]. In this limit the survival probability P , namely the probability of finding the system in the initial state, decreases quadratically with the expectation value of $A(t + \tau, t)$, always computed with respect to the initial state. When the QZ requirement on the time interval between subsequent measurements is relaxed (i.e., in the WQZ regime), it is possible to find a condition where the

survival probability P is maximally sensitive to an external field. Intuitively, if the projective measurements are too close to each other (pure QZ), the effect of any signal to be measured is inhibited ($P \sim 1$). On the other hand, if projective measurements are too sparse, P decays to zero regardless of the presence of an external field.

In the WQZ regime, a method can hence be devised to extract information about a faint noise signal by amplifying its effect with the use of a suitable control field. Let us better illustrate this by introducing the model adopted in our experiment. Consider a quantum system with only two levels, $|0\rangle$ and $|1\rangle$, which are eigenstates of the computational basis, and take $|\psi(0)\rangle = |0\rangle$ as the initial state. The system is driven with the Hamiltonian

$$H(t) = \frac{\hbar}{2} [\Omega_c(t) + \Omega_n(t)] \sigma_x, \quad (4.19)$$

where $\Omega_c(t)$ is the control field, σ_x is a Pauli matrix and $\Omega_n(t)$ is the unknown stochastic field to be characterised. While the system evolves, a sequence of N measurements separated by a time interval of τ is applied. By defining

$$\alpha_j \equiv \int_{(j-1)\tau}^{j\tau} [\Omega_c(t) + \Omega_n(t)] dt, \quad (4.20)$$

the probability P of finding the system in the initial state after N measurements takes the form

$$\begin{aligned} P &= \prod_{j=1}^N |\langle 0|U(j\tau, (j+1)\tau)|0\rangle|^2 \\ &= \prod_{j=1}^N |\langle 0|\exp(-i/\hbar)\alpha_j\sigma_x|0\rangle|^2 \\ &= \prod_{j=1}^N \left| \begin{bmatrix} 1 & 0 \\ -i \sin \alpha_j & \cos \alpha_j \end{bmatrix} \begin{bmatrix} 1 \\ 0 \end{bmatrix} \right|^2 \\ &= \prod_{j=1}^N \cos^2 \alpha_j. \end{aligned} \quad (4.21)$$

Equation (4.21) describes the relative decay of the survival probability P , which is given by the product of the survival probabilities in each time interval between two measurements. Then, following Ref. [57], a second-order approximation based on the condition $\alpha_j^4 \ll 1$ that defines the WQZ regime

can be applied. As a result, P can be factorized into three contributions, i.e.,

$$\begin{aligned}
P &= \exp \left(\ln \left(\prod_{j=1}^N \cos^2 \alpha_j \right) \right) = \exp \left(\sum_{j=1}^N \ln (\cos^2 \alpha_j) \right) \\
&= \exp \left(\sum_{j=1}^N \ln \left(\left(1 - \frac{\alpha_j^2}{2} + \mathcal{O}(\alpha_j^4) \right)^2 \right) \right) \\
&= \exp \left(\sum_{j=1}^N \ln (1 - \alpha_j^2 + \mathcal{O}(\alpha_j^4)) \right) = \exp \left(- \sum_{j=1}^N \alpha_j^2 + \mathcal{O}(\alpha_j^4) \right) \quad (4.22) \\
&\approx_{\alpha_j^4 \ll 1} \exp \left(- \sum_{j=1}^N \alpha_j^2 \right) \\
&= \exp \left[- \sum_{j=1}^N \left(\int_{(j-1)\tau}^{j\tau} (\Omega_c(t) + \Omega_n(t)) dt \right)^2 \right] \\
&= P_c P_n P_{\text{cn}},
\end{aligned}$$

where

$$P_c \equiv \exp \left[- \sum_{j=1}^N \left(\int_{(j-1)\tau}^{j\tau} \Omega_c(t) dt \right)^2 \right], \quad (4.23)$$

$$P_n \equiv \exp \left[- \sum_{j=1}^N \left(\int_{(j-1)\tau}^{j\tau} \Omega_n(t) dt \right)^2 \right], \quad (4.24)$$

$$P_{\text{cn}} \equiv \exp \left[-2 \sum_{j=1}^N \left(\int_{(j-1)\tau}^{j\tau} \Omega_c(t) dt \right) \left(\int_{(j-1)\tau}^{j\tau} \Omega_n(t') dt' \right) \right]. \quad (4.25)$$

P_c depends only on the control pulse and thus it can be directly computed, while $P_n \sim 1$ since $\ln(P_n)$ is a second-order term in Ω_n , which can be neglected for *weak* noise. Finally, P_{cn} is a cross term involving both the noise and the control pulse and containing all the interesting information on the spectral properties of $\Omega_n(t)$. In other words, a measurement of the survival probability P gives direct access to $P_{\text{cn}} \approx P/P_c$. In this regard, it is worth noting that the validity of the weak noise condition implies that the combination of noise and all the sequences of measurements (in the absence of the control field) correspond to the *strong* (stochastic) QZ regime [57]: the atoms are likely to remain in the initial state. It is the action of the control field that makes the WQZ regime accessible for the system.

4.2.1 Visualisation: Weak quantum Zeno regime as STFT

Let us examine the cross term, the product of the values of the control Rabi frequency and the noise Rabi frequency in $P_{cn} = \frac{P}{P_{cc}}$. This section offers a quantitative visualisation of the method presented above as a short-time Fourier transform (STFT) through simple approximations, while the next section will give the detailed calculations for exploiting the sensing methods. As was also shown above, the Fourier transform gives direct access to the spectrum of the noise, through the Wiener-Khintchin theorem.

$$-\frac{1}{2} \ln \left(\frac{P}{P_{cc}} \right) (\tau) = \sum_{j=0}^{N-1} \left(\int_{t=j\tau}^{(j+1)\tau} \Omega_c(t) dt \right) \left(\int_{t=j\tau}^{(j+1)\tau} \Omega_n(t) dt \right) \quad (4.26)$$

Since only the mean value during the time interval $[(j-1)\tau, \tau]$ matters, Ω_c is chosen to be constant over each interval $[(j-1)\tau, \tau]$. While in a conventional Fourier transform the signal is projected onto a basis of $\exp(2i\pi\nu t)$, which averages out to zero if the frequency ν is out of the noise variation range, here we can only project on a step function due to the time average.

Instead a square function $\Omega_c(t) = \Omega_0(-1)^j = \Omega_0(-1)^{\lfloor \frac{t}{\tau} \rfloor}$ is chosen such that when the signal is projected onto it, it will average out to zero if the frequency $\nu = \frac{1}{\tau}$ is out of the noise variation range.

$$\begin{aligned} \Omega_c(t) &= \Omega_0(-1)^j = \Omega_0(-1)^{\lfloor \frac{t}{\tau} \rfloor} = \Omega_0(-1)^{\lfloor 2\nu t \rfloor} \\ &= \frac{4\Omega_0}{\pi} \sum_{k=0}^{\infty} \frac{\sin((2k+1)2\pi\nu t)}{(2k+1)} \\ &= \frac{4\Omega_0}{\pi} \left(\sin(2\pi\nu t) + \frac{1}{3}\sin(2\pi(3\nu)t) + \frac{1}{5}\sin(2\pi(5\nu)t) + \dots \right) \end{aligned} \quad (4.27)$$

with $\nu = 1/(2\tau)$.

Equation (5.3) then become

$$\begin{aligned} -\frac{1}{2} \ln \left(\frac{P}{P_{cc}} \right) (\nu) &= \frac{4\Omega_0}{\pi} \int_0^{N\tau} \Omega_n(t) \left(\sum_{k=0}^{\infty} \frac{\sin((2k+1)2\pi\nu t)}{(2k+1)} \right) dt \\ &\xrightarrow{N \rightarrow \infty} \frac{4\Omega_0}{\pi} \sum_{k=0}^{\infty} \text{Im}(\mathcal{F}(\Omega_n)((2k+1)\nu)) \end{aligned} \quad (4.28)$$

In the case where the noise spectrum is not close to the origin (i.e., the spectrum bandwidth Δf is smaller than one-third of the central frequency, $f_0/3$), if the function is evaluated in the range of the spectrum, 1st, 3rd and higher harmonics will not be mixed. Observe that the first harmonic corresponds to a conventional short time Fourier transform.

Even for a spectrum which is not compactly supported, such as a Lorentzian, the contribution of other harmonics is significant. Through the outcome of the measurements, a quantitative guess could still be made about the noise's central frequency and bandwidth when the region of the noise spectrum is a few bandwidth away the origin.

In the case where the first harmonic may be separated from the others,

$$\begin{aligned} -\frac{1}{2} \ln \left(\frac{P}{P_{cc}} \right) (\nu) &= \frac{4\Omega_0}{\pi} \text{Im} (\mathcal{F} (\Omega_n) (\nu)) \\ &= \frac{4\Omega_0}{\pi} |\mathcal{F} (\Omega_n) (\nu)| \sin (\text{Arg} [\mathcal{F} (\Omega_n) (\nu)]) \end{aligned} \quad (4.29)$$

The square gives

$$\ln \left(\frac{P_{cn}}{P_{cc}} \right)^2 (\nu) \propto |\mathcal{F} (\Omega_n) (\nu)|^2 \sin^2 (\text{Arg} [\mathcal{F} (\Omega_n) (\nu)]) \quad (4.30)$$

Define χ as the average over many realisations:

$$\chi = \langle \ln \left(\frac{P}{P_{cc}} \right)^2 (\nu) \rangle \propto |\mathcal{F} (\Omega_n) (\nu)|^2 \quad (4.31)$$

with $\langle \sin^2 (\text{Arg} [\mathcal{F} (\Omega_n) (\nu)]) \rangle = 1/2$ for a stochastic function Ω_n , and, according to section 4.1.1, the measured result is simply

$$\chi \propto S_n(\nu) \quad (4.32)$$

4.2.2 Spectrum reconstruction

Now, let us rewrite equation (4.25) as

$$\ln (P_{cn}) = -2 \int_0^{N\tau} \tilde{\Omega}_c(t) \Omega_n(t) dt, \quad (4.33)$$

where we have defined

$$\tilde{\Omega}_c(t) \equiv \sum_{j=1}^N \left(\int_{(j-1)\tau}^{j\tau} \Omega_c(t') dt' \right) \mathcal{W}_j(t) \quad (4.34)$$

with the rectangular window function

$$\mathcal{W}_j(t) \equiv \begin{cases} 1, & (j-1)\tau \leq t < j\tau \\ 0, & \text{otherwise.} \end{cases} \quad (4.35)$$

Equation (4.33) naturally suggests the possibility of sampling the noise with a filter function dictated by modulating the control field. Notice that, since $\tilde{\Omega}_c(t)$ is a piecewise function that is constant between each pair of measurements, the periodicity of the control field $\Omega_c(t)$ can naturally be chosen to be a multiple of τ .

Thus, by averaging $\ln^2(P_{\text{cn}})$ over different experimental realisations, we can directly obtain the *second-order correlation function* $\chi_N^{(2)}$, which quantifies the correlations between noise and control. In particular, it can be proven that

$$\langle \ln^2(P_{\text{cn}}) \rangle = \int_0^{N\tau} \int_0^{N\tau} \tilde{\Omega}_c(t) \tilde{\Omega}_c(t') \langle \Omega_n(t) \Omega_n(t') \rangle dt dt' \equiv \chi_N^{(2)}, \quad (4.36)$$

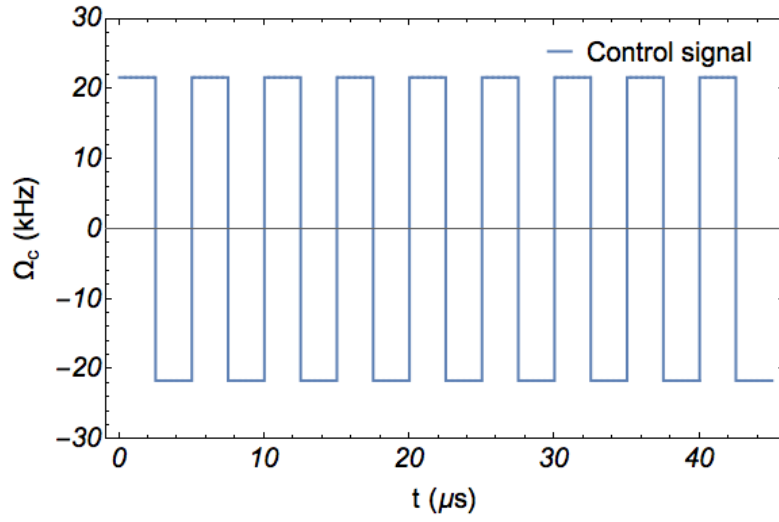
where it has been assumed, without loss of generality, that the average of the noise (a real, stationary stochastic process) over a sufficiently large number of realisations is zero at each time instant t . As a matter of fact, noise with a non-zero average can be mathematically modelled as a part of the control field. Through Eq. (4.36) we have access to $\langle \Omega_n(t) \Omega_n(t') \rangle$, which is the noise autocorrelation function [50]. Introducing the noise power spectral density $S(\omega)$ as the Fourier transform of the autocorrelation function, $\chi_N^{(2)}$ may be expressed in the frequency domain as

$$\chi_N^{(2)} = \int_0^\infty S(\omega) F(\omega) d\omega, \quad (4.37)$$

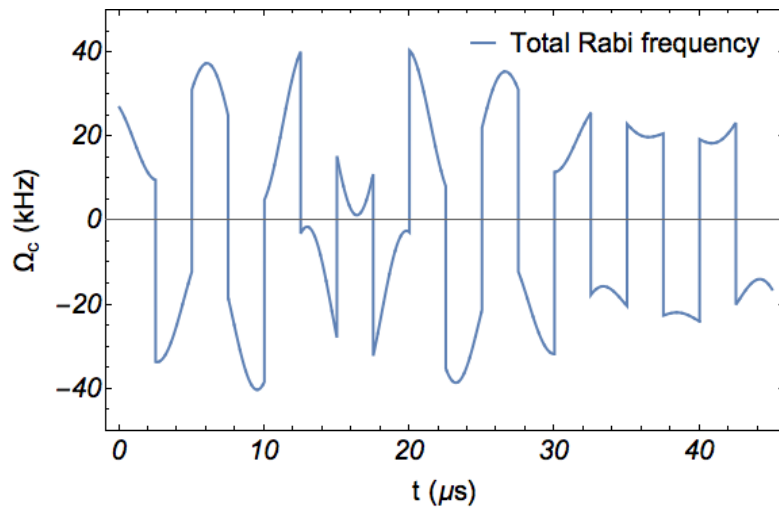
where the *filter function* $F(\omega) \equiv \frac{1}{2\pi} \left| \int_0^{N\tau} \tilde{\Omega}_c(t) e^{-i\omega t} dt \right|^2$ is the absolute square of the short-time Fourier transform of the normalised control field. Once again, it is worth noting that Eq. (4.37) holds true only if the noise is a stationary process and thus its power spectral density does not change over time. Therefore, by measuring $\chi_N^{(2)}$ for different choices of the control pulse $\tilde{\Omega}_c(t)$, the power spectral density $S(\omega)$ of the noise in different frequency regimes may be inferred.

4.3 Experimental implementation

The noise sensing protocol requires driving the $|0\rangle \rightarrow |1\rangle$ transition. To achieve this, we use a resonant microwave field with an amplitude that is



(a) Control pulse



(b) Total pulse

Figure 4.2: Rabi frequency used in the experiment

modulated by a zero-average square wave with period 2τ , i.e.,

$$\Omega_c(t) = \sum_{j=1}^N (-1)^j \Omega_0 \mathcal{W}_j(t), \quad (4.38)$$

with $\Omega_0 = 2\pi \times 43.3$ kHz. Then, corresponding to each switch of the control Hamiltonian, i.e., at $t = j\tau$, a projective measurement is applied. The number of projective measurements is limited by the stability of the light pulse generator to $N = 18$. In the experiment the minimum repetition time $\tau_{min} > 2 \times 0.6 \mu\text{s}$ is limited by the duration of the light pulse implementing the projection operator. Moreover, it is necessary to have $N\tau_{max} < 100 \mu\text{s}$ because of experimental decoherence.

The Rabi frequency sequence used for the experiment is shown in Fig. 4.2. Note that it is important to adjust the control signal so that at the repetition time $\tau_0 = \frac{1}{2\pi\Omega_{n0}}$, the survival probability $P_c = e^{-1/2} \approx 60\%$. In this way, the effect of the noise at its central frequency falls at the maximum sensitivity point of the control curve.

Figure 4.3 shows, in red, the experimental survival probability \mathcal{P} , i.e., the probability for an atom to remain in the initial state $|0\rangle$, as a function of τ . In this case, $\mathcal{P} = P_c$ and exponentially decreases with the square of τ , in perfect agreement with Eq. (4.23) (continuous red line). Following the protocol, the noise field is represented by a resonant microwave with a time-dependent amplitude. As a preliminary measurement, a modulation is applied with a single frequency component, producing $\Omega_n(t) = \Omega_{n0} \sin(\omega t + \phi)$, with $\Omega_{n0} = 2\pi \times 12$ kHz and $\omega = 2\pi \times 167$ kHz.¹ In Fig. 4.3, the survival probability \mathcal{P} is shown (in blue) as a function of τ with noise alone and $\phi = 0$. In this case, $\mathcal{P} = P_n$ is compatible with 1 within the experimental errors, thus confirming the hypothesis $P_n \sim 1$.

The effect of Ω_n is amplified by the control field, as shown in Fig. 4.4. This exemplifies the working principle of the sensing method. Indeed, by switching the phase ϕ , the survival probability is either increased (for $\phi = 0$) or decreased (for $\phi = \pi$). As a consequence, when ϕ is randomly chosen from a uniform probability distribution in the range $[0, 2\pi]$, the average of the survival probability coincides with that due to the control field alone, i.e., $\langle \mathcal{P} \rangle = P_c$. Meanwhile, its variance $\sqrt{\text{Var}(\mathcal{P})}$ is maximised when the repetition rate corresponds to half the frequency of the noise component, i.e., $1/\tau \sim \omega/\pi$.

The $\chi^{(2)}$ extracted directly from the measurements confirms that the experiment gives a sort of STFT, giving information on the central noise

¹This value is the central frequency of all the noise power spectral densities. It has been chosen so that the sensitivity of \mathcal{P} with respect to the action of the control is maximised.

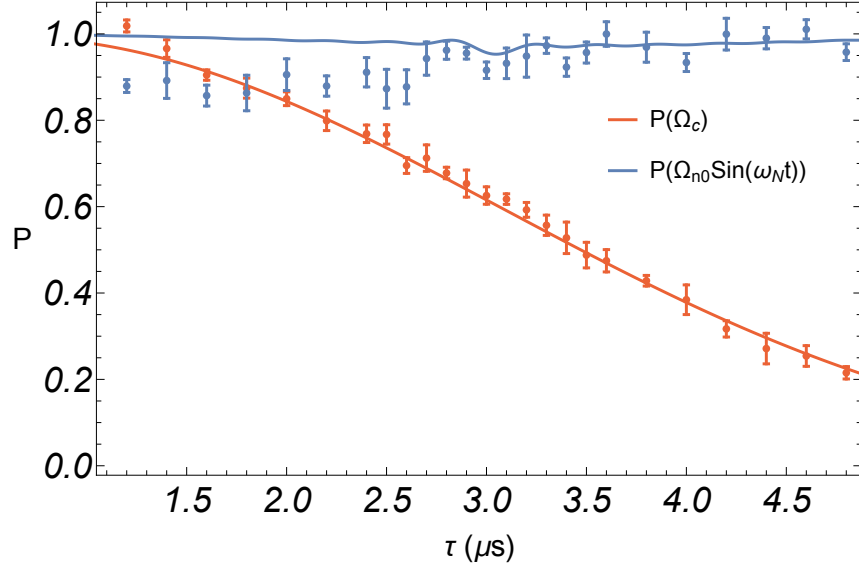


Figure 4.3: Survival probability \mathcal{P} as a function of τ , recorded with only the control field Ω_c (in red) and only the noise signal Ω_n (in blue). The dots are the experimental results, while the continuous lines show the dynamics of the system as predicted by Eqs. (4.23) and (4.24). Notice that, since the RF pulse used for normalisation can produce a rotation that drifts slightly away from $\pi/2$ between one realisation and another, it is possible to experimentally measure values of the survival probability higher than one.

frequency (see Fig. 4.5). The profile bandwidth decreases with the time windows, so the wider the time windows are, the better the resolution in analysing the given Dirac spectrum (a spectrum with only one frequency component).

In Fig. 4.6, we show the experimental, numerical, and theoretical $\chi_N^{(2)}$ values for the same number of realisations $Q = 14$ of the protocol, which exhibit remarkably good agreement. By increasing Q , the numerical data (obtained by simulating the time dynamics for different realisations of the noise) approach the theoretical curve (calculated from Eq.) which, in the case of a single noise component for a finite time window, is a sinc^2 function. In the experiment the noise can be switched off to give direct access to P_c , so this value is used instead of the average of \mathcal{P} over 14 realisations.

To demonstrate the protocol in a more realistic scenario, the experiment was repeated using two broader Gaussian and Lorentzian noise power spectral densities, both centred at 167 kHz with the same width of 50 kHz (FWHM for the Lorentzian, 2σ for the Gaussian). Both experiments and simulations

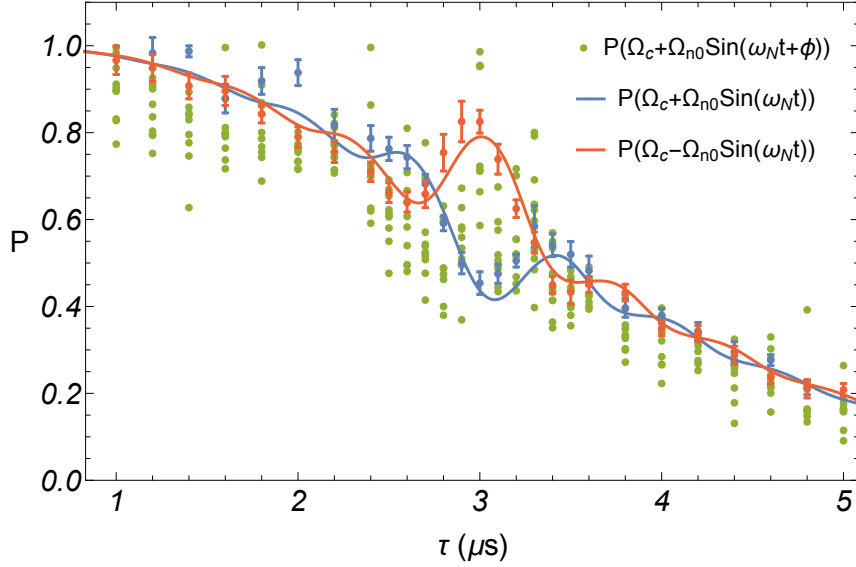
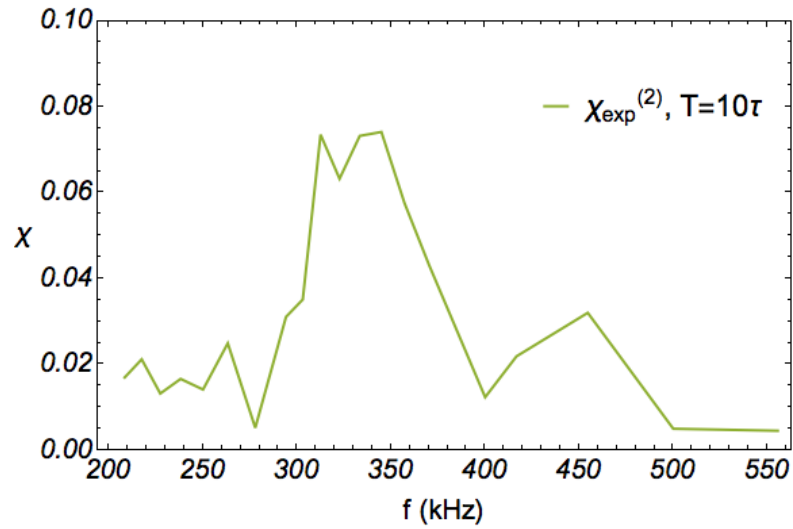


Figure 4.4: Survival probability \mathcal{P} as a function of τ in the presence of the control field, denoted as Ω_c in the legend, and different noise signals Ω_n . In red: sinusoidal signal without additional phase; in blue: sinusoidal signal with opposite phase. The dots are the experimental results, while the continuous lines denote the prediction of Eq. (4.25). Moreover, the green dots show the fluctuations recorded for a sinusoidal noise signal with a random phase, i.e., noise with a single frequency component.

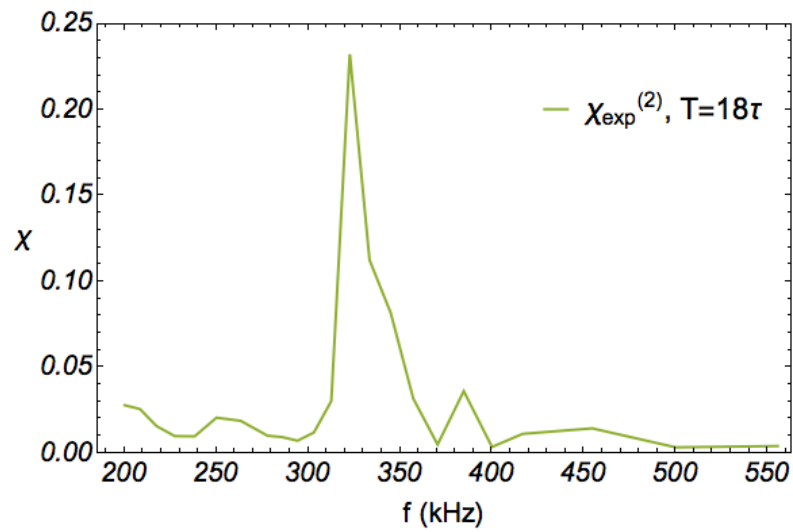
qualitatively agree with the applied noise spectra; see Figs. 4.7 and 4.8 for the second-order correlation functions and Figs. 4.9 and 4.10 for the power spectral densities. In these figures, the experimental data and theoretical curves are presented together with data obtained from numerical simulations of the quantum probe dynamics. In particular, Fig. 4.7 shows the normalised (L_2 -norm) second-order correlation functions for both scenarios. Figure 4.8 shows the overlap (fidelity \mathcal{F} defined below) between the experimental and numerical data points $\chi^{(data)}(\tau_k)$ (τ_k are the K different values of τ with $k = 1, \dots, K$ for which the measurements are repeated Q times) and the theoretical values $\chi^{(teo)}(\tau_k)$ from Eq. (4.37), i.e.,

$$\mathcal{F} = \sum_{k=1}^K \chi^{(data)}(\tau_k) \chi^{(teo)}(\tau_k). \quad (4.39)$$

Next, in Fig. 4.9 the power spectral densities of the noise fields are analysed. By means of a filter orthogonalisation protocol [58], the power spectral



(a) $\chi^{(2)}$ measured for a noise with Dirac spectrum, with 10 Zeno measurements



(b) $\chi^{(2)}$ measured for a noise with Dirac spectrum, with 18 Zeno measurements

Figure 4.5: Second-order correlation function measured for a single frequency component spectrum

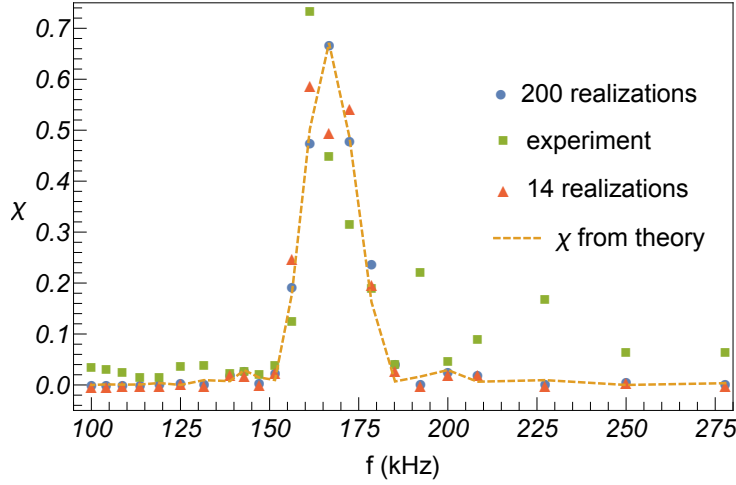
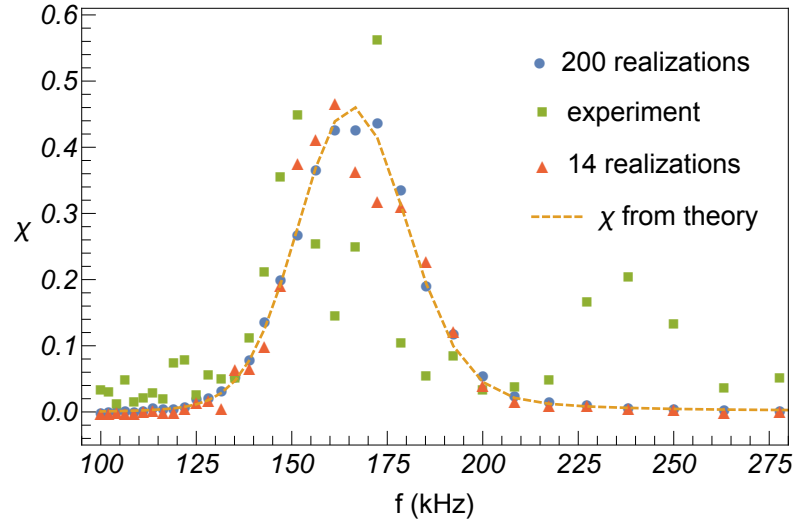
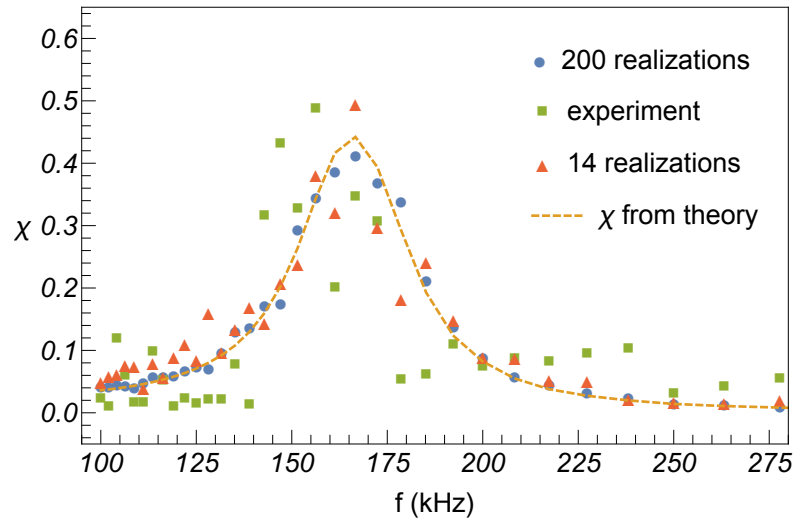


Figure 4.6: Second-order correlation function $\chi_N^{(2)}$ as a function of frequency for finite single-frequency-component noise with random phase. For $Q = 14$ the green squares show the experimental results, while the dashed yellow line denotes the theoretical curve obtained by evaluating Eq. (4.37). Simulating the time dynamics yields numerical values for both $Q = 14$ (red triangles) and $Q = 200$ (blue circles).

density of the noise can be reconstructed from the data points $\chi^{(data)}(\tau_k)$, corresponding to the measurement of the overlap between the filter $F_k(\omega)$ and the original spectrum $S^{(orig)}(\omega)$ as given by Eq. (4.37). This technique allows the reconstruction of a given noise spectral density in the K -dimensional function space spanned by the filter functions $F_k(\omega)$, by calculating an orthonormal basis $\hat{F}_k(\omega)$ of this space. In this case the procedure is highly recommended, since the window functions of the finite pulse length lead to very broad filter functions $F_k(\omega)$, comparable to the spectral width of the noise signal, which are non-orthogonal. We derive the overlap between the filter functions $F_k(\omega)$ in the frequency domain, i.e., we compute the symmetric matrix A whose matrix elements are $A_{kl} \equiv \int_0^{\omega_c} F_k(\omega) F_l(\omega) d\omega$ with $k, l = 1, \dots, K$ and ω_c a cut-off frequency. The matrix A , being symmetric, can always be orthogonalised by means of the transformation $VAV^T = \Lambda$, where the matrix V contains the eigenvectors of A and Λ is a diagonal matrix whose elements are the eigenvalues λ_k , $k = 1, \dots, K$. Thus, the orthonormal basis functions can be written as $\hat{F}_k(\omega) \equiv \frac{1}{\sqrt{\lambda_k}} \sum_{l=1}^K V_{kl} F_l(\omega)$, $k = 1, \dots, K$ (i.e., $\int_0^{\omega_c} \hat{F}_k(\omega) \hat{F}_l(\omega) d\omega = \delta_{kl}$ with δ_{kl} denoting the Kronecker delta) and perform the reconstruction of the noise spectral density in this transformed basis.



(a)



(b)

Figure 4.7: Second-order correlation function $\chi_N^{(2)}$ of (a) Gaussian and (b) Lorentzian noise power spectral densities. Both spectra have the same peak frequency and spectral width. The dashed yellow lines show the theoretical curves given by evaluating Eq. (4.37), while the green squares are the correlation function obtained by experimental measurements with $Q = 14$. Red triangles and blue circles denote the correlation function from numerical simulations of the system dynamics with $Q = 14$ and $Q = 200$, respectively.

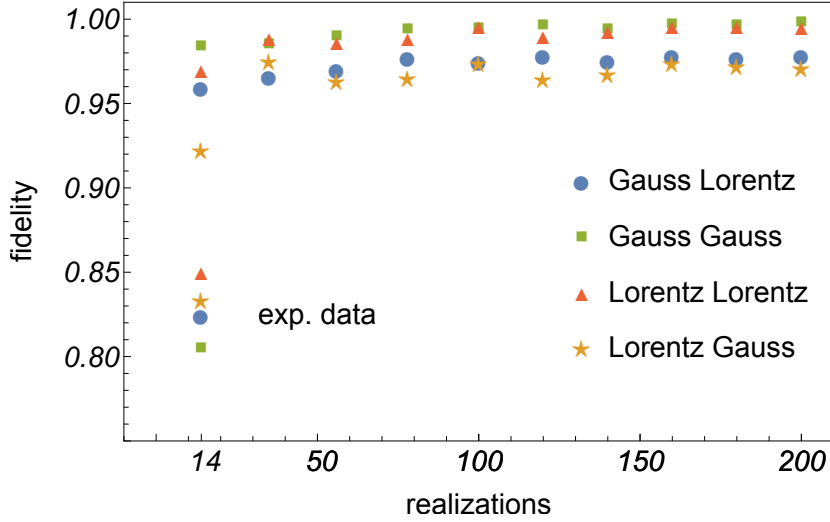


Figure 4.8: Fidelity of the second-order correlation function obtained by comparing the numerical and theoretical data. First, $\chi_N^{(2)}$ evaluated from the Gaussian power spectral density is compared with the *theoretical* curves given by using Lorentzian (blue circles) and Gaussian (green squares) noise spectra. Then, $\chi_N^{(2)}$ evaluated from the Lorentzian noise is compared to the theoretical curves from both Lorentzian (red triangles) and Gaussian (yellow stars) spectral densities. Overall, the fidelity increases with the number of realisations Q . All numerical data points obtained by comparing curves from the same distributions are much closer to 1 than the others. Thus, from the results of the numerical simulations, it is possible to distinguish between Gaussian and Lorentzian spectra. The lower data points on the left, referring to $Q = 14$, are obtained directly from the experimental data.

The expansion of the spectral density in the orthonormal basis is

$$S^{(rec)}(\omega) = \sum_{k=1}^K \hat{c}_k \hat{F}_k(\omega), \quad (4.40)$$

$$\hat{c}_k(\omega) = \int_0^{\omega_c} S^{(orig)}(\omega) \hat{F}_k(\omega) = \frac{1}{\sqrt{\lambda_k}} \sum_{l=1}^K V_{kl} \chi^{(data)}(\tau_l). \quad (4.41)$$

The main advantage of this reconstruction technique is its robustness against the amount of statistical noise, due to the truncation of the orthogonal basis to the dominant eigenvalues; more details can be found in Ref. [58]. Notice that the negative values of the reconstructed power spectral densities are an artefact of the reconstruction method within a larger function space and thus they may be set to zero. Here, the spectra, both the original

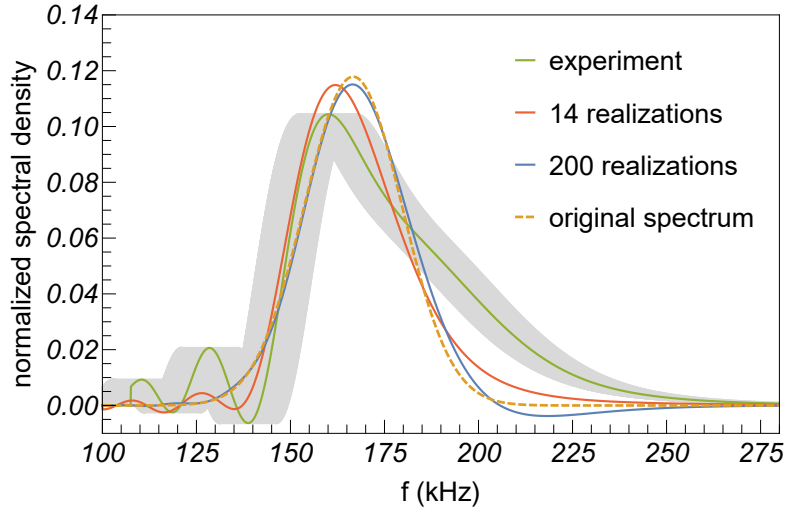
$S^{(orig)}(\omega)$ and the reconstructed version $S^{(rec)}(\omega)$, are normalised by the L_2 norm, and the fidelity is given by the continuous overlap

$$\mathcal{F} = \int_{\omega_{min}}^{\omega_{max}} S^{(teo)}(\omega)S^{(orig)}(\omega)d\omega, \quad (4.42)$$

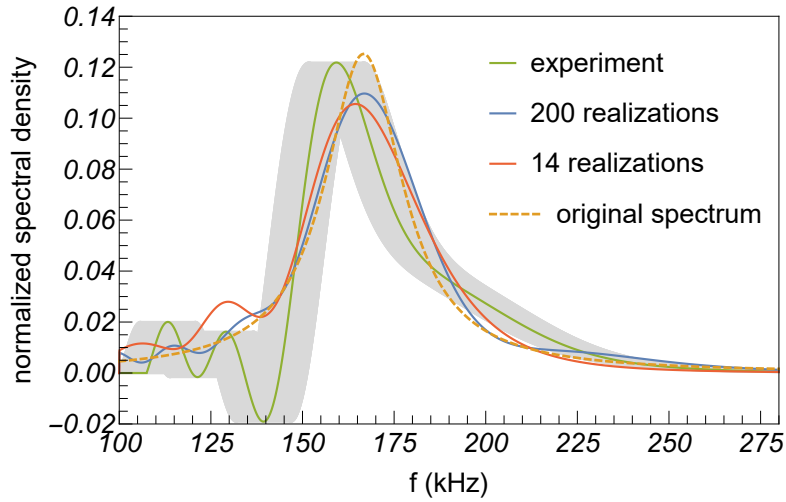
where $\omega_{min} = 2\pi \times 100$ kHz and $\omega_{max} = 2\pi \times 300$ kHz define the frequency range within which the power spectral density of the noise is reconstructed.

From the experimental results it is seen that the reconstructed spectrum resembles the original one, although the peak is shifted to lower frequencies and some residual oscillations are present. We believe that this is an effect of the finite time duration τ_m of the light pulse that implements the Zeno projective measurements. This effect may be taken into account by considering an uncertainty of $\pm\tau_m/2$ around each τ , represented by a shaded area in Fig. 4.9. Taking the centre of this area, shown as a continuous green line in Fig. 4.9, the reconstruction fidelity increases to $\approx 93\%$ for the Gaussian spectrum and $\approx 95\%$ for the Lorentzian. In a future experiment, this source of error could be reduced by a combination of stronger lasers (thus, faster projective measurements) and a correction factor in the theoretical treatment of the protocol.

The numerical results, on the other hand, allow for a high-fidelity reconstruction of the noise power spectral densities even for $Q = 14$. Moreover, the two spectra can be distinguished from both the second-order correlation function and the reconstructed spectrum. In this regard, it is worth noting that the overlap of the original Lorentzian and Gaussian power spectral densities is very high (97.7%), and thus very precise sensing is required to distinguish the two shapes. Taking Q equal to around 100 realisations, reconstruction fidelities of well above 99% are obtained.



(a)



(b)

Figure 4.9: Reconstructed power spectral density for (a) Gaussian and (b) Lorentzian noise. Both spectra have the same peak frequency and spectral width, and were reconstructed from the data presented in Fig. 4.7. The green curves show the reconstruction from the experimental data with $Q = 14$, while the shaded grey areas denote the frequency uncertainty due to the finite time duration of the laser pulses used for the projective measurements. The dashed yellow line is the original power spectral density of the noise (not taking into account the window function stemming from the finite pulse length), and the red and blue lines show the spectra reconstructed by using the data obtained from numerical simulations of the system dynamics with $Q = 14$ and $Q = 200$, respectively.

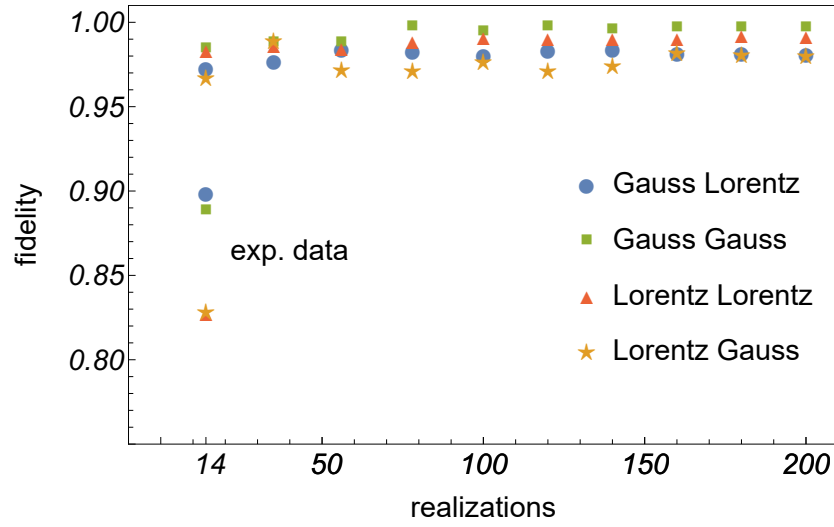


Figure 4.10: Fidelity obtained by comparing the reconstructed noise power spectral densities with the corresponding theoretical expressions. First, the reconstructed power spectral density of the Gaussian noise is compared with the theoretical expressions for both the original Lorentzian (blue circles) and Gaussian (green squares) spectra. Then, the reconstructed power spectral density of the Lorentzian noise is compared to both the Lorentzian (red triangles) and Gaussian (yellow stars) spectra. Overall, the reconstruction fidelity increases with the number of realisations Q , and again all numerical data points given by comparing curves from the same distribution are much closer to 1 than the others. Thus, it is again possible to distinguish between Gaussian and Lorentzian spectra. The lower data points referring to $Q = 14$ show the reconstructed power spectral densities of the noise directly from the experimental data.

Chapter 5

Designing quantum computation experiments

Within the last decade, significant progress has been made with machine learning algorithms in diverse domains, such as predictions, image recognition, speech recognition, medical diagnoses, and financial industry and trading. These algorithms allow software applications to become more accurate in performing a precise task without being given explicit instructions. The main idea consists of extracting patterns and making inferences from received data and using this statistical analysis to predict outputs and to improve with new experiences. Results may then be incorporated as newly available data.

Machine learning methods may be divided into different types of learning algorithms: supervised learning, unsupervised learning, reinforcement learning, feature learning, or sparse dictionary learning. This work makes use of reinforcement learning to search for beneficial quantum resources for quantum information.

The following research was conducted in the Quantum Information and Quantum Computing Lab in the Computer Science Department at Seoul National University under the supervision of Prof. Kim Taehyun (Seoul National University) and Prof. Son Wonmin (Sogang University).

5.1 Reinforcement learning

In reinforcement learning, an agent is taught to optimise its actions to get the best results. An agent takes actions in an environment and produces an outcome. After examining the outcome, satisfaction is expressed through a reward and a representation of the state. This reward is fed back to the agent. The agent continues the task by putting more weight on the actions

that give a desirable result. More precisely, here we apply a technique called ‘projective simulation’ introduced by the group of Hans J. Briegel [59].

The environment is our experiment, and each action taken in a trial is denoted by a_i , with $i \in \{1, \dots, N\}$ where N is the size of the action space $A = \{a_i\}_{i \in \{1, \dots, N\}}$. Each trial produces a state s_j in the total ensemble of outcomes $S = \{s_j\}_{j \in \{1, \dots, M\}}$.

We are interested in which action a_i or set of actions $A_i \in A$ would lead to a specific desired state s_j or group of desired states $S_j \in S$. The link between each pair (a_i, s_j) is then examined. To each link, a weight $h_{ij}^{(n)}$ is assigned which represents the joint probability of the pair, i.e., how probable it is for the action a_i or a set of actions containing a_i to produce a state s_j . This weight is evaluated for each trial (n). Note that K multiple experiments can be tried at the same time in a trial.

At first, without any information on quantum experiments, the computer is allowed to assume that each action has an equal probability of leading to the desired results:

$$h_{ij}^{(0)} = 1 \forall i, j \quad (5.1)$$

A set of actions is then chosen by randomly selecting L actions, where L is the length of the experiment, out of N actions with equal probabilities. There are $\binom{N}{L}$ possibilities for this choice. Note that some states are not accessible with just one action in the experiment and so require a length $L > 1$. Nevertheless, it is desirable to limit the total number of elements L in the experiment. Not only does it become impractical to carry out an experiment composed of many actions, but the quantum materials in the experiment (photons, ions, cold atoms) also have a limited coherence time and lifetime.

The state obtained by the process is calculated and evaluated against appropriate criteria to decide whether this state is of interest. This verification procedure is described for each experiment in the following sections.

After each trial, the weight is updated according to the outcomes. A reward λ is assigned to each action that leads to the desired state s :

$$h_{ij}^{(n+1)} - h_{ij}^{(n)} = \underbrace{-\gamma \left(h_{ij}^{(n)} - 1 \right)}_{\text{forget}} + \underbrace{\lambda \delta \left(s, s_j^{(n)} \right) \delta \left(a, a_i^{(n)} \right)}_{\text{reward}} \quad (5.2)$$

The probability to find an action that leads to a successful experiment is increased, the computer learns to prefer this action over others. However, over time, the computer will forget this preference, as this reward is damped

over time with a parameter γ . This updates the transition probabilities between each link ij , which are, according to the Bayes law, equal to the quotient of the joint probability over the marginal:

$$p^{(n+1)}(a_i|s_j) = \frac{h_{ij}^{(n+1)}}{\sum_{a \in A} h^{(n+1)}(a, s_j)} \quad (5.3)$$

For the next trial, the agent learns and chooses a new set of actions according to the Bayesian probabilities above. This favours the actions that gave good results previously.

Learning parameters

Various parameters have been introduced already, such as the number of choices of experiments K , the length of the experiment L , the loss of memory γ , and the reward λ . The values of these parameters can dramatically change the learning procedure of the agent.

For example, if K is set to the total number of possible experiments created by combinations of actions, the learning is useless, as every case is examined to start with. However, if K is set to a small number, the creativity of the agent is limited. The agent will not explore diverse possibilities, and once a good experiment is found, the agent will keep to the same actions and the same experiments without trying novel combinations of actions.

Likewise, the agent behaves differently depending on how much it is rewarded for a successful experiment. A relatively small value of the reward λ does not have much impact on the agent, but an enormous value of λ stops the agent from being innovative, as it keeps performing the same tasks for which it was praised.

To avoid this, in the script we prevent the agent from investing in an experiment already examined; however, it is also necessary to set the right parameters in order to prevent the script from falling into a repetitive loop.

The settings for these parameters also depend strongly on the requirements for the agent. Would we like the agent to find as many usable methods as possible for a collective group of outcomes, or would we like it to find a unique way to target a specific task? Depending on the goal, it is crucial to find the corresponding values for each parameter of the experiment.

Refining the algorithm

A few final refinements of the algorithm have been made to allow more control over the direction of the investigation.

Glow– As seen from Eq. 5.2, the reward is given to the latest successful experiment. However, successful experiments should continue to have an impact on the agent before being forgotten. A parameter called ‘glow’ is associated with each action–state pair ij and initially set to 0. It switches to a value of 1 on trial (n) if the link ij leads to a successful experiment, and is damped with a rate η in each subsequent trial.

$$\begin{aligned}
 h_{ij}^{(t+1)} - h_{ij}^{(t)} &= -\gamma \left(h_{ij}^{(t)} - 1 \right) + \lambda \underbrace{g_{ij}^{(t+1)}}_{\text{glow}} \\
 g_{ij}^{(0)} &= \delta \left(s_i, s^{(0)} \right) \delta \left(a_j, a^{(0)} \right) \\
 g_{ij}^{(t+1)} &= (1 - \eta) g_{ij}^{(t)}
 \end{aligned} \tag{5.4}$$

Action composition– Aside from rewarding the actions that lead to good results, the full set of actions can also be grouped into one long action. A successful experiment is added back to the list of actions, where it can be used to compose further new experiments.

When performing this task, we have to be careful that these new actions are more extended. An extended action a_i made with n initial single actions grouped together have a length $L_i = n > 1$. Consider an experiment made with $i_1^{th}, i_2^{th}, \dots, i_m^{th}$ actions. One has to ensure that the total length of the combination $\sum_{i_j} L_{i_j}$ does not exceed the maximal length allowed for an experiment to remain stable.

We later observe that for some cases this method helps to find successful experiments more rapidly; for example, an experiment that gives a maximally entangled state is composed of experiments that give partially entangled states (see below).

5.2 Producing high dimensional entangled resource

We study the case of projective simulation applied to manipulate entanglement between the angular momentum of photons, proposed by the group of A. Zeilinger [61]. The aim is to create a high-dimensionally entangled tripartite state. It is essential to first define a method to estimate the entanglement (see 5.2.1) and to describe the experimental setup before proceeding to design the corresponding script.

5.2.1 Entanglement estimation

The problem is to evaluate how much entanglement is present in the system. For a bipartite system, i.e., a system composed of two photons, it is enough to factorise the final state. In this case, when a Schmidt decomposition is performed, the Schmidt number [60] is sufficient to determine the number of dimensions needed to represent the final quantum state. In the bipartite case, the entanglement happens between two photons; hence, they each have the same degree of entanglement.

However, in the case of a tripartite system, the entanglement is not always shared between all three photons. The three photons can be maximally entangled, such as in the Greenberger-Horne-Zeilinger state [62] $|000\rangle + |111\rangle + \dots + |lll\rangle$. It is also possible to have, for example,

$$|\psi\rangle_{3,3,2} = |000\rangle + |111\rangle + |122\rangle \quad (5.5)$$

In this case, the second and the third photon are entangled with all the other photons, which means that knowing the state of the second or third photon is sufficient to determine the states of all three photons. However, the first photon is only partially entangled, which means that knowing the first photon's state gives some information about the second and the third photon, but does not allow the state of each photon to be entirely determined.

Examining each photon by partially tracing the density matrix of the final state over the other two photons, we find that the rank of the reduced state of the second and third photons is 3, while that of the first photon is 2. This value is called the Schmidt rank, and it quantifies the entanglement dimensionality of each party in an arbitrary multipartite state.

We denote as $SRV(3, 3, 2)$ the family of states that have one photon two-dimensionally entangled with other two, and two photons each three-dimensionally entangled with the other two. $|000\rangle + |102\rangle + |213\rangle$ is an example of such a state.

Generally, every tripartite state may be classified by calculating its Schmidt ranks and denoting the corresponding family as $SRV(r_i, r_j, r_k)$. Conventionally, this is written in descending order $r_i > r_j > r_k$, where the highest entanglement dimension is listed first.

Note that a Schmidt rank of 1 means that the particle is separable. A state in $SRV(r_i, r_j, 1)$ is a system of two entangled particles and one separable particle, whereas $SRV(1, 1, 1)$ has no entanglement between the three photons.

Note that this procedure requires a longer calculation time than factorisation. However, it is necessary to perform it in order to thoroughly examine the state. In the learning algorithm, we first factorise the final states and

check the coefficient of each term as a preliminary test, eliminating states that have an insufficient Schmidt number. Therefore, only the states that satisfy the Schmidt number criteria go through the lengthier Schmidt rank calculation procedure.

5.2.2 Materials

We aim to identify experiments that create an entangled tripartite state, reproducing the techniques described in [61].

The initial state consists of two pairs of photons created by two spontaneous parametric down-conversion (SPDC) events. Each pair is three-dimensionally entangled in the orbital angular momentum (OAM) degree of freedom. The polarisation degree of freedom is neglected.

Of the four photons, one is used as a trigger for the other three photons. If the remaining three-photon state fulfills the criteria (maximally entangled, SRV state), then it is recorded in a text file. Note that we also ensure to record only the states that are stable, i.e., higher-order creations from SPDC do not modify the states.

The initial actions that the agents are allowed to use are:

Spontaneous parametric down-conversion (SPDC)– The photon is split in a nonlinear scattering process within a crystal, conserving energy and momentum.

$$DownConv(l, a, b) = \sum_{m=-l}^l a(-m)b(m) \quad (5.6)$$

where l is the OAM degree and a, b are, respectively, the first and second paths from the splitting process.

Beam splitter– The beamsplitter is non-polarised and reflects or transmits light with equal probability.

$$\begin{cases} BS(a(-l)) = \frac{b(l)+ia(-l)}{\sqrt{2}} \\ BS(b(l)) = \frac{a(l)+ib(-l)}{\sqrt{2}} \end{cases} \quad (5.7)$$

Reflection– The reflection reverses the OAM of a photon:

$$Ref(a(l)) = ia(-l) \quad (5.8)$$

OAM Hologram– The OAM hologram modifies the OAM of a photon by m :

$$OAMHolo(a(l), m) = a(l + m) \quad (5.9)$$

5.2. PRODUCING HIGH DIMENSIONAL ENTANGLED RESOURCE 75

Dove prism– The Dove prism is a reflective prism that inverts the OAM of a photon and adds a phase to its quantum state.

$$DP(a(l)) = ie^{i\pi l}a(-l) \quad (5.10)$$

Parity sorter– The parity sorter is composed of a successive series of operations – beamsplitter, reflection, reflection, Dove prism, reflection, and beamsplitter [63] – which sorts even and odd OAM modes:

$$\begin{cases} LI(a(l)) = (\cos l\frac{\pi}{2})^2 a(l) + i (\sin l\frac{\pi}{2})^2 b(-l) \\ LI(a(l)) = -(\cos l\frac{\pi}{2})^2 b(l) + i (\sin l\frac{\pi}{2})^2 a(-l) \end{cases} \quad (5.11)$$

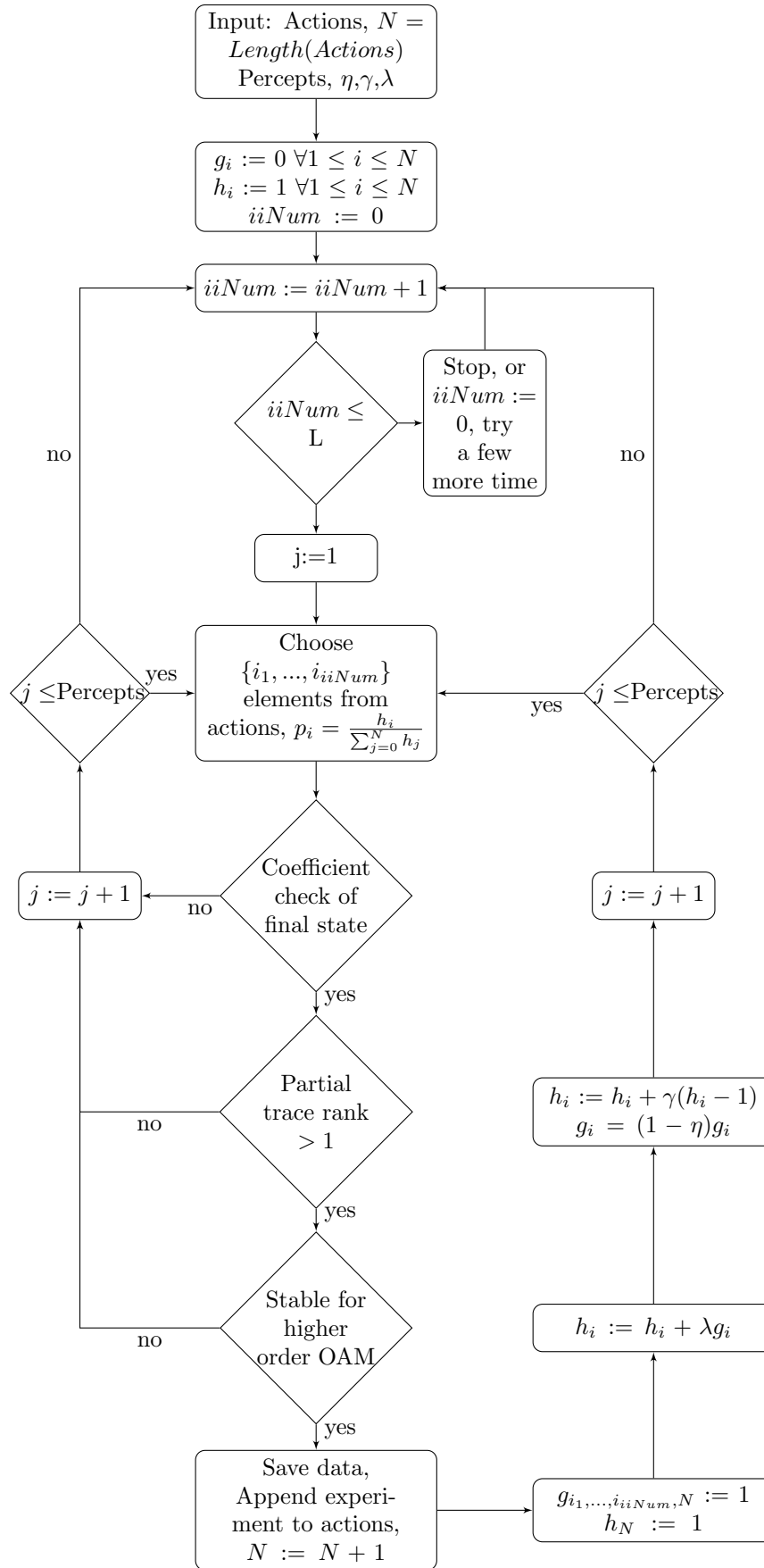
This parity sorter helps to suppress states that come from two different mechanisms of SPDC, such as $|\psi\rangle = |0, 0\rangle - |1, 1\rangle$, which is created by zero-level scattering in the first SPDC and first-level scattering in the second SPDC.

5.2.3 Algorithm

The group of A. Zeilinger has released a script for a part of their work on searching for experiments leading to tripartite entanglement [64], without applying any learning methods. Later, they collaborated with the group of H. J. Briegel [59] to adapt their projective simulation method [61] to search for more precise goals, targeting more specific state such as $SRV(3, 3, 3)$ (maximally entangled tripartite state), but this work did not come with a script.

In the next part of this study, I implement a projective simulation based on the method described in [61] and characterise the learning process of each additional task. Note the following results and conclusions are drawn from the observation of the performance of my script only and do not represent the original work of Zeilinger’s group.

The algorithm is detailed below:



All action–state pairs (a_j, s_j) are initialised with weight $h_{ij} = 1$ and glow $g_{ij} = 0$.

Algorithm 1: To choose *AllSizeList* experiments each containing *iiNum* optical elements from the action list, I use variables *aa* for the list of all chosen setups, *bb* for the length of a setup, and *cc* for the list of optical elements in the setup. The script adds one action at a time to *cc* until *bb* surpasses the maximum number of optical elements for a setup. Note that an action could contain more than one optical element.

```

def: Actionschoice(actionTable, actionlistsize, actioniiNum, weightlist)
1  aa = [];
2  for i in range(actionlistsize) do
3      j = 0;
4      cc = [];
5      while j < actioniiNum do
6          dd = choice(range(len(actionTable)), size = 1,
7                     p = [x/np.sum(weights) for x in weightlist])[0]);
8          cc.append(dd);
9          j = j + len(actionTable[dd]);
10     end
11  aa = aa + [cc];
end

```

The function **ActionsChoice**(*actions*, *AllSizeList*, *iiNum*, *weight*) (see Fig.1) then selects *AllSizeList* experiments, each containing *iiNum* optical elements, from the action list, with a probability determined by Eq. 5.3.

The following steps were initially present in the script of A. Zeilinger’s group [64]:

1. First check that the two parametric down-conversion processes were simultaneous and eliminate every single down-conversion event.
2. Next inspect the outcome from each experimental setup: inspect the coefficients of the outcome state by regrouping similar terms, check their values, and return only those states which the coefficients show to be non-separable.
3. Proceed to check the Schmidt rank vector of the final state by partially tracing the final density matrix and evaluating the rank of the reduced density matrix for each particle.
4. Only then test whether higher-order scattering from the spontaneous parametric down-conversion modified the final state.

The last step and the calculation of the Schmidt rank vector are relatively slow compared to other tasks, and we only perform them after carrying out several preliminary tests.

Algorithm 2:

```

1 glow[AllListNum[iiList]] = [1];
2 if setupString.nj < 6 then
3   | actions.append(setupString.rvATL);
4   | glow.append([1]);
5   | weights.append([1]);
6 else
7   | pass
8 end
9 weights = weights + reward.glow

```

After the verification procedure, the states that merit a reward have their weight and glow matrices updated accordingly (see Fig.2). A ‘forget’ term is also included, which determines whether the agent forgets between tests, either between one percept and the next or between one set of experiments and the next.

Algorithm 3:

```

1 weights = weights -  $\gamma * (weights - 1)$ ;
2 glow =  $(1 - \eta) * glow$ ;

```

5.2.4 Results

Search for tripartite entangled states

In the first instance, we search for experiments that give entangled tripartite states of any degree of entanglement, i.e., any $SRV(x, y, z)$ with $z \neq 1$.

Adding the projective simulation to the original script from the group of A. Zeilinger appears to slow the search process significantly. One reason may be the action composition task, which requires successive selection of $iiNum$ actions instead of selecting $iiNum$ actions at once. Using the same script with consecutive selection and varying only the values of the reward parameters, it appears that the projective simulation does affect the search time compared to the case of no reward ($\lambda = 0$). However, the experiment with automated search and without projective simulation may not be the same as the one previously published [64]. It is difficult to make a definite

claim as the total number of calculation operations in each script has not been determined, and I did not have precise control over the performance of the computer.

In consequence, while the number of interesting experiments identified in a given time would be one means of quantifying the search, calculation time is not necessarily a valid parameter for comparing different experiments run on different computers with different internal memory and different applications running at the same time. Hence the number of experiments per iteration was chosen as the basis for comparison.

No interesting experiments were found for $iiNum = 1$ and $iiNum = 2$. For the rest of the results section, all curves begin with $iiNum = 3$, i.e., the first iteration number represents the first test made for a three-element experiment.

The following paragraphs study the influence of the number of percepts, the reward parameter and the action composition to the number of experiments found per iteration and their lengths.

The effect of trying many percepts

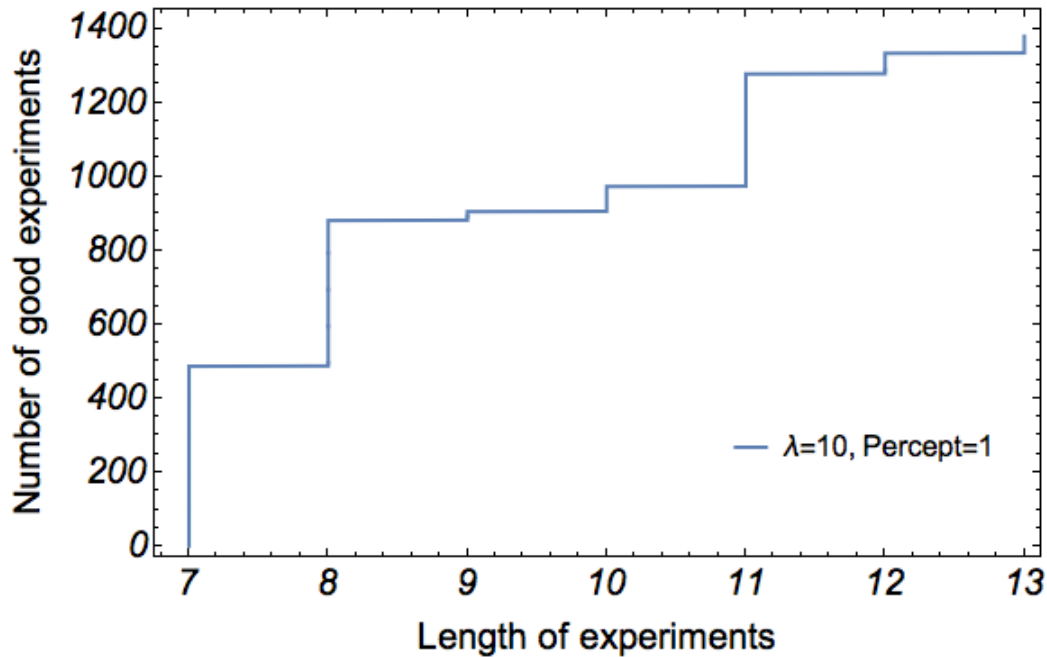


Figure 5.1: Number of successful experiments found for each set length

It is crucial to try various tests for each set length of the experiment $iiNum$. Figure 5.1 shows a search with one percept, which means only one set of actions is examined for each set length $iiNum \in [3, 13]$. In order to

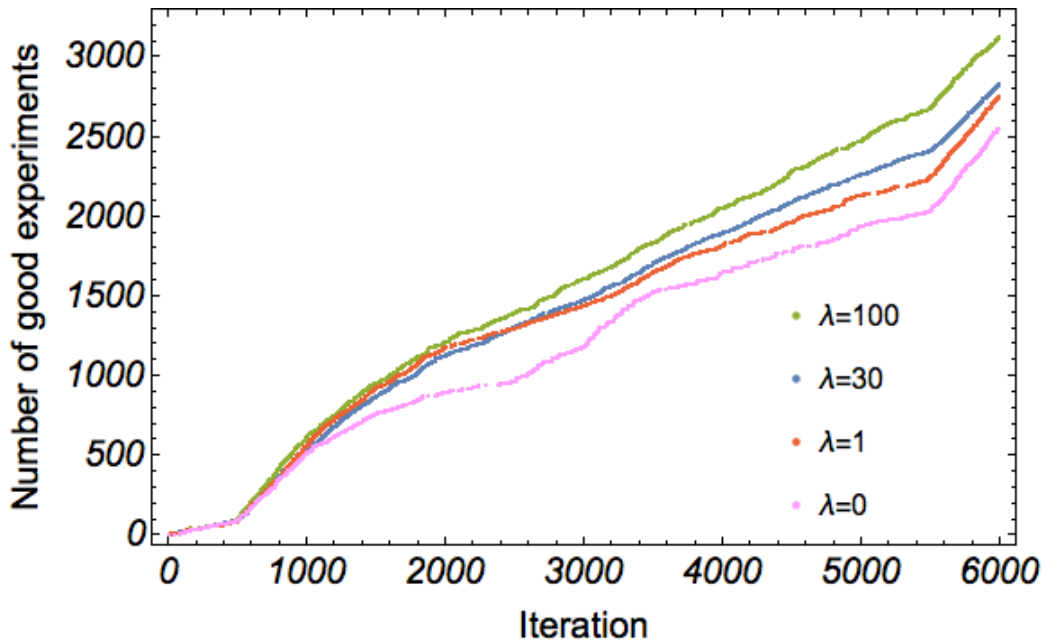


Figure 5.2: The number of successful experiments found as a function of the number of iterations increases with the reward parameter.

run more than 13 trials, once the maximum value $iiNum = 13$ is reached, the system is reset to $iiNum = 3$ and the process is repeated.

The first successful experiment was found for $iiNum = 7$, the first six experiments having failed. Due to the high reward $\lambda = 10$, the probability of choosing this successful experiment and its elements again was quite high. As a result, the agent only found experiments with a length $iiNum \leq 7$ despite the existence of successful tests with shorter lengths. This illustrates that the system's creativity to explore new designs was limited.

The effect of rewarding the agent

The rate of finding experiments increases with the reward parameter λ , for a fixed number of percepts set to 500. (See Fig. 5.2.)

The effect of composing the actions

Figure 5.3 shows the number of successful experiments as a function of the number of searches for a small reward parameter $\lambda = 2$ with various percepts. It can be seen that all the curves start out the same for the first iteration set, testing experiments composed of three elements ($iiNum = 3$).

As the length of the experiment grows, the agent can also make use of shorter experiments that were found previously and added to the action list. The red curves show more experiments with four components, $iiNum = 4$, appearing at iteration 1000; the same rise appears in the blue curve at

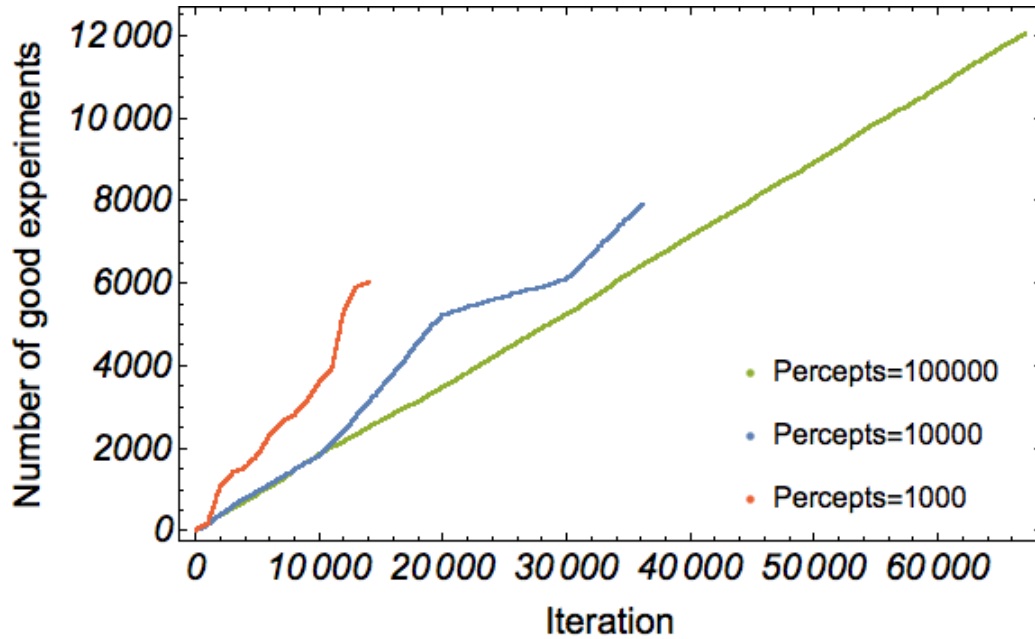


Figure 5.3: The number of experiments that produce a tripartite entangled state, for a constant reward of $\lambda = 2$

iteration 10000, and so on.

Nonetheless, action composition can also confuse the agent and slow down the process for a certain length. For example, between iteration number 20000 and iteration number 30000 in the blue curves ($iiNum = 5$), it is possible that many three-component actions which were previously rewarded have been chosen, but it is more difficult to select two single-component actions to match them with. During these iterations, the curve displays a smaller slope compared to the beginning of the search.

Search for $SRV(3, 3, 3)$ by rewarding $SRV(3, 3, 2)$ state

Note that in the following study, one aim was to find an experiment that gave a $SRV(3, 3, 3)$ (lowest order maximally entangled state) only, and not to stick with the previous goal of this script to find all experiments that lead to tripartite entangled state. I made small changes to this step and raised the criteria accordingly, which I explain below in the ‘results’ section.

The results published in [61] demonstrate that an experiment to create $SRV(3, 3, 3)$ was discovered from experiments that lead to $SRV(3, 3, 2)$ states. To increase the speed of the script, all experiments that did not lead to $SRV(3, 3, 2)$ or $SRV(3, 3, 3)$ states were eliminated. Of course, this elim-

inates many possibilities to learn from other classes of experiments that give entangled tripartite states.

One aspect that was not mentioned in the original work is that increasing the reward parameter λ decreases the diversity of the results. More precisely, the authors specified that a reward $\lambda = 100$ was used to increase the rate of finding interesting experiments, while to explore the possibilities of finding a $SRV(3, 3, 3)$ state a reward of $\lambda = 1$ was used instead. In order to reach a specific goal such as finding a $SRV(3, 3, 3)$ state, they found it necessary to try a more extensive range of action compositions, and hence the reward parameter was decreased from $\lambda = 100$ to $\lambda = 1$.

In our search, we tried to use a minimal reward, such as $\lambda = 1$ or $\lambda = 5$. The number of percepts in the test was also increased, which helps the agent reach for more diversity, but the increase needs to be kept reasonably small to preventing slowing down the script too much. Also if the number of percepts is set to the maximum combinations that the computer can make, there is no learning at all.

For example, for a small reward $\lambda = 1$ with a fixed number of iterations $N \approx 120000$ and a fixed number of percepts 45000 we found:

1. No experiments leading to $SRV(3, 3, 3)$ by rewarding every tripartite entangled state found;
2. Four experiments leading to $SRV(3, 3, 3)$ by rewarding $SRV(3, 3, 3)$ only;
3. Six experiments leading to $SRV(3, 3, 3)$ by rewarding setups producing both $SRV(3, 3, 2)$ and $SRV(3, 3, 3)$.

1. Setup: BS(OAMHolo(LI(XXX,b,c),b,2),a,b); Trigger on $|0\rangle + |1\rangle$

2. Setup: BS(OAMHolo(LI(XXX,b,c),b,2),a,b); Trigger on $|1\rangle + |2\rangle$

3. Setup: BS(OAMHolo(LI(OAMHolo(XXX,e,2),b,c),b,2),a,b);
Trigger on $|0\rangle + |1\rangle$

4. Setup: BS(OAMHolo(LI(OAMHolo(XXX,e,2),b,c),b,2),a,b);
Trigger on $|1\rangle + |2\rangle$

5. Setup:

BS(OAMHolo(LI(OAMHolo(LI(OAMHolo(XXX,e,9),a,c),f,7),b,c),b,2),a,b);
Trigger on $|0\rangle + |1\rangle$

6. Setup:

BS(OAMHolo(LI(OAMHolo(LI(OAMHolo(XXX,e,9),a,c),f,7),b,c),b,2),a,b);
Trigger on $|1\rangle + |2\rangle$

We were also able to find the setup presented in [61] but with a shorter length, by replacing the set of a reflection and an OAM hologram with value -2 by a single OAM hologram with value $+2$.

The use of a glow parameter allows the damping of the reward effect to be more finely tuned than simply using exponential damping with the parameter γ .

5.3 Designing ion quantum gates

Having learned and tested the method of projective simulation in the case of photons, we next apply it to our experiments.

In the Quantum Information and Quantum Computing Lab at Seoul National University, we mainly focused on hardware development for quantum computers and quantum repeaters based on ion trap systems and application of quantum algorithms and protocols to a real quantum system.

Trapped ions are a powerful resource for quantum computing as they enable individual manipulation of single qubits at room temperature. Hence we believe that it is crucial to find creative new ways of designing quantum computing experiments in ion trap systems. Specifically, we focus on exploiting the coupling between the vibrational motion and the atomic levels of the ion to fabricate diverse quantum logic gates. Here an agent is used to help discover how quantum gates can be experimentally implemented in our system, without prior knowledge.

5.3.1 Materials

The list of actions includes all the couplings between the ion's atomic levels and its motion that can be produced by resonant light, red-shifted light, blue-shifted light and rotation to auxiliary state for each of the qubits. The example below shows blue-shifted light that couples the \downarrow level with the ground state of the vibrational motion $n = 0$ of the first qubit with the \uparrow level with zero motion with the first excited state of the vibrational motion $n = 1$.

$$H_{blue1} = \begin{array}{c} \text{indices} \\ \uparrow\uparrow 0 \\ \uparrow\downarrow 0 \\ \downarrow\uparrow 0 \\ \downarrow\downarrow 0 \\ \uparrow\uparrow 1 \\ \uparrow\downarrow 1 \\ \downarrow\uparrow 1 \\ \downarrow\downarrow 1 \end{array} \begin{bmatrix} \uparrow\uparrow 0 & \uparrow\downarrow 0 & \downarrow\uparrow 0 & \downarrow\downarrow 0 & \uparrow\uparrow 1 & \uparrow\downarrow 1 & \downarrow\uparrow 1 & \downarrow\downarrow 1 \\ 0 & 0 & 0 & 0 & 0 & 0 & 0 & 0 \\ 0 & 0 & 0 & 0 & 0 & 0 & 0 & 0 \\ 0 & 0 & 0 & 0 & \frac{\Omega_{blue1}}{2} & 0 & 0 & 0 \\ 0 & 0 & 0 & 0 & 0 & \frac{\Omega_{blue1}}{2} & 0 & 0 \\ 0 & 0 & \frac{\Omega_{blue1}}{2} & 0 & 0 & 0 & 0 & 0 \\ 0 & 0 & 0 & \frac{\Omega_{blue1}}{2} & 0 & 0 & 0 & 0 \\ 0 & 0 & 0 & 0 & 0 & 0 & 0 & 0 \\ 0 & 0 & 0 & 0 & 0 & 0 & 0 & 0 \end{bmatrix} \quad (5.12)$$

Meanwhile, red-shifted light couples $|\downarrow, n=1\rangle$ to $|\uparrow, n=0\rangle$, the resonant light couple \downarrow and \uparrow with the same vibrational motion n . Rotation to auxiliary state starts from $|\downarrow\downarrow 1\rangle$ level, is set on resonance and adds a π phase for a full rotation. For a quantum phase gate, this rotation could also set off-resonance to generate arbitrary geometrical phase (See Chapter 3.)

We train an agent to search for combinations of actions that lead to a quantum logic gate by rewarding successful ones. For example, a SWAP gate was found by combining action numbers

$$7, 10, 10, 13, 10, 7 \quad (5.13)$$

equivalent to:

1. π -pulse coupling $|\uparrow y0\rangle \leftrightarrow |\downarrow y1\rangle$
2. 2π -rotation from $|x \downarrow 1\rangle$ to $|x \uparrow 0\rangle$
3. 2π rotation from $|\downarrow\downarrow 1\rangle$ to auxiliary state
4. π -pulse coupling $|x \downarrow 1\rangle \leftrightarrow |x \uparrow 0\rangle$
5. π -pulse coupling $|\uparrow y0\rangle \leftrightarrow |\downarrow y1\rangle$

It is commonly known that a SWAP gate can be fabricated using three CNOT gates [66]. However, a Cirac-Zoller CNOT gate itself has a length of three actions. In this scheme, the SWAP gate contains twelve transitions, which could be too long for the stability of a real experiment. Our agent found an experiment using six action elements for the SWAP gate. Furthermore, a repetition of action number 10 (π rotation from $|\downarrow\downarrow 1\rangle$ to auxiliary state) could be combined into a 2π rotation from $|\downarrow\downarrow 1\rangle$ to an auxiliary state,

reducing the length of the experiment to five successive transitions, half that of the conventional SWAP gate.

This is not the only five-component SWAP gate that has been identified by the script. However, while the algorithm is particularly good at finding the SWAP gate, it hasn't shown outstanding performance for other quantum logic gates. We expect that in future work the script will rediscover the Cirac-Zoller CNOT gate and will enable us to find other possible quantum gates by changing the search parameters and adding features, such as glow and action composition, which were utilised in the previous work on photons.

We are also considering implementing a new technique called 'clip deletion' [61]: after an action is created, if it does not lead to a successful gate within several successive trials, it is deleted from the action list. Doing this reduces the demands on the agent's limited memory.

5.4 Two qubits system made with QZE

Last but not least, this work carried in Seoul National University is also applicable to other quantum systems, including the BEC on-chip setup in my original group.

Recall the ^{87}Rb structure. When applying a strong Raman coupling between $|F = 2, m_f = 0\rangle$ and $|F = 1, m_f = 0\rangle$, quantum Zeno effect can be realized [13]. Observe that each hyperfine can be separated into two subspaces evolve coherently with each other, representing two qubits. The two subspace successively can be named $|\downarrow\downarrow\rangle, |\downarrow\uparrow\rangle$ and $|\uparrow\downarrow\rangle, |\uparrow\uparrow\rangle$.

Previous idea of a quantum phase gate has been proposed using the RF field coupling magnetic sublevels $|F = 2, m_F = 2\rangle \leftrightarrow |F = 2, m_F = 1\rangle$ and $|F = 2, m_F = -2\rangle \leftrightarrow |F = 2, m_F = -1\rangle$. However, with the actions list composed of RF field coupling magnetic sublevels, microwave field coupling different hyperfine state, similar projective simulation method can be applied in the future to find quantum logic gate design.

Conclusion

Quantum evolution typically leads to phase shifts with mixed geometric and dynamical origins. To identify geometric phases it is necessary to eliminate the dynamical phase from the total phase. In this experiment, we have generated and measured geometric phases in a system of cold trapped atoms by realising a sequence of closely spaced projectors along a closed trajectory. This evolution consists of a combination of dynamical quantum Zeno effect and free evolution. By separately analysing the phase shifts generated in each step, we demonstrate – both theoretically and experimentally – that the geometric phase is imprinted in the free evolution as an Aharonov-Anandan phase and the dynamical phase cancels out. The quantum Zeno effect thus represents a robust method to separate dynamical and geometric contributions of the quantum phase.

This method creates two alternative ways to reveal the geometric Aharonov-Anandan phase generated by the free evolution. Either we can compare the evolution to the free evolution that is obtained by ‘switching off’ the driving Hamiltonian, or we can disable the formation of a geometric phase by realising quantum Zeno dynamics through frequently repeated measurements. Both methods enable the contribution of the dynamical phase to be identified and removed from the total phase. The latter possibility has particularly interesting applications since it does not require the ability to control the Hamiltonian.

The presented method enables the measurement and identification of geometric phases in systems where they are normally concealed by dynamical phases that cannot be easily determined or eliminated. As such, it may lead to interesting novel approaches for the identification of topological phases of matter [43, 44] in synthetic systems [33] and potential applications in the context of quantum phase transitions [45] or quantum computations [46, 47].

On another hand, we have presented and experimentally demonstrated a new method, based on the stochastic quantum Zeno effect, for measuring the power spectral density of an unknown transverse noise field. Examples of Lorentzian and Gaussian spectra were experimentally reconstructed with

fidelity as large as 80 % (Lorentzian) and almost 90 % (Gaussian). This fidelity increases to more than 99 % in numerical simulations, which also allow the two different spectra to be distinguished.

In the future, by enhancing the long-period stability of the experiment we aim to increase the number of repetitions Q while reducing the measurement spread, improving the quality of the statistics. The numerical analysis shows that a factor of five would be sufficient to substantially improve the fidelity of the protocol and distinguish a Lorentzian power spectral density from a Gaussian with the same peak position and width. As already mentioned, the finite time duration of the projective measurements is a considerable source of error, which could be reduced with higher laser power and a correction term in the theoretical treatment.

From a purely theoretical point of view, a major step forward would be a better design of the control pulses adopted to reconstruct the noise power spectral densities, which may also be changing in time [58]. Finally, the reconstruction fidelity could be increased by experimentally implementing entangled probes or, as an alternative, by using feedback control and machine-learning-enhanced reconstruction methods.

Promising quantum technologies could also be explored with experiments suggested by a reinforced-learning agent, who can test creative approaches without prior knowledge. As an outlook, regardless of the quantum system (cold atoms, single ions, or photons), we expect to discover exciting prospects in the future.

Bibliography

- [1] H. -V. Do, M. Gessner, F. S. Cataliotti, A. Smerzi, Measuring geometric phases with a dynamical quantum Zeno effect in a Bose-Einstein condensate, [Phys. Rev. Research **1**, 033028](#) (2019).
- [2] H. -V. Do, C. Lovecchio, N. Fabbri, F. S. Cataliotti, S. Gherardini, M. M. Müller, N. Dalla Pozza, F. Caruso, Experimental proof of Quantum Zeno-assisted Noise Sensing, [arXiv:1907.09618](#) (2019).
- [3] L. Viola, E. Knill, and S. Lloyd. Dynamical decoupling of open quantum systems. [Phys. Rev. Lett. **82**, 2417](#) (1999).
- [4] G.S. Uhrig. Exact results on dynamical decoupling by π pulses in quantum information processes, [New. J. Phys. **10**, 083024](#) (2008).
- [5] B. Misra and E. C. G. Sudarshan, The Zeno's paradox in quantum theory, [J. Math. Phys. **18**, 756](#) (1977).
- [6] W. M. Itano, D. J. Heinzen, J. J. Bollinger, and D. J. Wineland, Quantum Zeno effect, [Phys. Rev. A **41**, 2295](#) (1990).
- [7] P. Kwiat, H. Weinfurter, T. Herzog, A. Zeilinger, and M.A. Kasevich. Interaction-Free Measurement, [Phys. Rev. Lett.**74**, 4763](#) (1995).
- [8] M.C. Fischer, B. Gutierrez-Medina, and M.G. Raizen. Observation of the Quantum Zeno and Anti-Zeno Effects in an Unstable System, [Phys. Rev. Lett.**87**, 040402](#) (2001).
- [9] J. von Neumann, *Mathematische Grundlagen der Quantenmechanik* (Springer, Berlin, 1932).
- [10] P. Facchi, and S. Pascazio. Quantum Zeno subspaces, [Phys. Rev. Lett.**9**, 080401](#) (2002).
- [11] P. Facchi and S. Pascazio, Quantum Zeno dynamics: mathematical and physical aspects, [J. Phys. A: Math. Theor. **41**, 493001](#) (2008).

- [12] A. Smerzi, Zeno dynamics, indistinguishability of state, and entanglement, *Phys. Rev. Lett.* **109**, 150410 (2012).
- [13] F. Schäfer, I. Herrera, S. Cherukattil, C. Lovecchio, F. S. Cataliotti, F. Caruso, and A. Smerzi, Experimental realization of quantum zeno dynamics, *Nat. Commun.* **5**, 3194 (2014).
- [14] A. Signoles, A. Facon, D. Grosso, I. Dotsenko, S. Haroche, J.-M. Raimond, M. Brune and S. Gleyzes, Confined quantum Zeno dynamics of a watched atomic arrow, *Nature Phys.* **10**, 715 (2014).
- [15] F. Sakuldee, and L. Cywiński. On relationship between subjecting the qubit to dynamical decoupling and to a sequence of projective measurements. Eprint arXiv:1907.05165 (2019).
- [16] K. E. Gibble, S. Kasapi, and S. Chu, Improved magneto-optic trapping in a vapor cell, *Opt. Lett.* **17**, 7, 526 (1992).
- [17] C. N. Cohen-Tannoudji, Manipulating atoms with photons, *Rev. Mod. Phys.* **70** 707 (1998).
- [18] William D. Phillips, Laser cooling and trapping of neutral atoms, *Rev. Mod. Phys.* **70** 721 (1998).
- [19] T. M. Roach, H. Abele, M. G. Boshier, H. L. Grossman, K. P. Zetie, and E. A. Hinds, Realization of a Magnetic Mirror for Cold Atoms, *Phys. Rev. Lett.* **75**, 629 (1995).
- [20] T. W. Hänsch and A. L. Schawlow, Cooling of gases by laser radiation, *Opt. Commun.* **13** 68(1975).
- [21] J. Dalibard and C. Cohen-Tannoudji, Laser cooling below the Doppler limit by polarization gradients: simple theoretical models, *J. Opt. Soc. Am. B*, **6** 2023 (1989).
- [22] E. Majorana, Atomi orientati in campo magnetico variabile, *Nuovo Cimento* **9**, 43 (1932).
- [23] W. Gerlach and O. Stern, Das magnetische Moment des Silberatoms, *Z. Phys.* **9**, 353 (1922).
- [24] W. Ketterle, D. S. Durfee and D. M. Stamper-Kurn, Making, probing and understanding Bose-Einstein condensates in Proceedings of the International School of Physics "Enrico Fermi" **140** 67 (1999).

- [25] C. Lovecchio, F. Schäfer, S. Cherukattil, M. Ali Khan, I. Herrera, F. S. Cataliotti, T. Calarco, S. Montangero, and F. Caruso, *Phys. Rev. A* **93**, 010304(R) (2016).
- [26] M. V. Berry, Quantal Phase Factors Accompanying Adiabatic Changes, *Proc. Roy. Soc. A.* **392**, 45 (1984).
- [27] Y. Aharonov and J. Anandan, Phase change during a cyclic quantum evolution, *Phys. Rev. Lett.* **58**, 1593 (1987).
- [28] Shapere, A. and F. Wilczek, Geometric Phases in Physics (World Scientific, Singapore, 1989).
- [29] D. Suter, K. T. Mueller, and A. Pines, Study of the Aharonov-Anandan quantum phase by NMR interferometry, *Phys. Rev. Lett.* **60**, 1218 (1988).
- [30] C. A. Mead, The geometric phase in molecular systems, *Rev. Mod. Phys.* **64**, 51 (1992).
- [31] Y. Zhang, Y.-W. Tan, H. L. Stormer, and P. Kim, Experimental observation of the quantum Hall effect and Berry's phase in graphene, *Nature* **438**, 201 (2005).
- [32] P. J. Leek, J. M. Fink, A. Blais, R. Bianchetti, M. Göppl, J. M. Gambetta, D. I. Schuster, L. Frunzio, R. J. Schoelkopf, and A. Wallraff, Observation of Berry's Phase in a Solid-State Qubit, *Science* **318**, 1889 (2007).
- [33] M. Atala, M. Aidelsburger, J. T. Barreiro, D. Abanin, T. Kitagawa, E. Demler, and I. Bloch, Direct measurement of the Zak phase in topological Bloch bands, *Nature Phys.* **9**, 795 (2013).
- [34] C. Gross and I. Bloch, Quantum simulations with ultracold atoms in optical lattices, *Science* **357**, 995 (2017).
- [35] D. Leibfried, B. DeMarco, V. Meyer, D. Lucas, M. Barrett, J. Britton, W. M. Itano, B. Jelenković, C. Langer, T. Rosenband, and D. J. Wineland, Experimental demonstration of a robust, high-fidelity geometric two ion-qubit phase gate, *Nature* **422**, 412 (2003).
- [36] S. Pancharatnam, Generalized Theory of Interference and its Applications, Part I. Coherent Pencils, *Proc. Indian. Acad. Sci. A* **44**, 247 (1956).
- [37] M. V. Berry and S. Klein, Geometric phases from stacks of crystal plates, *J. Mod. Opt.* **43**, 165 (1996).

- [38] P. Hariharan, H. Ramachandran, K. A. Suresh, and J. Samuel, The Pancharatnam phase as a strictly geometric phase: A demonstration using pure projections, *J. Mod. Opt.* **44**, 707 (1997).
- [39] R. Bhandari, On geometric phase from pure projections, *J. Mod. Opt.* **45**, 2187 (1998).
- [40] A. K. Pati and S. V. Lawande, Quantum Zeno Dynamics and Inhibition of Geometric Phase, [arXiv:quant-ph/9806079](https://arxiv.org/abs/quant-ph/9806079).
- [41] P. Facchi, A. G. Klein, S. Pascazio, L. S. Schulman, Berry phase from a quantum Zeno effect, *Phys. Lett. A* **257**, 232 (1999).
- [42] N. F. Ramsey, A Molecular Beam Resonance Method with Separated Oscillating Fields. *Phys. Rev.* **78**, 695 (1950).
- [43] D. Xiao, M.-C. Chang, and Q. Niu, Berry phase effects on electronic properties, *Rev. Mod. Phys.* **82**, 1959 (2010).
- [44] X.-L. Qi and S.-C. Zhang, Topological insulators and superconductors, *Rev. Mod. Phys.* **83**, 1057 (2011).
- [45] S.-L. Zhu, Geometric phases and quantum phase transitions, *Intl. J. Mod. Phys. B* **22**, 561 (2008).
- [46] V. Vedral, Geometric phases and topological quantum computation, *Intl. J. Quant. Inf.* **1**, 1 (2003).
- [47] C. Nayak, S. H. Simon, A. Stern, M. Freedman, and S. Das Sarma, Non-Abelian anyons and topological quantum computation, *Rev. Mod. Phys.* **80**, 1083 (2008).
- [48] W.H. Zurek. Decoherence, einselection, and the quantum origins of the classical, *Rev. Mod. Phys.* **75**, 715 (2003).
- [49] A. Streltsov, G. Adesso, and M.B. Plenio. *Colloquium: Quantum coherence as a resource*, *Rev. Mod. Phys.* **89**, 041003 (2017).
- [50] C.L. Degen, F. Reinhard, and P. Cappellaro. Quantum sensing, *Rev. Mod. Phys.* **89**, 035002 (2017).
- [51] V. Giovannetti, S. Lloyd, and L. Maccone. Quantum Metrology, *Phys. Rev. Lett.* **96**, 010401 (2006).
- [52] V. Giovannetti, S. Lloyd, and L. Maccone. Advances in Quantum Metrology, *Nat. Photon.* **5**, 222–229 (2011).

- [53] L.T. Hall, J.H. Cole, C.D. Hill, and L.C.L. Hollenberg. Sensing of fluctuating nanoscale magnetic fields using nitrogen-vacancy centers in diamond, [Phys. Rev. Lett. **103**, 220802](#) (2009).
- [54] J.C. Cole, and L.C.L. Hollenberg. Scanning quantum decoherence microscopy, [Nanotechnology **20**, 495401](#) (2009).
- [55] G.A. Paz-Silva, and L. Viola. General transfer-function approach to noise filtering in open-loop quantum control, [Phys. Rev. Lett. **113**, 250501](#) (2014).
- [56] L.M. Norris, and G.A. Paz-Silva, and L. Viola. Qubit noise spectroscopy for non-Gaussian dephasing environments, [Phys. Rev. Lett. **116**, 150503](#) (2016).
- [57] M.M. Müller, S. Gherardini, and F. Caruso. Quantum Zeno dynamics through stochastic protocols, [Annalen der Physik **529**\(9\), 1600206](#) (2017).
- [58] M.M. Müller, S. Gherardini, and F. Caruso. Noise-robust quantum sensing via optimal multi-probe spectroscopy, [Sci. Rep. **8**, 14278](#) (2018).
- [59] H. J. Briegel, and G. De las Cuevas, Projective simulation for artificial intelligence, [Scientific Reports **2** 400](#) (2012)
- [60] B. M. Terhal and P. Horodecki, Schmidt number for density matrices, [Phys. Rev. A **61**, 040301](#) (2000).
- [61] A. A. Melnikov, H. P. Nautrup, M. Krenn, V. Dunjko, M. Tiersch, A. Zeilinger, and H. J. Briegel, Active learning machine learns to create new quantum experiments, [PNAS **115** **6** 1221-1226](#) (2018)
- [62] D. M. Greenberger, M. A. Horne, A. Zeilinger, Going Beyond Bell's Theorem, [Bell's Theorem, Quantum Theory and Conceptions of the Universe 69-72](#) (1989).
- [63] J. Leach, M. J. Padgett, S. M. Barnett, S. Franke-Arnold, and J. Courtial, Measuring the Orbital Angular Momentum of a Single Photon, [Phys. Rev. Lett. **88**, 257901](#) (2002).
- [64] M. Krenn, M. Malik, R. Fickler, R. Lapkiewicz, and A. Zeilinger, Automated Search for new Quantum Experiments, [Phys. Rev. Letter **116** 090405](#) (2016).
- [65] M. Huber, J. I. de Vicente, Structure of multidimensional entanglement in multipartite systems, [Phys Rev Lett. **110** **3** 030501](#) (2013).

- [66] D. W. Leung, M. A. Nielsen, I. L. Chuang, Y. Yamamoto, Approximate quantum error correction can lead to better codes, [Phys. Rev. A](#) **56** 2567 (1997).